

Thermoelectric properties of transition
metal oxides and thallium main group
chalcogenides

by

Jianxiao Xu

A thesis

presented to the University of Waterloo

in fulfillment of the

thesis requirement for the degree of

Doctor of Philosophy

in

Chemistry

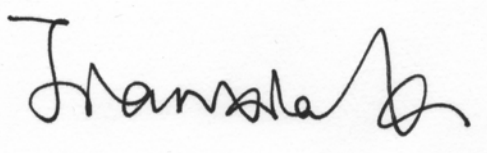
Waterloo, Ontario, Canada, 2008

©Jianxiao Xu 2008

Author's declaration

I hereby declare that I am the sole author of this thesis. This is a true copy of the thesis, including any required final revisions, as accepted by my examiners.

I understand that my thesis may be made electronically available to the public.

A handwritten signature in black ink, appearing to read "J. Mansala", is centered on the page. The signature is written in a cursive style with a large initial 'J' and a decorative flourish at the end.

Abstract

Thermoelectric energy (TE) conversion can be used to create electricity from temperature gradients. Hence power can be generated from waste heat using TE materials, e.g. from the exhaust in automotives. This power in turn may lead to a reduction of gas consumption by reducing the alternator load on the engine. Because of the increasing demand and limited availability of energy sources, there is strong and renewed interest in advancing thermoelectric materials. Past research shows that the best TE materials are narrow band gap semiconductors composed of heavy elements, exhibiting a large Seebeck coefficient, S , combined with high electrical conductivity, σ , and low thermal conductivity, κ .

Various research projects have been attempted during the past four years of my Ph.D. studies. These include the synthesis, crystal structure studies, electronic structure calculations and thermoelectric properties of transition metal oxides and thallium main group chalcogenides.

Because of the good thermal stability, lack of sensitivity to the air, and non-toxicity, transition metal oxides are potential candidates for commercial thermoelectric applications. During the investigation of oxides for thermoelectric application, several interesting features of different transition metal oxides have been discovered: 1. A new quaternary layered transition-metal oxide, $\text{Na}_2\text{Cu}_2\text{TeO}_6$, has been synthesized under air using stoichiometric mixtures of Na_2CO_3 , CuO and TeO_2 . $\text{Na}_2\text{Cu}_2\text{TeO}_6$ crystallizes in a new structure type, monoclinic space group $C2/m$ with $a = 5.7059(6) \text{ \AA}$, $b = 8.6751(9) \text{ \AA}$, $c = 5.9380(6) \text{ \AA}$, $\beta = 113.740(2)^\circ$, $V = 269.05(5) \text{ \AA}^3$ and $Z = 2$, as determined by single crystal X-ray diffraction. The structure is composed of $\infty^2[\text{Cu}_2\text{TeO}_6]$ layers with the Na atoms located in the octahedral voids between the layers. $\text{Na}_2\text{Cu}_2\text{TeO}_6$ is a green nonmetallic compound, in agreement with

the electronic structure calculation and electrical resistance measurement. 2. An *n*-type narrow band gap semiconductor, $\text{LaMo}_8\text{O}_{14}$, exhibiting the high Seebeck coefficient of $-94 \mu\text{VK}^{-1}$ at room temperature has been investigated. 3. $\text{Pb}_{0.69}\text{Mo}_4\text{O}_6$ with a new modulated structure and stoichiometry was determined from single-crystal X-ray diffraction data. The compound crystallizes in the tetragonal super space group, $P4/mbm(00g)00ss$, with $a = 9.6112(3) \text{ \AA}$, $c = 2.8411(1) \text{ \AA}$, $q = 0.25c^*$, which is different from the previously reported structure.

As for the research of thermoelectric properties of thallium main group chalcogenides, three new ternary thallium selenides, $\text{Tl}_{2.35}\text{Sb}_{8.65}\text{Se}_{14}$, $\text{Tl}_{1.97}\text{Sb}_{8.03}\text{Se}_{13}$ and $\text{Tl}_{2.04}\text{Bi}_{7.96}\text{Se}_{13}$, have been discovered. All three compounds crystallize in the same space group $P2_1/m$ with different cell parameters, and in part different Wyckoff sites, hence different structure types. The three selenides with similar structures are composed of distorted edge-sharing (Sb,Bi) Se_6 octahedra, while the distorted Tl/(Sb, Bi) sites are coordinated by 8 - 9 Se atoms. Electronic structure calculations and physical property measurements reveal they are semiconductors with high Seebeck coefficient but low electrical conductivity, and therefore not good thermoelectrics. On the other hand, our transport property measurements on the unoptimized Tl_2SnTe_3 sample show interesting thermoelectric properties of this known compound.

Advanced thermoelectrics are dominated by antimonides and tellurides so far. The structures of the tellurides are mostly composed of NaCl-related motifs; hence do not contain any Te-Te bonds. All of the antimonide structures containing Sb-Sb bonds of various lengths are much more complex. The Sb atom substructures are Sb_2^{4-} pairs in $\beta\text{-Zn}_4\text{Sb}_3$, linear Sb_3^{7-} units in $\text{Yb}_{14}\text{MnSb}_{11}$, planar Sb_4^{4-} rectangles in the skutterudites, e.g., $\text{LaFe}_3\text{CoSb}_{12}$, and Sb_8 cubes interconnected via short Sb-Sb bonds to a three-dimensional network in $\text{Mo}_3\text{Sb}_5\text{Te}_2$.

The results of electronic structure calculations suggested that these interactions have a significant impact on the band gap size as well as on the effective mass around the Fermi level, which represent vital criteria for advanced thermoelectrics.

The crystal structure and electronic structure investigation for the unique T net planar Sb–Sb interactions in Hf_5Sb_9 will be also presented, although Hf_5Sb_9 is metallic compound with poor thermoelectric performances.

Acknowledgements

First, I want to express my deep appreciation to my supervisor, Professor Kleinke, for his support and guidance during the past five years.

Second, it is wonderful for me to work with so many nice colleagues in the group. Many thanks to Jalil, Jean Paul, Katja, Shahab, Navid, Pingjian, Yanjie, Annie, Bryan, Tingting, Brent, Wiqar, Mykhailo, Mariya, Raj.

The last but not the least, I would like to thank for my advisory committee members and examiners: Professor Oakley, Professor Nazar, Professor Preuss, Professor Hill and Professor Mozharivshyj for their helpful comments and suggestions during my Ph.D. studies.

Table of Contents

| | |
|---|-----------|
| List of Figures | x |
| 1. Thermoelectric materials | 1 |
| 1.1 Introduction | 1 |
| 1.1.1 Thermoelectric phenomena | 1 |
| 1.1.2 Thermoelectric devices and applications | 2 |
| 1.2 Optimization of thermoelectric performances | 5 |
| 1.2.1 Figure-of-merit ZT and efficiency | 5 |
| 1.2.2 Seebeck coefficient | 7 |
| 1.2.3 Electrical conductivity | 7 |
| 1.2.4 Thermal conductivity | 8 |
| 1.3 Advanced thermoelectric materials | 10 |
| 1.3.1 CsBi ₄ Te ₆ | 10 |
| 1.3.2 AgPb _m SbTe _{2+m} | 11 |
| 1.3.3 Tl ₉ BiTe ₆ and Tl ₂ SnTe ₅ | 12 |
| 1.3.4 Antimonides | 14 |
| References | 16 |
| 2. Experimental techniques and physical property characterizations | 18 |
| 2.1 Synthesis techniques | 18 |
| 2.1.1 Sample preparations | 19 |
| 2.1.2 Different techniques | 20 |
| 2.2 Analysis techniques | 23 |
| 2.2.1 Powder X-ray diffraction | 23 |
| 2.2.2 Single crystal structure determination | 25 |
| 2.2.3 Energy dispersive X-ray (EDX) analysis | 27 |
| 2.2.4 Thermal analysis | 28 |
| 2.3 Physical property measurements | 30 |
| 2.3.1 Seebeck coefficient measurement | 30 |
| 2.3.2 Electrical conductivity measurement | 32 |
| 2.3.3 Thermal conductivity measurement | 33 |

| | |
|--|-----------|
| 2.4 Electronic structure calculations | 34 |
| 2.4.1 LMTO | 34 |
| 2.4.2 Gaussian03 | 35 |
| References | 36 |
| 3. New oxides | 38 |
| 3.1 Synthesis, structure and physical properties of the new layered oxide $\text{Na}_2\text{Cu}_2\text{TeO}_6$ | 40 |
| 3.1.1 Introduction | 40 |
| 3.1.2 Synthesis and phase analysis | 40 |
| 3.1.3 Crystal structure | 43 |
| 3.1.4 Electronic structure calculation | 45 |
| 3.1.5 Physical properties | 46 |
| 3.2 Ternary oxides with Mo clusters: $\text{LaMo}_8\text{O}_{14}$ and $\text{Pb}_{0.69}\text{Mo}_4\text{O}_6$ | 47 |
| 3.2.1 Introduction | 47 |
| 3.2.2 Synthesis and phase analysis | 49 |
| 3.2.3 Crystal structures of two molybdenum oxides | 51 |
| 3.2.4 Electronic structure investigation | 55 |
| 3.2.5 Transport property measurements | 57 |
| 3.2.6 Conclusion | 61 |
| References | 62 |
| 4. Ternary thallium chalcogenides | 64 |
| 4.1 Synthesis and single crystal structure determination of new compounds | 65 |
| 4.1.1 Synthesis | 65 |
| 4.1.2 Single crystal structure determination | 66 |
| 4.2 Crystal structures | 68 |
| 4.3 Electronic structures | 74 |
| 4.3.1 Model descriptions | 74 |
| 4.3.2 Calculation results | 74 |
| 4.4 Physical property measurements | 77 |
| 4.4.1 $\text{Tl}_{2.35}\text{Sb}_{8.65}\text{Se}_{14}$, $\text{Tl}_{1.93}\text{Sb}_{8.07}\text{Se}_{13}$ and $\text{Tl}_{2.04}\text{Bi}_{7.96}\text{Se}_{13}$ | 77 |
| 4.4.2 Tl_2SnSe_3 and Tl_2SnTe_3 | 83 |
| 4.5 Conclusion | 86 |

| | |
|--|------------|
| References | 87 |
| 5. Electronic structure investigation of unusual Sb-Sb bonding in high temperature thermoelectric materials | 89 |
| 5.1 Introduction | 89 |
| 5.2 Theoretical methodology | 90 |
| 5.3 Results and discussion | 92 |
| 5.3.1 β -Zn ₄ Sb ₃ | 92 |
| 5.3.2 Filled skutterudites | 97 |
| 5.3.3 Yb ₁₄ MnSb ₁₁ | 102 |
| 5.3.4 Mo ₃ Sb ₇ | 106 |
| 5.3.5 Hf ₅ Sb ₉ | 112 |
| 5.4 Conclusion | 119 |
| References | 121 |
| Appendix | 124 |

List of Figures

| | |
|--|----|
| Figure 1.1 Power Generation based on the Seebeck effect (left) and Refrigeration based on the Peltier effect (right). | 2 |
| Figure 1.2 a. Power generator module; b. Refrigerator module; c. State-of-the-art thermoelectric devices. | 3 |
| Figure 1.3 Lunch box with thermoelectric technologies. | 4 |
| Figure 1.4 Comparison of thermoelectric properties between insulator, semiconductor and metal. | 6 |
| Figure 1.5 Crystal structure of CsBi ₄ Te ₆ . Cs: black; Bi: cyan; Te: red. | 11 |
| Figure 1.6 Crystal structure of AgPb _m SbTe _{2+m} . Ag: Green; Pb: black; Sb: cyan; Te: red. | 12 |
| Figure 1.7 Crystal structure of Tl ₅ Te ₃ . Tl: black; Te: red. | 13 |
| Figure 1.8 Crystal structure of Tl ₂ SnTe ₅ . Tl: black, Sn: green, and Te: red. | 14 |
| Figure 2.1 Various vessels for solid state reactions: a. Al ₂ O ₃ boat; b. Quartz tube with the sample inside; c. Mo crucible; d. Ta crucibles. | 20 |
| Figure 2.2 Tube furnace (left); box furnace with the gas flow (right). | 21 |
| Figure 2.3 High temperature furnace with the Diffstak Mk2 diffusion oil pump | 21 |
| Figure 2.4 Induction furnace. | 22 |
| Figure 2.5 X-ray diffraction from lattice planes. | 24 |
| Figure 2.6 Apex CCD in the Department of Chemistry at University of Waterloo. | 26 |
| Figure 2.7 EDX spectrum and summary of the results. | 27 |
| Figure 2.8 Schematic DSC curve. | 29 |
| Figure 2.9 Seebeck Measurement System in our laboratory. | 30 |
| Figure 2.10 Sample stage for the Seebeck measurement with the sample (black) and reference (red). | 31 |
| Figure 2.11 Four-point probe method. | 32 |
| Figure 3.1 CoO ₂ -based TE oxides: (a) Na _x CoO ₂ , (b) Ca ₃ Co ₄ O ₉ , (c) Bi ₂ Sr ₂ Co ₂ O _y . | 38 |
| Figure 3.2 Schematic illustration of contributions from different layers of cobalt oxides for good thermoelectric properties | 39 |
| Figure 3.3 Scanning Electron Microscope picture of Na ₂ Cu ₂ TeO ₆ crystals and EDAX analysis | 41 |
| Figure 3.4 Thermal analysis for the Na ₂ Cu ₂ TeO ₆ . | 42 |

| | |
|---|----|
| Figure 3.5 Crystal structure of $\text{Na}_2\text{Cu}_2\text{TeO}_6$. Na: black; Cu: blue; Te: purple; O: red. | 43 |
| Figure 3.6 $\frac{2}{\infty}[\text{Cu}_2\text{TeO}_6]$ layer of $\text{Na}_2\text{Cu}_2\text{TeO}_6$. | 44 |
| Figure 3.7 Band structure and densities of states of $\text{Na}_2\text{Cu}_2\text{TeO}_6$. | 45 |
| Figure 3.8 Mo clusters in a. LaMo_5O_8 , b. $\text{Y}_4\text{Mo}_4\text{O}_{11}$, c. $\text{Pr}_4\text{Mo}_9\text{O}_{18}$, d. $\text{La}_5\text{Mo}_{32}\text{O}_{54}$. | 48 |
| Figure 3.9 Band structure and densities of states of $\text{Y}_4\text{Mo}_4\text{O}_{11}$. | 49 |
| Figure 3.10 Two bicapped Mo_8 clusters in $\text{LaMo}_8\text{O}_{14}$. <i>Cis</i> (left) and <i>Trans</i> (right). | 52 |
| Figure 3.11 Basic $\text{Pb}_{0.69}\text{Mo}_4\text{O}_6$ structure obtained from the main reflections. The Pb atoms exhibit a split position around (0, 0, 0). | 54 |
| Figure 3.12 Modulated description of the structure. Thermal ellipsoids are indicated. | 55 |
| Figure 3.13 Band structure of $\text{LaMo}_8\text{O}_{14}$. | 56 |
| Figure 3.14 Band structure of $\text{Pb}_{0.75}\text{Mo}_4\text{O}_6$. | 57 |
| Figure 3.15 Electrical resistivity measurement of $\text{LaMo}_8\text{O}_{14}$. | 58 |
| Figure 3.16 Seebeck coefficient measurement of $\text{LaMo}_8\text{O}_{14}$. | 59 |
| Figure 3.17 Electrical resistivity measurement of $\text{Pb}_{0.69}\text{Mo}_4\text{O}_6$. | 60 |
| Figure 3.18 Seebeck coefficient measurement of $\text{Pb}_{0.69}\text{Mo}_4\text{O}_6$. | 61 |
| Figure 4.1 Crystal structure of $\text{Tl}_{2.35}\text{Sb}_{8.65}\text{Se}_{14}$ viewed along the <i>b</i> axis. Tl: black; Sb: cyan; Se: red. | 68 |
| Figure 4.2 Coordination spheres of the three independent Tl sites of $\text{Tl}_{2.35}\text{Sb}_{8.65}\text{Se}_{14}$ with the disordered Sb atoms at the Tl1 and Tl3 sites | 69 |
| Figure 4.3 Crystal structure of $\text{Tl}_{2.04}\text{Bi}_{7.96}\text{Se}_{13}$ viewed along the <i>b</i> axis. Tl: black; Bi: cyan; Se: red. | 72 |
| Figure 4.4 Crystal structure of Tl_2SnTe_3 . Tl: black; Sn: cyan; Te: red. | 73 |
| Figure 4.5 Band structure (left) of $\text{Tl}_{2.5}\text{Sb}_{8.5}\text{Se}_{14}$ and its first Brillouin zone (right). | 75 |
| Figure 4.6 Computed densities of states of $\text{Tl}_{2.5}\text{Sb}_{8.5}\text{Se}_{14}$. | 75 |
| Figure 4.7 Computed densities of states of Tl_2SnTe_5 (left), Tl_2SnSe_3 (middle), and Tl_2SnTe_3 (right). | 76 |
| Figure 4.8 Infrared diffuse reflectance spectrum of $\text{Tl}_{2.35}\text{Sb}_{8.65}\text{Se}_{14}$. | 77 |
| Figure 4.9 Electrical conductivity of $\text{Tl}_{2.35}\text{Sb}_{8.65}\text{Se}_{14}$. | 78 |
| Figure 4.10 Electrical conductivity of $\text{Tl}_{1.93}\text{Sb}_{8.07}\text{Se}_{13}$. | 79 |
| Figure 4.11 Plot of $\ln(\sigma)$ versus $1/T$ for $\text{Tl}_{2.35}\text{Sb}_{8.65}\text{Se}_{14}$. | 80 |
| Figure 4.12 Plot of $\ln(\sigma)$ versus $1/T$ for $\text{Tl}_{1.93}\text{Sb}_{8.07}\text{Se}_{13}$. | 81 |

| | |
|---|-----|
| Figure 4.13 Seebeck coefficient of $\text{Tl}_{2.35}\text{Sb}_{8.65}\text{Se}_{14}$. | 82 |
| Figure 4.14 Seebeck coefficient of $\text{Tl}_{1.93}\text{Sb}_{8.07}\text{Se}_{13}$. | 82 |
| Figure 4.15 Electrical conductivity of Tl_2SnSe_3 . | 83 |
| Figure 4.16 Plot of $\ln(\sigma)$ versus $1/T$ for Tl_2SnSe_3 . | 84 |
| Figure 4.17 Electrical conductivity of Tl_2SnTe_3 . | 85 |
| Figure 4.18 Seebeck coefficient of Tl_2SnTe_3 . | 85 |
| Figure 5.1 Crystal structure of $\beta\text{-Zn}_4\text{Sb}_3$ ($R\bar{3}c$). Zn: cyan; Sb: red. | 93 |
| Figure 5.2 MO diagram of the Sb_2^{4-} unit of $\beta\text{-Zn}_4\text{Sb}_3$. | 94 |
| Figure 5.3 MO diagram of the Sb_4^{8-} unit of $\beta\text{-Zn}_4\text{Sb}_3$. | 95 |
| Figure 5.4 Densities of states (left) and Sb–Sb crystal orbital Hamilton populations (right) of Zn_6Sb_5 . | 97 |
| Figure 5.5 Crystal structure of $\text{LaRu}_4\text{Sb}_{12}$ ($Im\bar{3}$). La: black; Ru: cyan; Sb: red. | 98 |
| Figure 5.6 MO diagram of the Sb_4^{4-} unit of $\text{LaRu}_4\text{Sb}_{12}$. | 99 |
| Figure 5.7 Band structure of $\text{LaRu}_4\text{Sb}_{12}$. | 100 |
| Figure 5.8 Densities of states (left) and Sb–Sb crystal orbital Hamilton populations (right) of $\text{LaRu}_4\text{Sb}_{12}$. | 101 |
| Figure 5.9 Crystal structure of $\text{Ca}_{14}\text{AlSb}_{11}$ ($I4_1/acd$). Ca: black; Al: cyan; Sb: red. | 103 |
| Figure 5.10 MO diagram of the Sb_3^{7-} unit of $\text{Ca}_{14}\text{AlSb}_{11}$. | 104 |
| Figure 5.11 Densities of states (left) and Sb–Sb crystal orbital Hamilton populations (right) of $\text{Ca}_{14}\text{AlSb}_{11}$. | 106 |
| Figure 5.12 Crystal structure of Mo_3Sb_7 ($Im\bar{3}m$). Mo: black; Sb: red. | 107 |
| Figure 5.13 Three-dimensional network of Sb cubes of Mo_3Sb_7 . | 108 |
| Figure 5.14 Band structure of Mo_3Sb_7 . | 109 |
| Figure 5.15 Densities of states (left) and Sb–Sb crystal orbital Hamilton populations (right) of Mo_3Sb_7 . | 110 |
| Figure 5.16 Densities of states of $\text{Mo}_3\text{Sb}_5\text{Te}_2$ (left) and $\text{Ni}_{0.5}\text{Mo}_3\text{Sb}_5\text{Te}_2$ (right). | 111 |
| Figure 5.17 Crystal structure of Hf_5Sb_9 . Hf: black; Sb: red. Hf1 is highlighted; the other black atoms are Hf2. | 113 |
| Figure 5.18 T net of Hf_5Sb_9 . | 114 |
| Figure 5.19 Band structure of Hf_5Sb_9 , with emphasis on the Sb3 p_y contributions. | 115 |

| | |
|--|-----|
| Figure 5.20 Densities of states (left) and Hf–Sb crystal orbital Hamilton population (right) curves. | 116 |
| Figure 5.21 MO diagram comparison of Sb_8^{16-} units. | 117 |
| Figure 5.22 Temperature dependence of the thermoelectric figure-of-merit, ZT , for selected p -type antimonides. | 119 |

1. Thermoelectric materials

1.1 Introduction

Nowadays, there is an urgent need for the alternatives of the energy utilization because of the depletion of the energy resources on our planet. Thermoelectric materials, which can realize the energy conversion between heat and electricity, might be potential candidates. Thermoelectric phenomena were discovered in the 19th century. However, practical applications for thermoelectric devices became feasible only after mid-20th century because of advancements in the semiconductor technologies. After two decades, there was no breakthrough discovery in the thermoelectrics. But this field is experiencing a re-discovery for several reasons: First, current environmental concern requires new alternative materials to be able to do green energy conversion. Second, modern advanced techniques make it possible to synthesize many new compounds with complex structures and characterize their properties. Last but not least, reliable theoretical calculations by powerful computers are now available for predicting and understanding properties of materials, which makes the selection of the new materials much easier.

1.1.1 Thermoelectric phenomena

In 1821, Thomas Johann Seebeck [1] found that an electric current would flow continuously in a closed circuit made up of two different metals, if the junctions of the metals were maintained at two different temperatures, as shown in Figure 1.1 (left). This effect could have power-generation applications, which are currently popular in the automotive industries for utilizing the waste engine heat from exhaust systems.

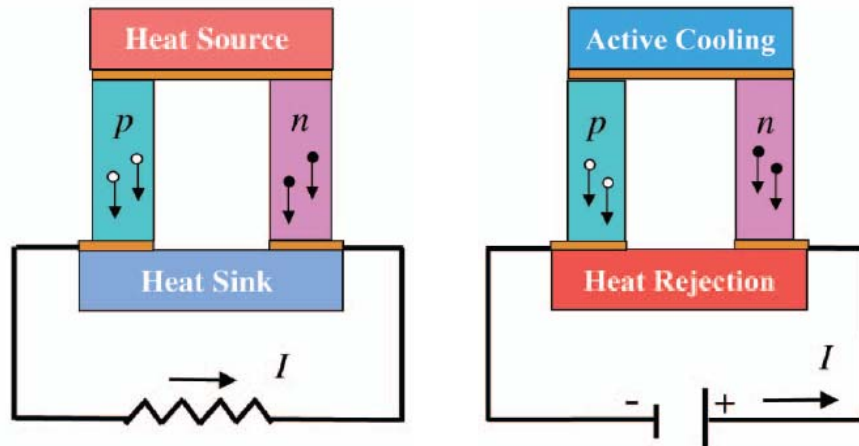


Figure 1.1 Power Generation based on the Seebeck effect (left) and Refrigeration based on the Peltier effect (right) [2].

It was later in 1834 that Jean Peltier [1] found that an electrical current would produce a temperature gradient at the junction of two different metals, which is the reverse of the Seebeck effect (Figure 1.1 right). The Peltier effect, on the other hand, serves as an idea for the thermoelectric refrigeration to replace the old cooling systems.

1.1.2 Thermoelectric devices and applications

Employing the Seebeck effect, thermoelectric power generators convert heat energy to electricity as shown in Figure 1.2a. When a temperature gradient is created across the thermoelectric device, a voltage gradient appears across the terminals. One of the well-known applications is the thermocouple for measuring the temperatures. Other applications for this technology include providing the power for the remote telecommunication, space probes and waste heat recovery for automotives.

When a voltage gradient is applied to a thermoelectric module, the positive and negative charge carriers in the pellet array absorb heat energy from one substrate surface and release it

to the substrate at the opposite side (Figure 1.2b). Using this simple approach to heat pumping, thermoelectric technology is applied to many widely varied applications: portable refrigerators, scientific thermal conditioning and so forth.

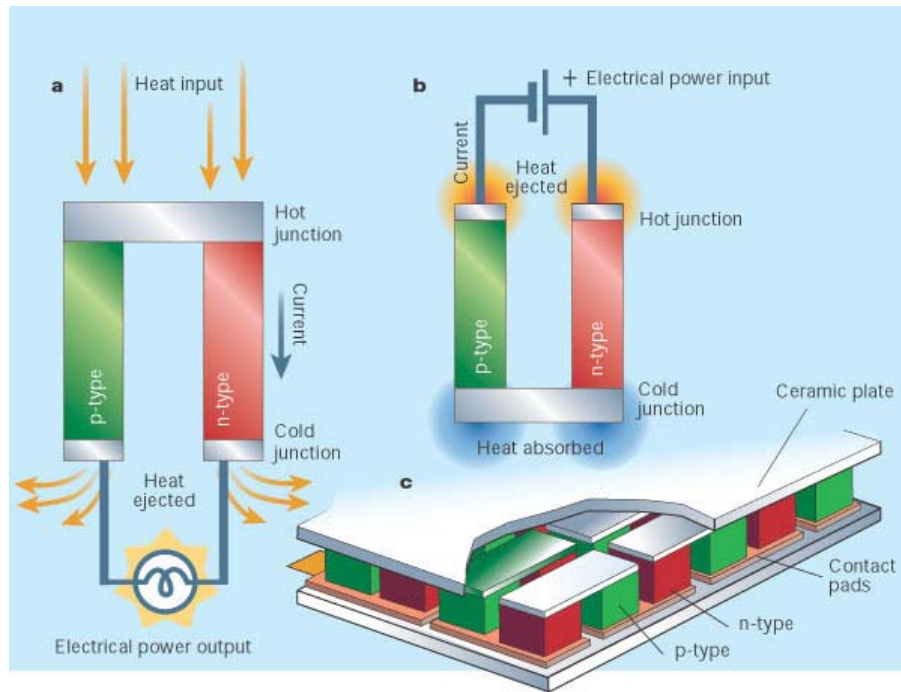


Figure 1.2 a. Power generator module; b. Refrigerator module; c. State-of-the-art thermoelectric devices [3].

A typical thermoelectric module, shown in Figure 1.2c, consists of semiconductor pellets that have been doped so that there is only one type of charge carrier. The n-type or p-type pellets are arranged in order to be connected electrically in series, but thermally in parallel.

Figure 1.3 shows a portable lunch box based on thermoelectric modules by NASA. So theoretically, e.g. by utilizing the Peltier effect, we can keep our hot dishes at the hot side and cold dishes at the cold side during the travel. The LCD monitor even allows us to set the exact temperature.



Figure 1.3 Lunch box with thermoelectric technologies [4].

1.2 Optimization of thermoelectric performances

As we discussed about thermoelectric devices above, it is easy to see that thermoelectric devices have many advantages, such as high reliability, no-moving parts, efficiency independent of size and environmentally friendly, compared with conventional cooling systems. However, thermoelectric materials have not been widely used in commercial applications because of the low efficiency.

1.2.1 Figure-of-merit ZT and efficiency

The major goal of thermoelectric material research is to design materials that will improve the efficiency of these solid-state devices. The efficiency (η) [5] of thermoelectric materials for power generation is defined as the output of electrical power (P) divided by the thermal power (Q) supplied:

$$\eta = \frac{P}{Q} = \frac{T_H - T_C}{T_H} \frac{\sqrt{1 + ZT} - 1}{\sqrt{1 + ZT} + \frac{T_C}{T_H}} \quad (1-1)$$

T_H and T_C are referring to the temperature of the hot and cold sides of the sample, respectively. Efficiency depends on material properties through the dimensionless figure of merit ZT [6]:

$$ZT = T \frac{S^2 \sigma}{\kappa} \quad (1-2)$$

where T is the average temperature of the sample, S is the thermopower or Seebeck coefficient, σ is the electrical conductivity and κ is the total thermal conductivity. High ZT

will lead to high efficiency. From the equation above, we can easily see that high ZT values can be achieved with a high Seebeck value (S) and high electrical conductivity (σ), but low thermal conductivity (κ). Unfortunately, these thermoelectric parameters can not be treated independently and the correlations between them are rather complicated. Before we look into details of each parameter, let us have a look at what kind of materials might be good candidates for thermoelectric applications.

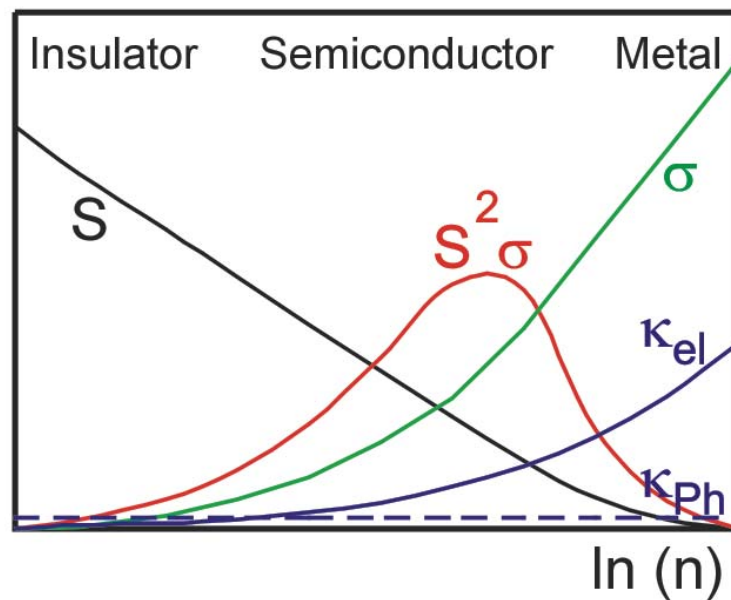


Figure 1.4 Comparison of thermoelectric properties between insulator, semiconductor and metal.

As shown in Figure 1.4, insulators have high Seebeck coefficient but no electrical conductivity, and metals have high electrical conductivity but low Seebeck coefficient, and thus they are not good thermoelectric materials. The best thermoelectric materials are predicted to be semiconductors with small band gaps [1].

1.2.2 Seebeck coefficient

The Seebeck coefficient, e.g. thermopower, with a unit of (V/K) is a measure of the magnitude of an induced thermoelectric voltage in response to a temperature difference across that material:

$$S = \frac{\Delta V}{\Delta T} \quad (1-3)$$

The Seebeck coefficient can be derived from the Mott equation [7,8] with σ = electrical conductivity, k = Boltzmann constant, T = temperature, e = charge of an electron, and E = energy:

$$S = \frac{\pi^2}{3} \frac{k^2 T}{e} \left. \frac{d \ln \sigma(E)}{dE} \right|_{E=E_F} \quad (1-4)$$

One can deduce from the Mott equation that the Seebeck coefficient is inversely proportional to the DOS at Fermi level and directly proportional to the derivative of the DOS at Fermi level, i.e. large DOS are disadvantageous for a high Seebeck coefficient and flat band will be beneficial for a large Seebeck coefficient [9] :

$$S \propto \frac{1}{\text{DOS}(E_F)} \left. \frac{d \text{DOS}(E)}{dE} \right|_{E=E_F} \quad (1-5)$$

1.2.3 Electrical conductivity

Electrical conductivity (σ) is a measure of a material's ability to conduct an electric current, which is defined as [10]:

$$\sigma = \frac{L}{R \times A} \quad (1-6)$$

where R is the resistance of the sample, A and L being the cross area and length, respectively. A and L are constant for any experiment with fixed contacts. Electrical conductivity can also be explained by the equation [11] below:

$$\sigma = n \times e \times \mu \quad (1-7)$$

with n = the charge carrier concentration, e = charge of an electron and μ = mobility. Generally, materials containing elements with small electronegativity differences are more likely to have higher mobility, e.g., electrons are more delocalized in these materials, leading to the high electrical conductivity.

1.2.4 Thermal conductivity

Thermal conductivity, κ , is the ability of a material to conduct the heat, which has two contributions, one from the electrical charge carriers, κ_e , and the other from the lattice vibrations (phonons), κ_{ph} . The overall thermal conductivity is the sum of the contributions by both charge carriers and phonons:

$$\kappa = \kappa_e + \kappa_{ph} \quad (1-8)$$

For metals, the high thermal conductivity is the contribution of large numbers of electrons as charge carriers. Hence, the electronic contribution (κ_e) has the major impact for the thermal conductivity in metals, while the lattice vibrations have smaller effect. According to the Wiedemann-Franz relation [10], the thermal conductivity is proportional to the electrical conductivity for the metals at a certain temperature ($L = 2.45 \times 10^{-8} \text{ W}\Omega\text{K}^{-2}$):

$$\kappa_e = L \times \sigma \times T \quad (1-9)$$

On the other hand, in semiconductors κ_{ph} is usually much greater than κ_e . Since the best thermoelectric materials were predicted to be semiconductors with small band gaps, one challenge is to minimize κ_{ph} . One way to do this is to synthesize compounds by using heavy elements. High atomic masses can reduce the atomic vibration frequencies resulting in lower thermal conductivity. This is one of the reasons that the elements like antimony, bismuth, tellurium, and lead are used quite often for current thermoelectric research. Another way is to introduce so-called “guest” atoms into the voids of the skutterudites [12-14] with CoAs_3 [15] structure type. These small “guest” atoms act like strong phonon scattering centers to reduce the lattice thermal conductivity dramatically, resulting in excellent thermoelectric properties.

1.3 Advanced thermoelectric materials

During the search for good thermoelectric materials since 1950s, some material systems stand out with the high potential for achieving excellent thermoelectric performances. These materials contain the high electrical conductivity and thermopower, while maintaining the relatively low thermal conductivity. In the following, we will discuss some advanced thermoelectric materials, and some of them are highly related to my research project as well.

1.3.1 CsBi₄Te₆

Chalcogenides comprise a large number of materials with complex structures and semiconducting behavior. Most of them are stable in the air in a wide temperature range. Because of the multiple choices of chalcogen elements e.g. from sulfur to tellurium, it is highly possible to obtain semiconductors with different energy gaps which are suitable for thermoelectric applications in a wide range of temperature. Since the early stages, chalcogenides were considered to be one of the best material classes for thermoelectric applications. Bi₂Te₃ and its variants like Bi_{2-x}Sb_xTe₃ and Bi₂Te_{3-x}Se_x [16] still holding the record for thermoelectric performances around room temperature. Another important chalcogenide is PbTe [17], with a maximum ZT value of 0.8 at 773 K [18].

In 2000, CsBi₄Te₆ [19] derived from Bi₂Te₃, with appropriate p-type doping of SbI₃ or Sb, was reported to have a high ZT of 0.8 at 225 K, which is highest among all reported thermoelectric materials at that low temperature.

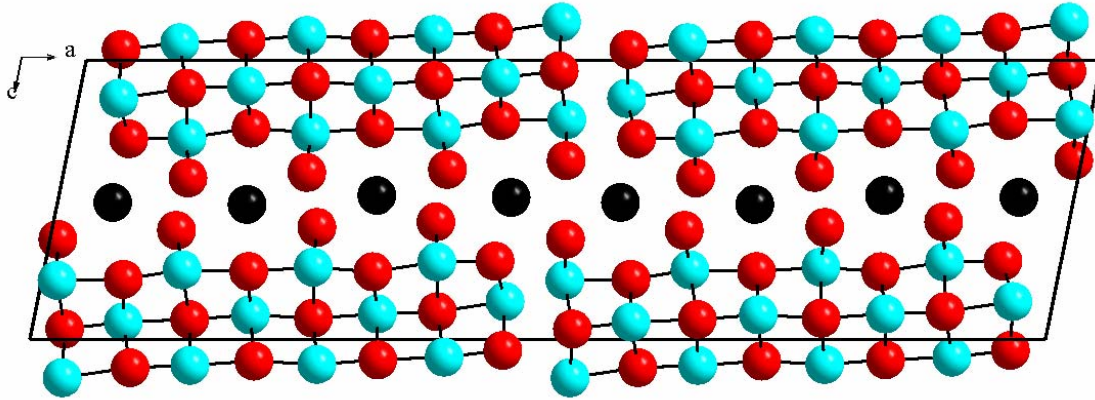


Figure 1.5 Crystal structure of CsBi₄Te₆. Cs: black; Bi: cyan; Te: red.

CsBi₄Te₆ crystallizes in a monoclinic crystal system with the space group $C2/m$ and presents a new structure type consisting of anionic infinite Bi₄Te₆⁻ blocks and Cs⁺ ions residing between the layers, as shown in Figure 1.5. Different doping materials might allow the figure of merit, ZT, to be shifted to even lower temperatures [20]. CsBi₄Te₆ is the example to make the extension for the use of thermoelectric materials to lower temperatures.

1.3.2 AgPb_mSbTe_{2+m}

AgPb_mSbTe_{2+m} is another chalcogenide with outstanding thermoelectric performances. A lot of compounds with different compositions can be obtained with different m values. The cubic AgPb₁₈SbTe₂₀ [21] was discovered to have $ZT \approx 2.2$ at 800 K, which outperformed all reported bulk materials in the temperature range of 600 to 900 K. This family of compounds presents an average NaCl structure like PbTe [17] with the mixed occupations of Ag, Sb and Pb [22], schematically shown in Figure 1.6.

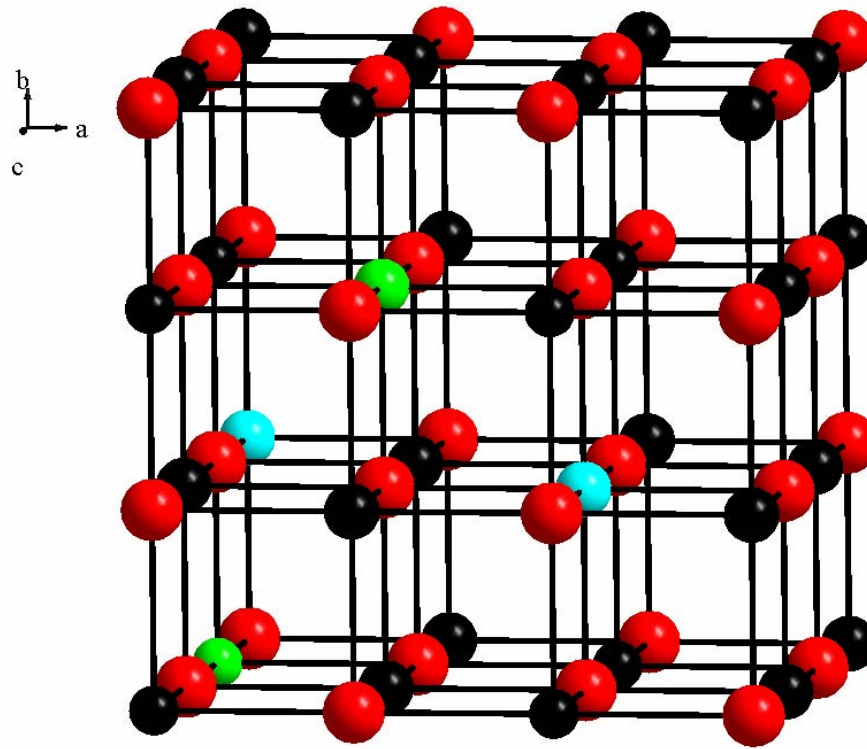


Figure 1.6 Crystal structure of $\text{AgPb}_m\text{SbTe}_{2+m}$. Ag: Green; Pb: black; Sb: cyan; Te: red.

However, recent work [23] on $\text{AgPb}_m\text{SbTe}_{2+m}$ by Transmission Electron Microscopy (TEM) revealed the nano-structural features of this compound. Research on the impact and significance of nano features for improving of thermoelectric properties is still in progress.

1.3.3 Tl_9BiTe_6 and Tl_2SnTe_5

Recently, thallium chalcogenides such as Tl_9BiTe_6 [24] and Tl_2SnTe_5 [25] have been found to have excellent thermoelectric properties with extremely low thermal conductivities at room temperature, e.g., $0.39 \text{ Wm}^{-1}\text{K}^{-1}$ for Tl_9BiTe_6 and $0.5 \text{ Wm}^{-1}\text{K}^{-1}$ for Tl_2SnTe_5 . Tl_9BiTe_6 can be derived from the binary compound, Tl_5Te_3 [26,27] with the mixed

occupancy of Tl/Bi at the 4c site (Figure 1.7). Tl_9BiTe_6 exhibits the figure of merit of $ZT \approx 1.2$ at 500 K.

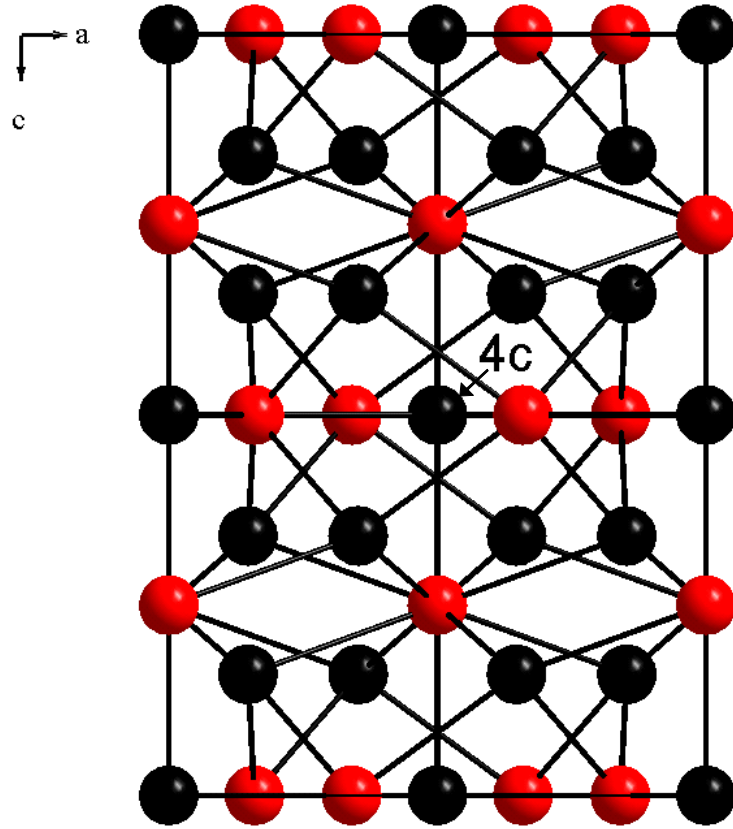


Figure 1.7 Crystal structure of Tl_5Te_3 . Tl: black; Te: red.

Tl_2SnTe_5 also forms a the tetragonal crystal structure, with chains of SnTe_5^{2-} parallel to the c -axis to and the cation Tl^+ filling in the eight-coordinated voids shown in Figure 1.8. Tl–Te bonds (3.49 Å) in Tl_2SnTe_5 are relatively long compared with that of Tl_5Te_3 ranging from 3.15 to 3.36 Å. Such long bonds could produce very low-frequency phonons, which might be one of the key reasons for Tl_2SnTe_5 to have that low thermal conductivity resulting in a ZT

of 1 at 500 K. More information about thallium chalcogenides for thermoelectric applications will be disclosed in Chapter 3.

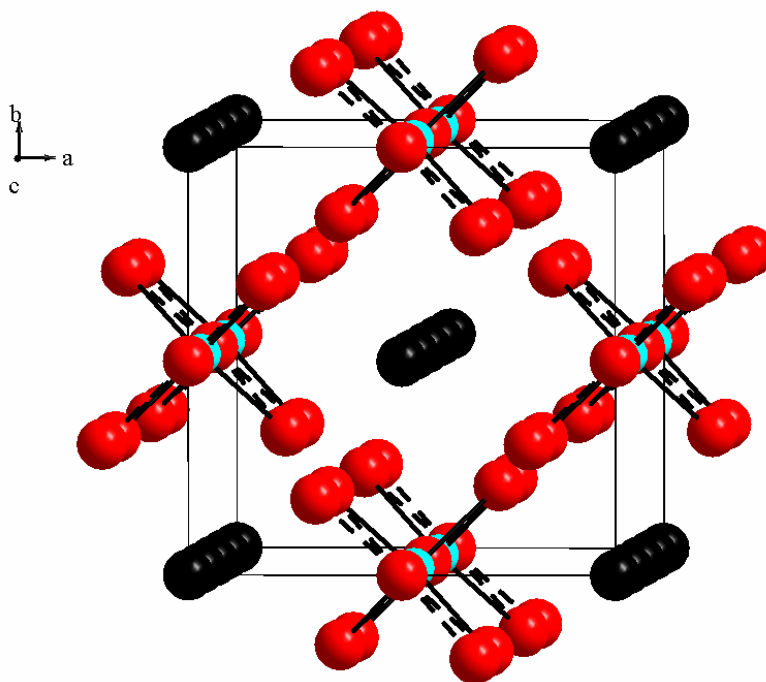


Figure 1.8 Crystal structure of Tl_2SnTe_5 . Tl: black, Sn: cyan, and Te: red.

1.3.4 Antimonides

Antimonides have also attracted wide interest for thermoelectric applications. The antimony anions in antimonides participate in much more complicated structures than tellurium anions do in chalcogenides. Since in Chapter 5 I will introduce my research efforts of electronic structure calculations for the investigation of Sb–Sb bonding in several advanced thermoelectric antimonides, only a brief review about their outstanding thermoelectric properties will be given in this section.

Starting with the binary compound, Zn_4Sb_3 there are three modifications for this compound. β - Zn_4Sb_3 was considered to be one of the best p -type thermoelectric materials around 700 K, the other two phases being α and γ [28]. The highest ZT value reported for β - Zn_4Sb_3 is 1.4 at 673 K [29]. The filled skutterudites with the general formula LnM_4Sb_{12} (Ln = lanthanoid; M = transition metals such Fe, Co, Ni, etc.) as a phonon-glass-electron crystal material [30], help us to understand the mechanism for lowering thermal conductivity. The parent compound, $LaFe_4Sb_{12}$ [31] is a metal, while $LaFe_3CoSb_{12}$ and $CeFe_3CoSb_{12}$ [32,33] were reported to be p -type and n -type specimens with $ZT \approx 1$ at 800 K. $Yb_{14}MnSb_{11}$ [34] was reported recently to break the two decades record of thermoelectric performances above 975 K, with the Figure of Merit, $ZT \approx 1$ at 1223 K. Since the late 90s, our research group has developed several interesting early transition metal antimonides [35-39]. Some of them with Ir_3Ge_7 structure type [40] were very promising candidates for the future thermoelectric applications, e.g., $Ni_{0.06}Mo_3Sb_{5.4}Te_{1.6}$ reaches $ZT \approx 1$ at 1050 K [41].

There is also another material system, oxides, of particular interests for the thermoelectric applications. Since it is part of my research project, the details will be introduced in the chapter 3.

References

- [1] Rowe, D. M. *CRC Handbook of Thermoelectrics*; CRC Press: Boca Raton, FL, 1995.
- [2] Tritt, T. M.; Subramanian, M. A. *Mat. Res. Bull.* **2006**, *31*, 188-198.
- [3] Vining, C. B. *Nature* **2001**, *413*, 557-558.
- [4] <http://gizmodo.com/gadgets/space-cooler>
- [5] Snyder, G. J.; Ursell, T. S. *Phys. Rev. Lett.* **2003**, *91*, 148301-148304.
- [6] DiSalvo, F. J. *Science* **1999**, *285*, 703-706.
- [7] Mott, N. F.; Jones, H. *The Theory of the Properties of Metals and Alloys*; Dover Publication: New York, NY, 1958.
- [8] Mahan, G. D.; Sofo, J. O. *Proc. Natl. Acad. Sci.* **1996**, *93*, 7436-7439.
- [9] Rao, A.; Ji, X.; Tritt, T. M. *Mat. Res. Bull.* **2006**, *31*, 218-223.
- [10] Kittel, C. *Introduction to Solid State Physics*; 7th ed.; John Wiley & Sons Inc.: New York, 1996.
- [11] Pollock, D. D. *"Thermoelectricity" Theory, Thermometry, Tool*; ASTM Publications: Philadelphia, PA, 1985.
- [12] Uher, C. *Semiconductors and Semimetals*; Academic Press: New York, 2000; Vol. 69.
- [13] Nolas, G. S.; Morelli, D. T.; Tritt, T. M. *Annu. Rev. Mater. Sci.* **1999**, *29*, 89-116.
- [14] Sales, B. C. *Handbook of the Physics and Chemistry of Rare Earths*; Elsevier Science: Amsterdam, 2002; Vol. 33.
- [15] Mandel, N.; Donohue, J. *Acta Crystallogr. B* **1971**, *27*, 2288-2289.
- [16] Nolas, G. S.; Sharp, J.; Goldsmid, H. J. *Thermoelectrics: Basic Principles and New Materials Developments*; Springer: New York, 2001.
- [17] Rousse, G.; Klotz, S.; Saitta, A. M.; Rodriguez-Carvajal, J.; McMahan, M. I.; Couzinet, B.; Mezouar, M. *Phys. Rev. B* **2005**, *71*, 224116-224116-224116-224116.
- [18] Nolas, G. S.; Poon, J.; Kanatzidis, M. G. *Mat. Res. Bull.* **2006**, *31*, 199-205.
- [19] Chung, D. Y.; Hogan, T. P.; Brazis, P.; Rocci-Lane, M.; Kannewurf, C. R.; Bastea, M.; Uher, C.; Kanatzidis, M. G. *Science* **2000**, *287*, 1024-1027.
- [20] Chung, D. Y.; Hogan, T. P.; Rocci-Lane, M.; Brazis, P.; Ireland, J. R.; Kannewurf, C. R.; Bastea, M.; Uher, C.; Kanatzidis, M. G. *J. Am. Chem. Soc.* **2004**, *126*, 6414-6428.
- [21] Hsu, K. F.; Loo, S.; Guo, F.; Chen, W.; Dyck, J. S.; Uher, C.; Hogan, T.; Polychroniadis, E. K.; Kanatzidis, M. G. *Science* **2004**, *303*, 818-821.
- [22] Sportouch, S.; Bastea, M.; Brazis, P.; Ireland, J. R.; Kannewurf, C. R.; Uher, C.; Kanatzidis, M. G. *Thermoelectric Materials 1998-The next Generation Materials for Small-Scale Refrigeration and Power Generation Applications*; Mat. Res. Soc. Symp. Proc.: Warrendale, PA, 1998; Vol. 545.
- [23] Quarez, E.; Hsu, K. F.; Pcionek, R.; Frangis, N.; Polychroniadis, E. K.; Kanatzidis, M. G. *J. Am. Chem. Soc.* **2005**, *127*, 9177-9190.
- [24] Wölfing, B.; Kloc, C.; Teubner, J.; Bucher, E. *Phys. Rev. Lett.* **2001**, *86*, 4350-4353.
- [25] Sharp, J. W.; Sales, B. C.; Mandrus, D. G.; Chakoumakos, B. C. *Appl. Phys. Lett.* **1999**, *74*, 3794-3796.
- [26] Bhan, S.; Schubert, K. *J. Less-Common Met.* **1970**, *20*, 229-235.
- [27] Schewe, I.; Böttcher, P.; Schnering, H. G. *Z. Kristallogr.* **1989**, *188*, 287-298.
- [28] Mayer, H. W.; Mikhail, I.; Schubert, K. *J. Less-Common Met.* **1978**, *59*, 43-52.
- [29] Caillat, T.; Fleurial, J. P.; Borshchevsky, A. *J. Phys. Chem. Solids* **1997**, *58*, 1119-1125.

- [30] Slack, G. A. *Mat. Res. Soc. Symp. Proc.* **1997**, 478, 47-54.
- [31] Braun, D. J.; Jeitschko, W. *J. Less-Common Met.* **1980**, 72, 147-156.
- [32] Fleurial, J. P.; Borshchevsky, A.; Caillat, T.; Morelli, D. T.; Meisner, G. P. *Proc. 15th Int. Conf. Thermoelectrics*; IEEE: Piscataway, NJ, 1996.
- [33] Sales, B. C.; Mandrus, D.; Williams, R. K. *Science* **1996**, 272, 1325-1328.
- [34] Brown, S. R.; Kauzlarich, S. M.; Gascoin, F.; Snyder, G. J. *Chem. Mater.* **2006**, 18, 1973-1877.
- [35] Kleinke, H. *Chem. Commun.* **1998**, 2219-2220.
- [36] Kleinke, H. *J. Mater. Chem.* **1999**, 9, 2703-2708.
- [37] Kleinke, H. *Inorg. Chem.* **1999**, 38, 2931-2935.
- [38] Kleinke, H. *J. Am. Chem. Soc.* **2000**, 122, 853-860.
- [39] Kleinke, H.; Ruckert, C.; Felser, C. *Eur. J. Inorg. Chem.* **2000**, 315-322.
- [40] Soheilnia, N.; Kleinke, H. *Z. Anorg. Allg. Chem.* **2006**, 623, 2082.
- [41] Xu, H.; Soheilnia, N.; Zhang, H.; Alboni, P. N.; Tritt, T. M.; Kleinke, H. *Mat. Res. Soc. Symp. Proc.* **2008**, in press.

2. Experimental techniques and physical property characterizations

2.1 Synthesis techniques

All of the samples were prepared by conventional solid state reactions, e.g., heating mixtures of two or more materials to form a solid phase product. Solid state materials may be one of three forms: 1. Single crystals, which are usually preferred for the structure determination and physical property characterizations; 2. Polycrystalline powder, which can be used for the structure and property characterizations if large enough crystals can not be obtained; 3. Amorphous phases, which do not have any long range order. Compared with gas and liquid phases, one of the key factors that inhibit solid state reactions is diffusion, which is expressed by Fick's law [1]:

$$J = -D \frac{dc}{dx} \quad (2-1)$$

where J = flux of diffusing species, D = diffusion coefficient and dc/dx = concentration gradient. In order to have good rates of reaction, the typical diffusion coefficient needs to be greater than $10^{-12} \text{cm}^2 \text{s}^{-1}$. Mostly, the higher the temperature, the greater will be the diffusion coefficient. Tamman's rule [2] concludes that intensive reaction will only occur when the reaction temperature reaches $2/3$ of the melting point of one or more reactants. As for different temperatures required, different kinds of equipments were employed for the synthesis. In this section, detailed information about solid state synthesis techniques in our laboratories will be introduced.

2.1.1 Sample preparations

Since most of starting materials for solid state reactions are sensitive to oxygen and moisture, they were usually stored in an argon or nitrogen filled glove box. The details about the starting materials for the synthesis are listed Table A. 1 in the Appendix. Most sample preparations, e.g., weighing stoichiometric reactants and transferring to the proper vessels, were also done in the glove box. Two different types of reactions can be classified depending on whether the atmosphere needs to be excluded or not. For the reactions in air, a ceramic boat made up of Al_2O_3 was used as the vessel. After the preparation, the ceramic boats were directly put into the furnaces for the reactions, which were usually ongoing either in the air or under oxygen flow. As for the reactions that need to exclude the presence of oxygen and moisture, different containers such as quartz tubes, Mo and Ta crucibles, were selected for the synthesis at different temperatures.

Quartz tubes consisting of SiO_2 are usually employed if the reaction temperature is below 1273 K. If some reactants tend to react with the quartz tube at high temperatures, Tamman crucibles (Al_2O_3) are often used to avoid contacts between samples and quartz tubes as shown in Figure 2.1. The vacuum needed for sealing the tubes was obtained by the home-made vacuum-line and BOC EDWARDS' rotary pump.

For high temperature (> 1473 K) reactions, Mo or Ta crucible are better choices instead of quartz tubes (SiO_2), since the melting points of Mo (2896 K) and Ta (3290 K) are much higher than SiO_2 (1710 K) [3]. Once the samples were sealed in the tubes or crucibles, they were loaded into different types of furnaces for the synthesis at different temperatures.

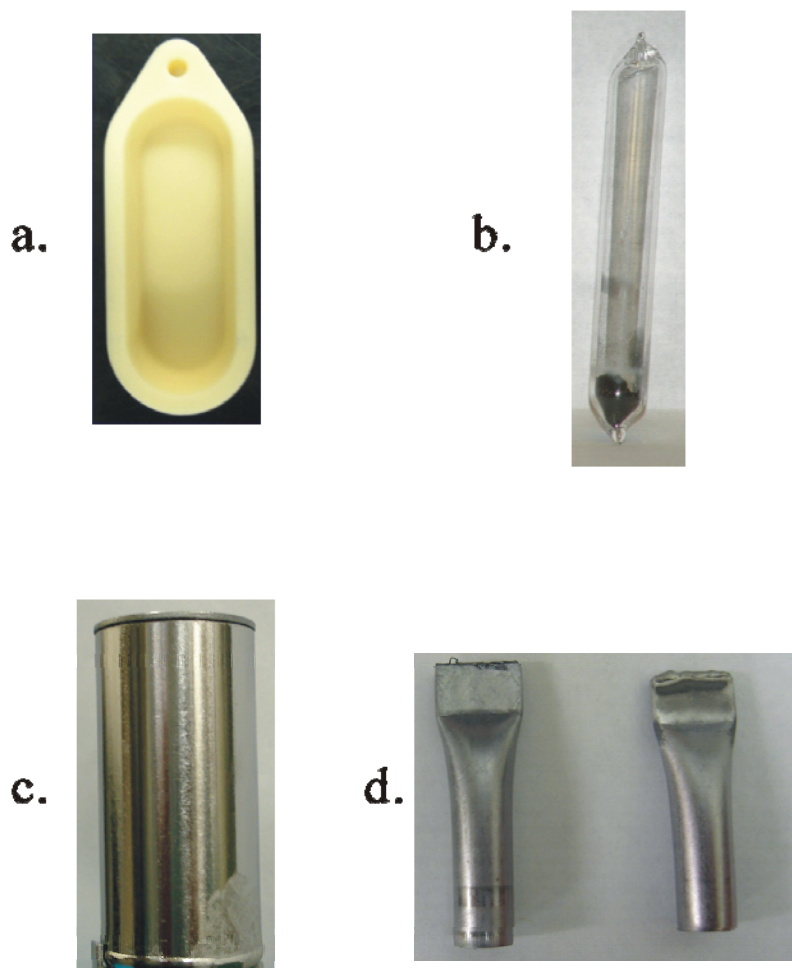


Figure 2.1 Various vessels for solid state reactions: a. Al₂O₃ boat; b. Quartz tube with the sample inside; c. Mo crucible; d. Ta crucibles.

2.1.2 Different techniques

According to different temperatures required for the synthesis, different equipments were employed. Oxygen and inert argon gas flow were applied for different needs of the environment for the reactions by utilizing the tube furnaces, as shown in the left of Figure 2.2. For the moderate temperature (< 1273 K) reactions, box furnaces (Figure 2.2 right) were

favourable. The designed annealing profiles can be set up in order to obtain good qualities of crystals within these furnaces.



Figure 2.2 Tube furnace (left); box furnace with the gas flow (right).

The high temperature furnaces (Figure 2.3) can be used for the reactions up to 1870 K, under high vacuum, e.g. 10^{-7} mbar, which can be obtained by the Diffstak Mk2 diffusion oil pump.



Figure 2.3 High temperature furnace with the Diffstak Mk2 diffusion oil pump.

Some compounds need even higher temperatures (up to 2273 K) for the synthesis, such as some molybdenum oxides that will be discussed in the next chapter. These high

temperature reactions were carried out in the induction furnace [4] (Figure 2.4), which is an electrical furnace in which the heat is applied by induction heating of a conductive medium (usually a metal) in a crucible.



Figure 2.4 Induction furnace.

2.2 Analysis techniques

After the products are synthesized, the next step is the analysis of the samples in order to obtain the structure information, determine phase purity and so forth. Several general analysis techniques utilized by our group as well as other solid state material scientists will be introduced in the following section.

2.2.1 Powder X-ray diffraction

X-rays were discovered in 1895 by German physicist Dr. Roentgen [5]. Before Dr. Bragg [6] discovered that X-rays were scattered by the internal lattices of solid objects, they were used for the medical applications, e.g., making images of the internal structure of bodies. X-rays are a form of electromagnetic radiation of very short wavelengths in the angstrom and nanometer region with typical energies in the range of 100 eV - 100 keV, and the wavelength of X-rays is comparable to the size of atoms. The elastic scattering made by the interactions between X-ray and electrons of atoms in the material is used for probing the structural arrangement of atoms and molecules in a wide range of materials.

The peaks in the X-ray diffraction pattern are indirectly related to the atomic distances, which may be explained by the Figure 2.5 [7], with the angle θ representing the scattering (Bragg) angle and d referring to the distances of a set of lattice planes.

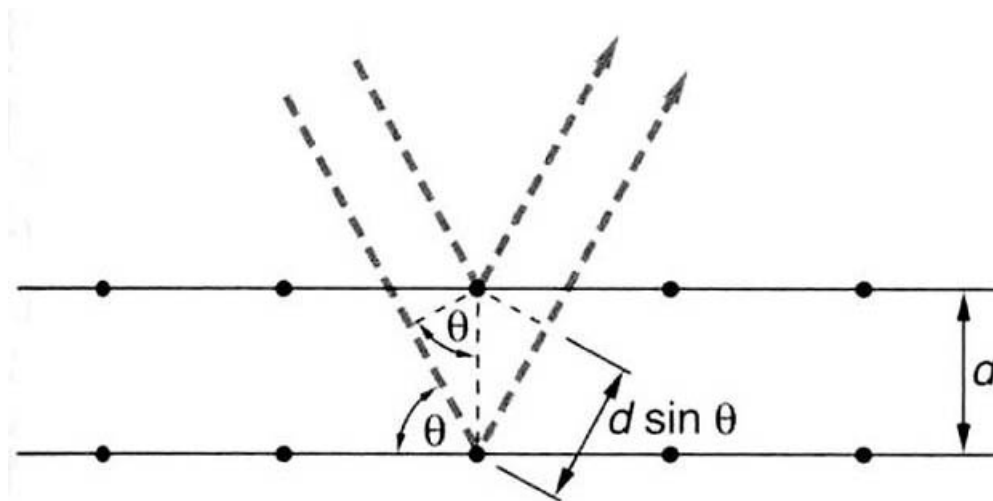


Figure 2.5 X-ray diffraction from lattice planes.

When two parallel X-rays hit on two atomic layers separated by a distance of d , obviously one beam must travel the extra distance of $2d\sin\theta$, which must be a multiple of the wavelength (λ) and integer (n) for the two beams to be in phase. Bragg's law [8] equation can be derived:

$$n\lambda = 2d \times \sin \theta \quad (2-2)$$

Since the peak positions in the Powder X-ray Diffraction (PXRD) pattern are related to the unit cell parameters as well as d values, and the intensities of the peaks are proportional to the square of atomic number of elements, i.e. the total number of electrons, the PXRD pattern can be regarded as the fingerprint for a certain compound. A sample with a powdery form for the measurement is usually easy to obtain, which makes PXRD one of the most widely used techniques for characterizing materials.

2.2.2 Single crystal structure determination

To solve a crystal structure means to determine the precise arrangements of all atoms in a chemical compound in the crystalline state, which include the positions of the atoms in that solid.

The first step is to select a suitable crystal. Generally, crystal dimensions greater than 0.5mm should be avoided, but the least thickness should be more than 0.01mm. The crystals are usually mounted on a glass fiber for the data collection. With new camera techniques, the equipment for collecting the data has been developed dramatically as well. Nowadays, area-detector systems are mainly used, which include two types: the Charge Coupled Device (CCD) and Image Plate [9].

In the Department of Chemistry at University of Waterloo, the data collection is performed on the Apex CCD with graphite-monochromatized Mo-K α_1 radiation (BRUKER) as shown in Figure 2.6.

The data collection and unit cell determination were done by using the SMART software [10]. After collecting the data, the raw data has to be corrected for Lorentz and polarization effects [11], which is part of the data reduction. This step will usually be done by using the SAINT program [12], followed by the space group determination with XPREP embedded in the SHELXTL package [13]. Absorption corrections are also needed, since the X-ray beam is weakened when it passes through the crystal. This process can be done by the program, SADABS [12] or XPREP [13].

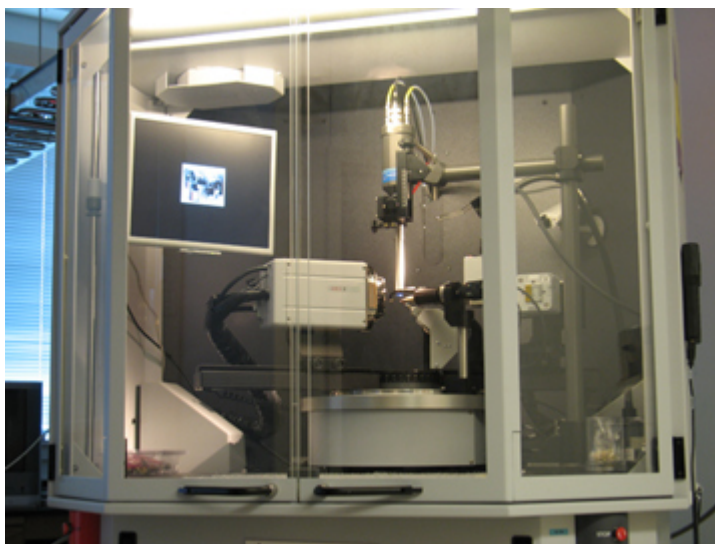


Figure 2.6 Apex CCD in the Department of Chemistry at University of Waterloo.

Structure solution and refinements were performed with the SHELXTL package. The program tries to find the best fitting between the calculated structure factors (F_c) and the observed ones (F_o). Two residual factors, R1 and wR2, are evaluated in order for checking the refinement results:

$$R1 = \frac{\sum_{hkl} || F_o | - | F_c ||}{\sum_{hkl} | F_o |} \quad (2-3)$$

$$wR2 = \sqrt{\frac{\sum_{hkl} w(F_o^2 - F_c^2)^2}{\sum_{hkl} w(F_o^2)^2}} \quad (2-4)$$

Generally, for a crystal structure without special problems, the refined structure should give an R1 value less than 0.05 and wR2 less than 0.10. Nowadays, single crystal structure

determination has become an important and extremely powerful tool not only for solid state chemists but also for other chemists interested in the structures of their compounds.

2.2.3 Energy dispersive X-ray (EDX) analysis

Energy dispersive X-ray (EDX) analysis provides the characterization of elements and their stoichiometry in the materials. This technique is applied in conjunction with Scanning Electron Microscopy (SEM). When an electron beam hits the surface of the sample, X-rays will be emitted from that material. The energy of the beam used is usually in the range of 10-25 kV [14] and the energy of the X-rays emitted depends on the material under the investigation. One example of an EDX spectrum is shown in Figure 2.7.

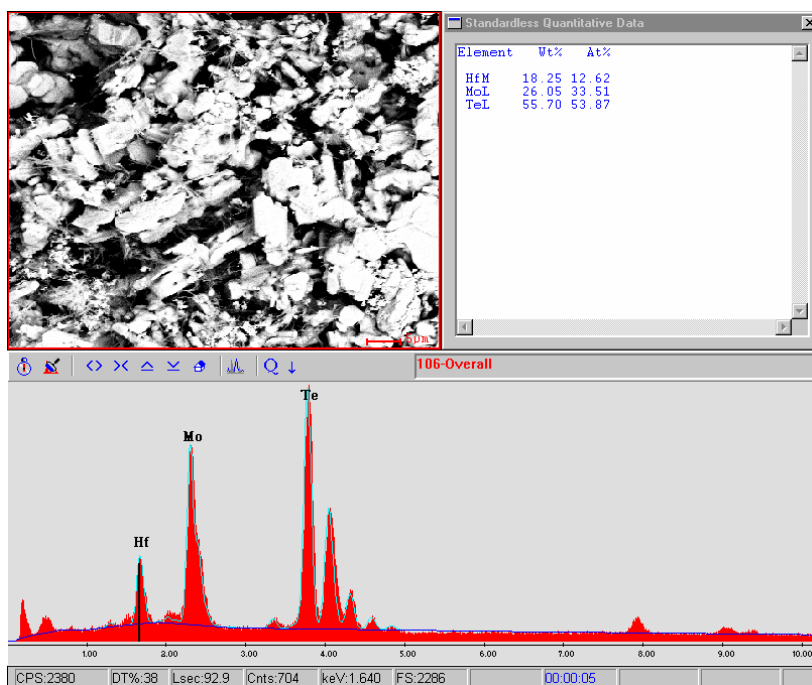


Figure 2.7 EDX spectrum and summary of the results.

Different elements will have different chemical shifts in the spectrum, which can be used as “Fingerprints”. The sum of the areas under the peaks of each element is proportional to quantity of elements

EDX analysis in the following chapters was performed by a SEM (LEO 1530) integrated with EDX Pegasus 1200 in the Department of Chemistry at University of Waterloo.

2.2.4 Thermal analysis

Thermal analysis is the study of thermal stability and possible phase changes in relation to the temperatures. Thermal analysis in this thesis is performed on the computer-controlled NETZSCH STA 409PC Luxx, which combines Differential Scanning Calorimetry (DSC) and Thermogravimetry (TG) measurements. The measurements were carried out under a constant flow of the argon.

DSC is a thermoanalytical technique in which the difference of the heat required to increase the temperature of a sample and reference is measured as a function of temperature [15]. Both the sample and reference are maintained at ideally the same temperature throughout the experiment. The basic theory behind the technique is that, when the sample undergoes a phase transition, different amounts of heat will be needed to reach the target temperature. When the sample is going to melt, more heat will be needed for increasing the temperature resulting in an endothermic process; likewise, crystallization will undergo an exothermic processes as shown in Figure 2.8.

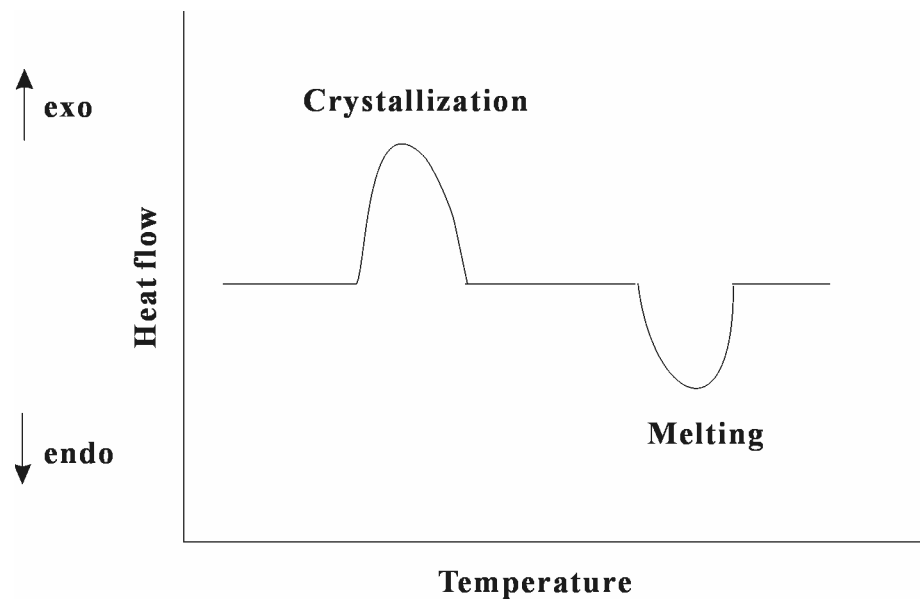


Figure 2.8 Schematic DSC curve.

TG analysis, on the other hand, is performed on samples to examine changes in weight in relation to the phase changes in dependence of the temperature.

2.3 Physical property measurements

In order to investigate the thermoelectric performances of the materials, Seebeck coefficient, electrical conductivity and thermal conductivity will be measured. Detailed information about the methods and equipment utilized in our laboratories for these measurements is introduced here.

2.3.1 Seebeck coefficient measurement

In our laboratory the MMR SB-100 Seebeck System [16] shown in Figure 2.9 is used for the Seebeck coefficient measurements over a temperature range from 300 K to 600K.



Figure 2.9 Seebeck Measurement System in our laboratory.

The Seebeck thermal stage includes two pairs of connections as shown in Figure 2.10. One pair consists of a junction of silver and a reference material with a known Seebeck coefficient. We use copper-nickel wire (constantan, Cu : Ni = 55 : 45 wt%) as the reference,

which has a Seebeck value of around $-40\mu\text{VK}^{-1}$ at room temperature. The other one consists of a junction of silver and the material whose Seebeck coefficient is to be determined.

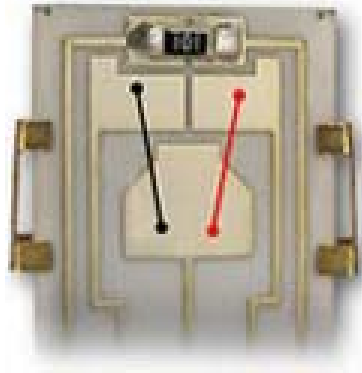


Figure 2.10 Sample stage for the Seebeck measurement with the sample (black) and reference (red).

The temperature on the sample stage is operated by a computer via the heater K-20. The temperature difference generated by the K-20 is related to the input power (P). When the power is applied to the heater, the potential difference can be obtained for both of the sample (V_1) and reference (V_2). The Seebeck coefficient of the sample (S_1) will be calculated by the known Seebeck coefficient of the reference (S_2) via equations below.

$$V_1 = S_1 \times \Delta T(P) \quad (2-5)$$

$$V_2 = S_2 \times \Delta T(P) \quad (2-6)$$

$$S_1 = S_2 \times \frac{V_1}{V_2} \quad (2-7)$$

2.3.2 Electrical conductivity measurement

In order to get accurate electrical conductivity, the four-point probe method was utilized for all the measurements as shown in Figure 2.11.

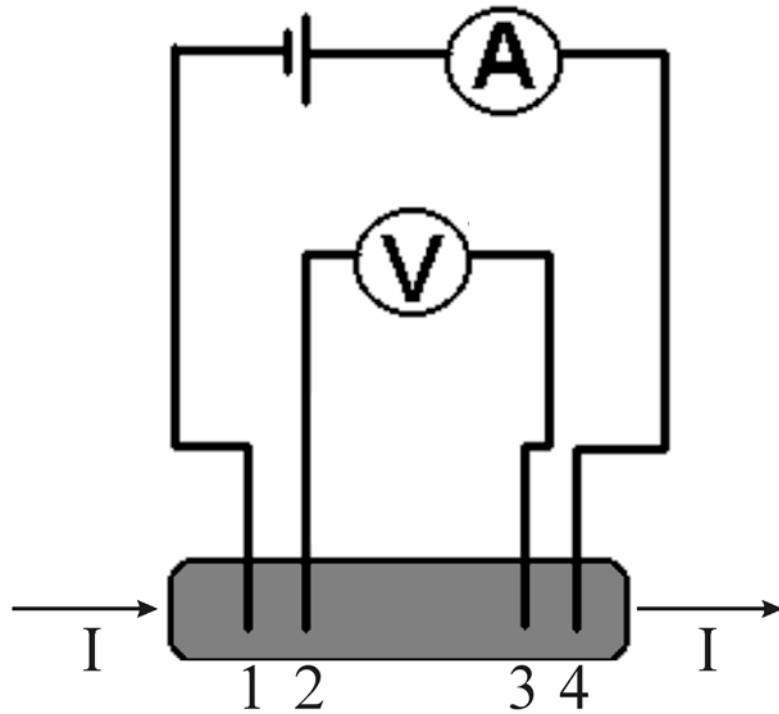


Figure 2.11 Four-point probe method [17].

The main source of error for the two-point method in the conductivity measurement is from the contact resistance, R_c . The voltage will be measured as:

$$V_{\text{total}} = R_{\text{total}} \times I = (R_c + R_{\text{sample}}) \times I \quad (2-8)$$

For the four-point method (Figure 2.11), the potential difference (V_{23}) is measured instead of V_{total} . Since the voltage meter and the sample between points 2 and 3 are in a parallel circuit,

V_{23} is the accurate value of potential differences of the sample between points 2 and 3 independent of the contact resistance.

Because the sample and contacts are in a series circuit, the current will be the same anywhere in the sample. Therefore, the resistance of the sample between points 2 and 3 can be extracted:

$$R_{23} = \frac{V_{23}}{I} \quad (2-9)$$

The conductivity will then be calculated by the equation 1-6 introduced Chapter 1.

2.3.3 Thermal conductivity measurement

The thermal conductivity (κ) is found from the equation [18]:

$$\kappa = \alpha \times \rho \times C_p \quad (2-10)$$

where ρ being the density, α representing thermal diffusivity, C_p standing for specific heat capacity. α can be extracted from its relationship with the sample thickness (L) and the time required to reach half of the maximum temperature increase ($t_{0.5}$) [19]:

$$\alpha = 0.1388 \times \frac{L^2}{t_{0.5}} \quad (2-11)$$

The specific heat capacity (C_p) is the amount of heat per unit mass required to raise the temperature by one degree Celsius. In our laboratory, this value of the sample can be obtained by comparing the heat absorptions with the reference sample, which has the known C_p value. If we know the density (ρ) of the sample, the thermal conductivity (κ) can be easily calculated based on the equation above.

2.4 Electronic structure calculations

During the past decade, electronic structure calculations have played a more and more important role in the fields of physics and chemistry, especially with the development of advanced computers at the present day. For the thermoelectric research, electronic structure calculations not only can predict the transport properties of materials, but they also help scientists to have a good understanding of properties. A brief summary of calculation methods and software packages utilizing different theory levels is presented below.

2.4.1 LMTO

These calculations are quantum-mechanical methods, e.g., calculating the energy by solving the quantum mechanical equations for electrons in the atom. Unfortunately, the equations are too complicated to be solved exactly due to numerous electrons contained in a crystal with large amount of degrees of freedom and interactions. However, a periodic arrangement of atoms in the crystal makes it possible to solve equivalent equations in a small periodic unit cell instead of doing so for the whole infinite system.

The LMTO (LMTO = linear muffin tin orbitals) program [20] is employed for the electronic structure investigations in this thesis. This method is based on density functional theory (DFT) [21,22], which states that the total energy is a unique functional of the electron density and has its minimum at the ground state density. The model lets us solve the simplified Kohn-Sham equations [23] instead of solving the Schrödinger equation. The LMTO program package we are using is controlled under a LINUX computer operating system. The LMTO method uses the atomic spheres approximation (ASA) [24], and the local density approximation (LDA) [25] for exchange correlation energy in the DFT.

2.4.2 Gaussian03

Gaussian03 [26] is quite useful software for molecular chemists to extract calculation results of their compounds, including the single point energy, electron density, dipole moment, geometry optimization, and frequencies. For solid state chemists, the molecular orbitals around the Fermi level [27] and the energy differences between these orbitals are especially interesting. Such information can be achieved by the single point energy calculation from Gaussian03.

Various suitable basis sets and calculation methods are required for different calculations. A basis set is the mathematical description of the orbitals within a system used to perform the theoretical calculations. Larger basis sets more accurately approximate the orbitals by imposing fewer restrictions on the locations of the electrons in space, hence are more time consuming. In order to get accurate calculation results within a reasonable time, another factor to be considered is the appropriate level of the theoretical method. In this work, molecular orbital diagrams for the frontier orbitals were computed via the B3LYP method [28,29] based on DFT, with the 3-21G basis set [30].

References

- [1] Knuth, E. L. *Phys. of Fluids* **1959**, 2, 339-340.
- [2] West, A. R. *Basic solid state chemistry*; 2nd ed.; John Wiley & Sons Ltd.: Chichester, UK, 1999.
- [3] Greenwood, N. N. *Chemistry of the Elements*; 2nd ed.; Oxford: Butterworth, UK, 1997.
- [4] John, B. *Foseco Ferrous Foundryman's Handbook*; 11th ed.; Elsevier Butterworth-Heinemann: Oxford, UK, 2000.
- [5] Ewald, P. P. *Fifty years of X-ray diffraction*; International Union of Crystallography: Utrecht, 1962.
- [6] Bragg, W. H. *Nature* **1913**, 90, 219.
- [7] www.farmfak.uu.se
- [8] Bragg, W. H. *Nature* **1913**, 91, 477.
- [9] Massa, W. *Crystal structure Determination*; 2nd ed.; Springer: Berlin, Germany, 2004.
- [10] *SMART*; Version 4 ed.; Siemens Analytical X-ray Instruments Inc.: Madison.
- [11] Kittel, C. *Introduction to Solid State Physics*; 7th ed.; John Wiley & Sons Inc.: New York, 1996.
- [12] *SAINT*; Version 4 ed.; Siemens Analytical X-ray Instruments Inc.: Madison, WI, 1995.
- [13] Sheldrick, G. M. *SHELXTL*; Version 5.12 ed.; Siemens Analytical X-Ray Systems: Madison, WI, 1995.
- [14] <http://www.uksaf.org/tech/edx.html>
- [15] Pungor, E. A. *A Practical Guide to Instrumental Analysis*; CRC Press: Boca Raton, Florida, 1995.
- [16] <http://www.mmr.com/seebeck.html>
- [17] www.imagesco.com
- [18] Parker, W. J.; Jenkins, R. J.; Butler, C. P.; Abbott, G. L. *J. Appl. Phys.* **1961**, 32, 1679-1684.
- [19] Rowe, D. M. *CRC Handbook of Thermoelectrics*; CRC Press: Boca Raton, FL, 1995.
- [20] Skriver, H. L. *The LMTO Method*; Springer: Berlin, Germany, 1984.
- [21] Parr, R. G.; Yang, W. *Density-functional theory of atoms and molecules*; Oxford Univ. Press: Oxford, 1989.
- [22] Hohenberg, P.; Kohn, W. *Phys. Rev.* **1964**, 136, B864-B871.
- [23] Kohn, W.; Sham, L. J. *Phys. Rev.* **1965**, 140, A1133-A1138.
- [24] Andersen, O. K. *Phys. Rev. B* **1975**, 12, 3060-3083.
- [25] Hedin, L.; Lundqvist, B. I. *J. Phys. C* **1971**, 4, 2064-2083.
- [26] M. J. Frisch; G. W. Trucks; Schlegel, H. B.; Scuseria, G. E.; Robb, M. A.; Cheeseman, J. R.; Montgomery, J. A.; Vreven, T.; Kudin, K. N.; Burant, J. C.; Millam, J. M.; Iyenga, S. S.; Tomasi, J.; Barone, V.; Mennucci, B.; Cossi, M.; Scalmani, G.; Rega, N.; Petersson, G. A.; Nakatsuji, H.; Hada, M.; Ehara, M.; Toyota, K.; Fukuda, R.; Hasegawa, J.; Ishida, M.; Nakajima, T.; Honda, Y.; Kitao, O.; Nakai, H.; Klene, M.; Li, X.; Knox, J. E.; Hratchian, H. P.; Cross, J. B.; Adamo, C.; Jaramillo, J.; Gomperts, R.; Stratmann, R. E.; Yazyev, O.; Austin, A. J.; Cammi, R.;

- Pomelli, C.; Ochterski, J. W.; Ayala, P. Y.; Morokuma, K.; Voth, G. A.; Salvador, P.; Dannenberg, J. J.; Zakrzewski, V. G.; Dapprich, S.; Daniels, A. D.; Strain, M. C.; Farkas, O.; Malick, D. K.; Rabuck, A. D.; Raghavachari, K.; Foresman, J. B.; Ortiz, J. V.; Cui, Q.; Baboul, A. G.; Clifford, S.; Cioslowski, J.; Stefanov, B. B.; Liu, G.; Liashenko, A.; Piskorz, P.; Komaromi, I.; Martin, R. L.; Fox, D. J.; Keith, T.; Al-Laham, M. A.; Peng, C. Y.; Nanayakkara, A.; Challacombe, M.; Gill, P. M. W.; Johnson, B.; Chen, W.; Wong, M. W.; Gonzalez, C.; Pople, J. A. *Gaussian 03, Revision C.02*; Gaussian, Inc.: Wallingford, CT, USA, 2004.
- [27] Hoffmann, R. *Solids and Surfaces: A Chemist's View on Bonding in Extended Structures*; VCH Publishers, Inc.: New York, 1988.
- [28] Miehlich, B.; Savin, A.; Stoll, H.; Preuss, H. *Chem. Phys. Lett.* **1989**, *157*, 200-206.
- [29] Lee, C.; Yang, W.; Parr, R. G. *Phys. Rev.* **1988**, *37*, 785-789.
- [30] Pietro, W. J.; Francl, M. M.; Hehre, W. J.; DeFrees, D. J.; Pople, J. A.; Binkley, J. S. *J. Am. Chem. Soc.* **1982**, *104*, 5039-5048.

3. New oxides

Oxides had not originally been considered as suitable for thermoelectric applications because of their poor mobility. However, in 1997 Dr. Terasaki et al. [1] found that a single crystal of the layered cobalt oxide NaCo_2O_4 exhibits excellent thermoelectric performances, with $ZT \approx 0.8$ at 1000K. Because of relatively low cost, non-toxic and high thermal stability in the air, oxides have been strongly considered to be potential candidates for future commercial applications. This is one of the key reasons for the oxides system to be investigated by many research groups. After that, the layered cobalt oxides were of great interest, and several new candidate materials, including $\text{Ca}_3\text{Co}_4\text{O}_9$ [2,3], and $[\text{Bi}_{0.87}\text{SrO}_2]_2[\text{CoO}_2]_{1.82}$ [4], were developed through extensive studies. These compounds all consist of stacks of edge-sharing CoO_6 and rock-salt type blocking layers along the c -axis, e.g., the misfit-layer structure, as shown in Figure 3.1.

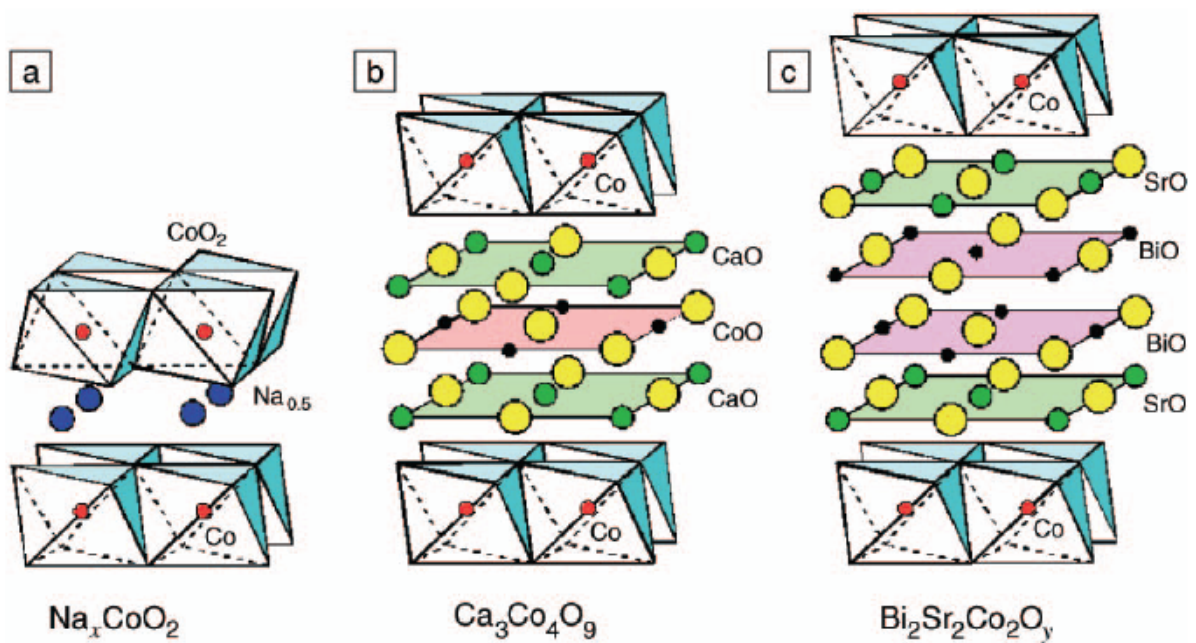


Figure 3.1 CoO₂-based TE oxides: (a) Na_xCoO_2 , (b) $\text{Ca}_3\text{Co}_4\text{O}_9$, (c) $\text{Bi}_2\text{Sr}_2\text{Co}_2\text{O}_y$ [5].

Within the structure of the Co oxides, CoO_6 layers work as the path way for the electric current which leads to a high electrical conductivity and thermopower; on the other hand, the rock-salt layer as the path way for the thermal flow results in the low thermal conductivity [6,7] as shown in Figure 3.2.

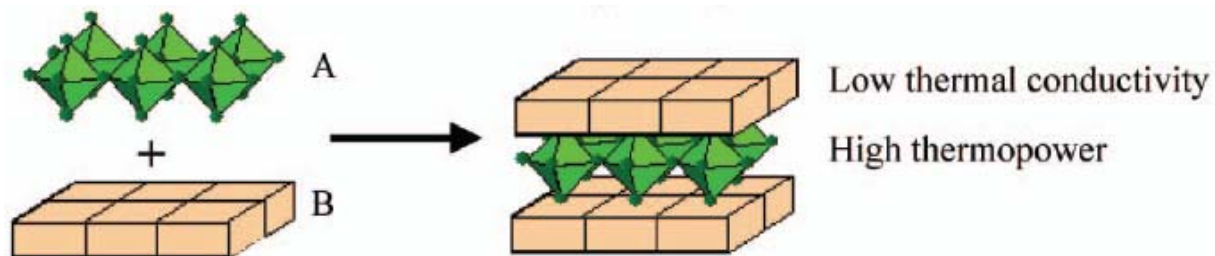


Figure 3.2 Schematic illustration of contributions from different layers of cobalt oxides for good thermoelectric properties [5].

During my Ph.D. studies, I have been looking for oxides with new structure types as well as investigating the thermoelectric properties of known oxides. In the following part of this chapter, the structure and physical properties of three oxides: $\text{Na}_2\text{Cu}_2\text{TeO}_6$ [8], $\text{LaMo}_8\text{O}_{14}$ and $\text{Pb}_{0.69}\text{Mo}_4\text{O}_6$ [9] will be fully discussed.

3.1 Synthesis, structure and magnetic Properties of the new layered Cu^{II} oxide Na₂Cu₂TeO₆

3.1.1 Introduction

Since oxides like NaCo₂O₄ [1] with misfit layers showed excellent thermoelectric properties, one of my targets of the project is to discover new oxides with the similar structure but different composites. In order to build up a layered structure like in NaCo₂O₄, the elements Cu and Te are chosen to replace Co because first, CuO₂ layers could bring interesting electrical properties e.g., high-T_C superconductors like YBa₂Cu₃O₇ [10,11] and related materials; second, Te as a heavy element will be beneficial for low thermal conductivity. We succeeded in synthesizing a new layered transition-metal oxide, Na₂Cu₂TeO₆ [8]. With this contribution we present its crystal structure, electronic structure, as well as transport and interesting magnetic properties.

3.1.2 Synthesis and phase analysis

Phase pure Na₂Cu₂TeO₆ was prepared starting from 1 mmol Na₂CO₃, 2 mmol CuO and 1 mmol TeO₂ under air, i.e. oxidizing conditions, according to the reaction equation (3-1).



The starting materials were thoroughly ground and subsequently calcined at 923 K in a muffle furnace in air for three days. Thereafter, the furnace was cooled down to room temperature at a rate of 10 K per hour. Na₂Cu₂TeO₆ was formed as a green microcrystalline

powder. For the single crystal structure study, single crystals of green $\text{Na}_2\text{Cu}_2\text{TeO}_6$ were synthesized by heating the single-phase sample at 860 K for 12 hours, followed by slow cooling to room temperature.

A block shaped single crystal of $\text{Na}_2\text{Cu}_2\text{TeO}_6$ was selected for the Single Crystal Structure Determination. The lattice parameters were indicative of monoclinic symmetry, and the systematic absences restricted the possible space groups to $C2$, $C2/m$, and Cm . The subsequent solution and refinement in $C2/m$ were successful, and refining the model in $C2$ and Cm led to no improvements in the residual factors, but instead resulted in high correlation factors. Crystallographic data, atomic coordinates and thermal parameters, as well as selected bond distances for $\text{Na}_2\text{Cu}_2\text{TeO}_6$ are given in Table A.2 – 4 in the Appendix.

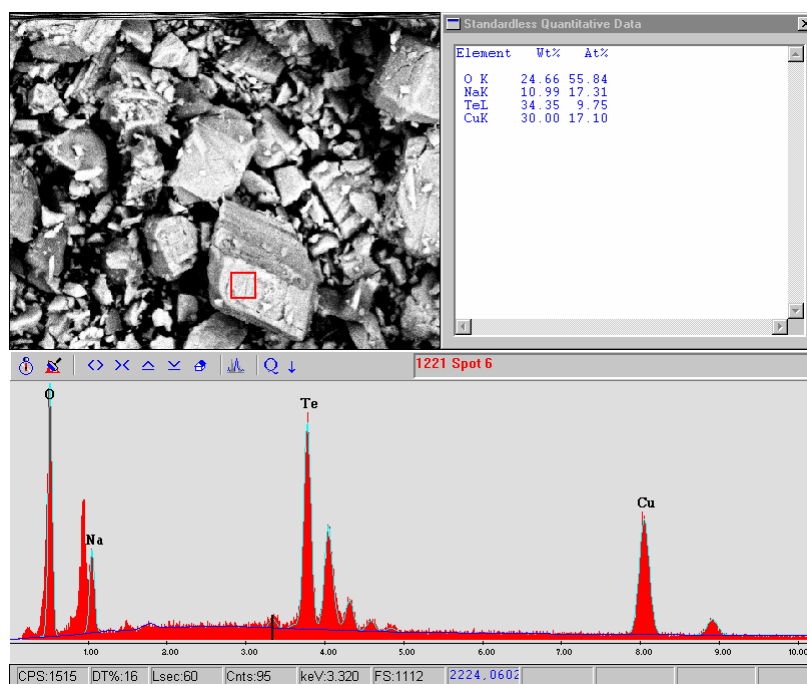


Figure 3.3 Scanning Electron Microscope picture of $\text{Na}_2\text{Cu}_2\text{TeO}_6$ crystals and EDAX analysis.

The sample was then examined by the powder X-ray diffraction at room temperature and Energy Dispersive X-ray (EDX) analysis (Figure 3.3). No known compounds were detected in the X-ray powder pattern. The composition averaged over selected crystals using EDAX was Na : Cu : Te : O = 17(1) : 17(1) : 10(1) : 56 (in at-%). This is in quantitative agreement with the at-% values resulting from the single crystal structure determination of 18.2 : 18.2 : 9.1 : 54.5.

In order to study the stability of this new oxide, Differential scanning calorimetry (DSC) measurements were also performed to investigate the crystallization behavior of the compound. Samples (3-5mg) held in aluminum pans were heated from room temperature to 1000 °C at a rate of 10 °C/min under a flow of argon. The results suggested that $\text{Na}_2\text{Cu}_2\text{TeO}_6$ started to decompose at 870 °C and the total weight loss was around 4%, as shown in Figure 3.4. The color of the compound changed from green to brown after the measurement, which was also the evidence of the phase change.

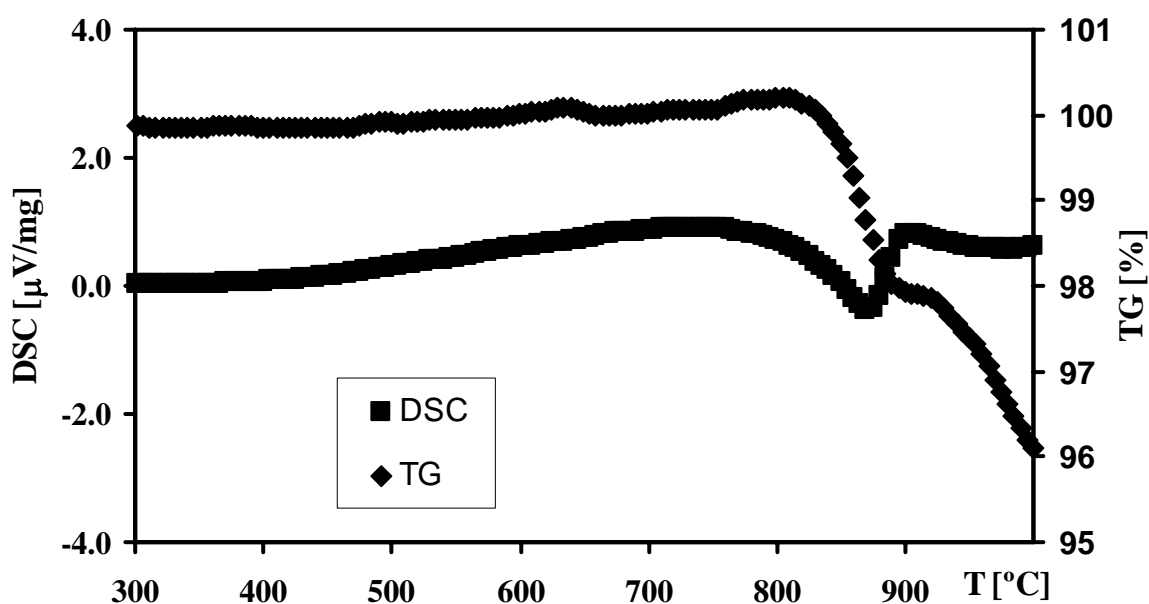


Figure 3.4 Thermal analysis for $\text{Na}_2\text{Cu}_2\text{TeO}_6$.

3.1.3 Crystal structure

$\text{Na}_2\text{Cu}_2\text{TeO}_6$ is a new quaternary layered transition-metal oxide crystallizing in a new structure type. The assignment of formal charges is straightforward, yielding fully oxidized cations Na^+ and Te^{6+} , and therefore Cu^{2+} . This type is a (filled) distorted substitution variant of the CdI_2 type, with the O anions forming layers reminiscent of hexagonal closest packing. The Cd atoms are substituted by the Cu and Te cations, and the Na cations fill pseudo-octahedral voids between the $\text{}^2_\infty[\text{Cu}_2\text{TeO}_6]$ layers (Figure 3.5).

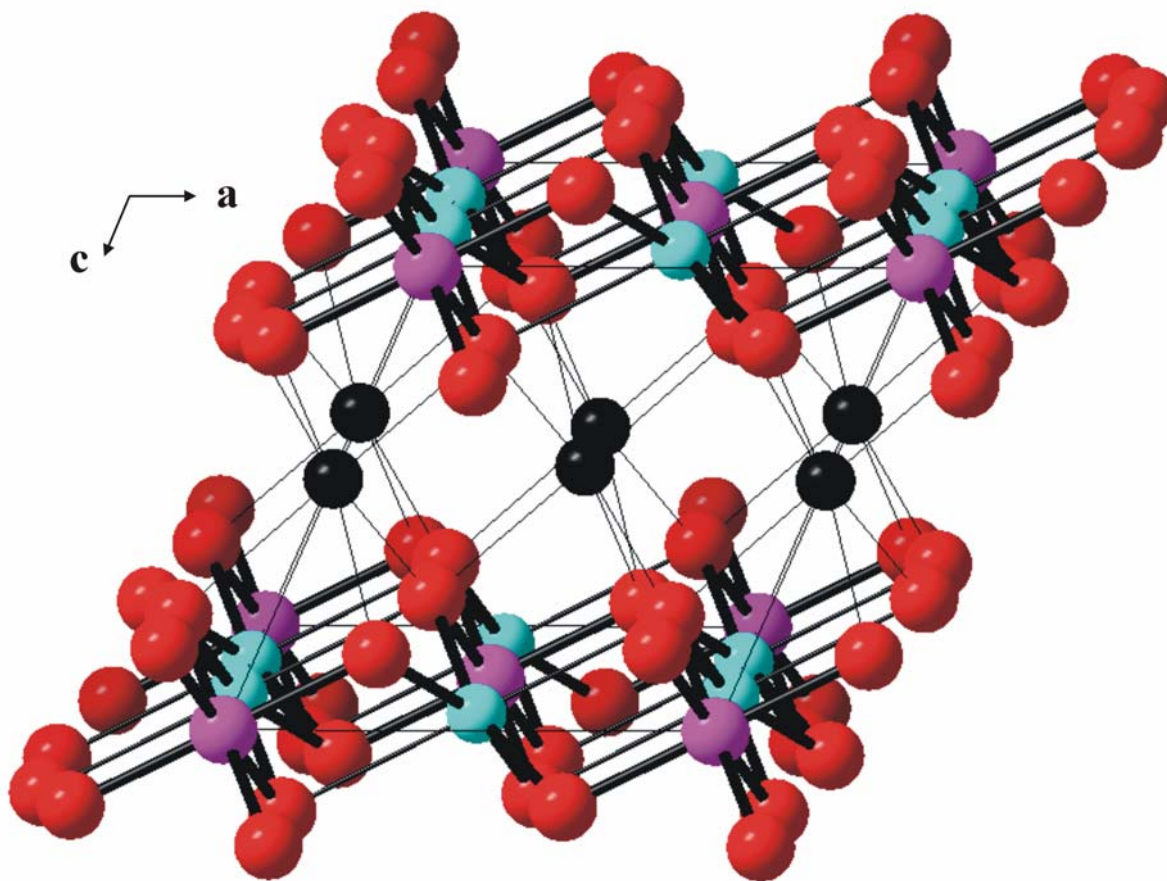


Figure 3.5 Crystal structure of $\text{Na}_2\text{Cu}_2\text{TeO}_6$. Na: black; Cu: blue; Te: purple; O: red.

The NaO_6 octahedra exhibit an AlCl_3 -like arrangement with Na-O bonds between 2.31 Å and 2.49 Å. A ${}^2_\infty[\text{Cu}_2\text{TeO}_6]$ layer is depicted in Figure 3.6, revealing the substitution pattern of two Cu cations and one Te cation for the Cd atoms of CdI_2 .

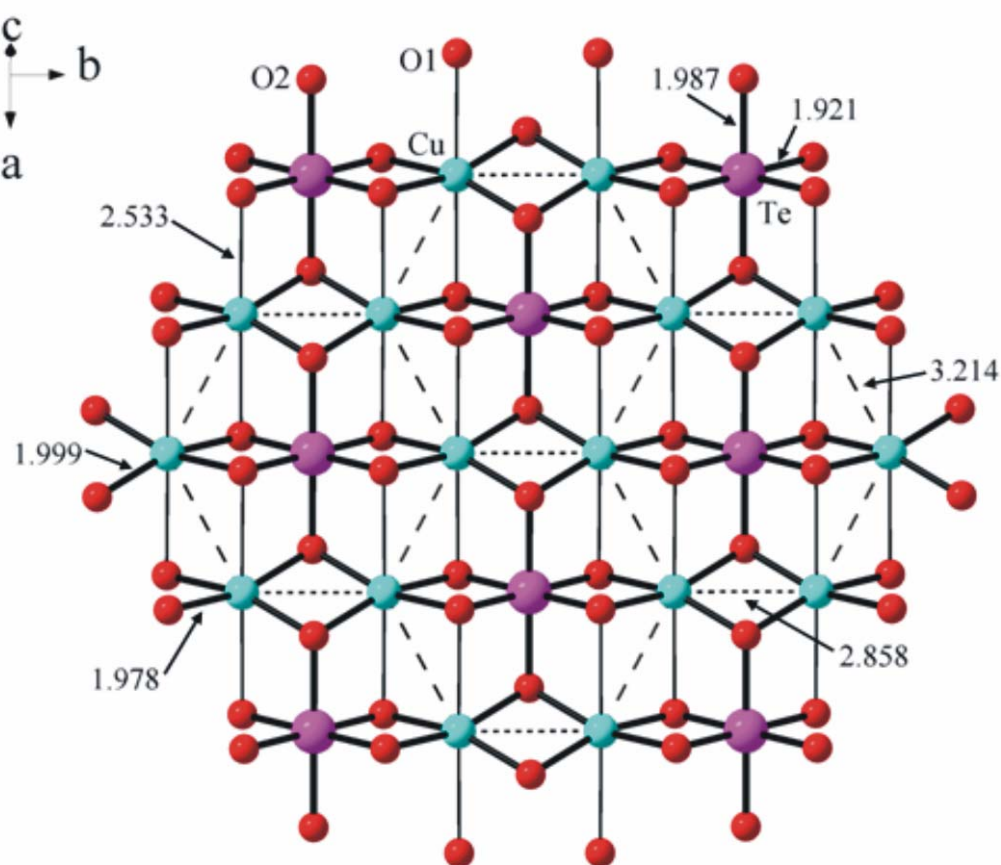


Figure 3.6 ${}^2_\infty[\text{Cu}_2\text{TeO}_6]$ layer of $\text{Na}_2\text{Cu}_2\text{TeO}_6$.

The TeO_6 polyhedron is an almost regular octahedron, with six Te-O bonds between 1.92 Å and 1.99 Å. Such bond lengths are expected for Te^{VI} oxides, as also found in Na_2TeO_4 (Te-O bonds between 1.85 Å and 2.04 Å) [12] and CuTeO_4 (1.87 Å - 2.02 Å) [13]. On the other hand, significant deviations from the octahedral coordination of the Cu cation are obvious, as it forms four short (2.00 Å) and two longer (2.53 Å) Cu-O interactions. Deviations like this,

towards an elongated octahedron, are typical for Cu^{II} oxides; e.g., tenorite, CuO , comprises four bonds in the range of 1.94 Å to 1.97 Å, and two longer contacts of 2.82 Å [14]. Other examples include the superconducting cuprates. The CuO_6 polyhedra are linked to three CuO_6 and three TeO_6 neighbors via edge-sharing. This results in one Cu–Cu contact per Cu^{II} of 2.86 Å and two of 3.21 Å (dashed lines in Figure 3.6), yielding a distorted honeycomb lattice of Cu atoms.

3.1.4 Electronic structure calculation

We employed the LMTO program package for the electronic structure calculations Figure 3.7. The filled valence orbitals are O-2s (occurring below the energy window shown), O-2p, and Cu-3d orbitals. Per Cu^{II} atom, there are four filled 3d bands and one half-filled 3d band. This amounts to two half-filled bands, as there are two Cu atoms in the first Brillouin zone. The Cu-3d electrons are localized, i.e. this oxide is a Mott insulator.

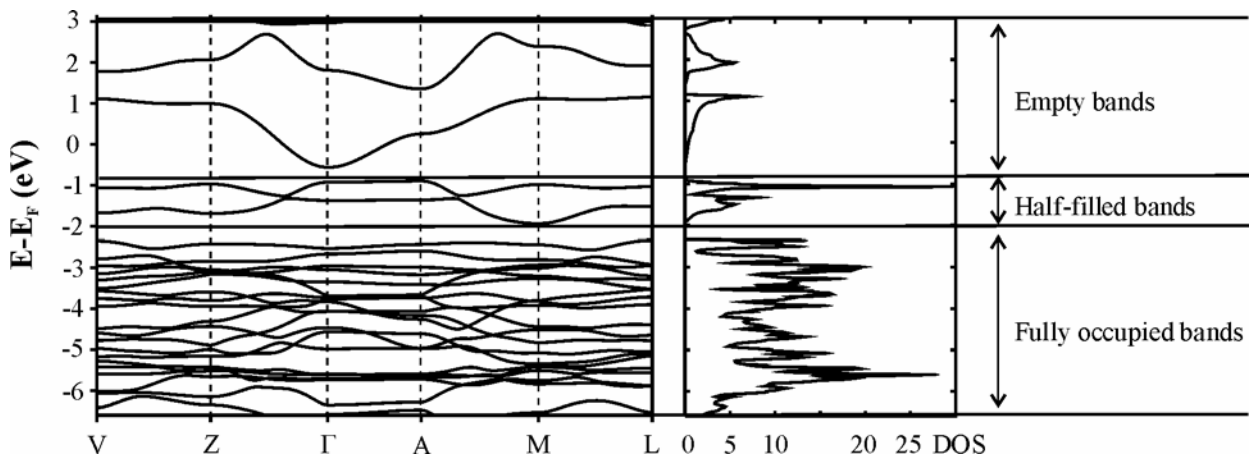


Figure 3.7 Band structure and densities of states of $\text{Na}_2\text{Cu}_2\text{TeO}_6$.

Cu is in the +2 oxidation state and Te in +6. There is a band gap between the Te 4s bands and Cu 3d bands.

3.1.5 Physical Properties

We cold-pressed part of the ground phase-pure sample into a bar-shaped pellet of the dimensions $6 \times 1 \times 1 \text{ mm}^3$ for physical transport measurements, since no single crystals of sufficient dimensions were available. The high internal resistance of the pellet prevented Seebeck and electrical resistance measurements. Based on our experience with other high resistance materials we conclude that its specific resistance must be above $1 \text{ M}\Omega\text{cm}$ at room temperature.

In conclusion, a new quaternary layered transition-metal oxide, $\text{Na}_2\text{Cu}_2\text{TeO}_6$, has been synthesized under air using stoichiometric (with respect to the cationic elements) mixtures of Na_2CO_3 , CuO and TeO_2 . The structure is composed of $\frac{2}{\infty}[\text{Cu}_2\text{TeO}_6]$ layers with the Na atoms located in the octahedral voids between the layers. $\text{Na}_2\text{Cu}_2\text{TeO}_6$ is a green nonmetallic compound with the extreme high resistivity, which is not suitable for thermoelectric applications.

3.2 Ternary oxides with Mo clusters: $\text{LaMo}_8\text{O}_{14}$ and $\text{Pb}_{0.69}\text{Mo}_4\text{O}_6$

3.2.1 Introduction

In the previous sections of this chapter, we have discussed layered oxides for the thermoelectric applications. There might be other potential oxide systems showing outstanding thermoelectric performances, which is one of the big reasons for many research groups to re-investigate known oxides with interesting features. Based on a thorough literature searching, it turned out that oxides with different molybdenum clusters could be one of the promising alternative oxide systems for thermoelectric applications.

Those molybdenum oxides, such as LaMo_5O_8 [15,16], $\text{Y}_4\text{Mo}_4\text{O}_{11}$ [17], $\text{Pr}_4\text{Mo}_9\text{O}_{18}$ [18], and $\text{La}_5\text{Mo}_{32}\text{O}_{54}$ [19], containing different Mo clusters with strong metal-metal bonds between Mo atoms, are usually semiconductors with narrow band gaps which would be ideal for the thermoelectric applications. Within the structures of those compounds, LaMo_5O_8 contains infinite zigzag chains of Mo_{10} clusters, and $\text{Y}_4\text{Mo}_4\text{O}_{11}$ consists of infinite trans-edge sharing Mo octahedra. As for $\text{Pr}_4\text{Mo}_9\text{O}_{18}$, there are several different isolated Mo clusters in the structure, Mo_3 , Mo_7 and Mo_{19} in $\text{Pr}_4\text{Mo}_9\text{O}_{18}$; while $\text{La}_5\text{Mo}_{32}\text{O}_{54}$ contains $\text{Mo}_7+\text{Mo}_{10}+\text{Mo}_7$ motifs in $\text{La}_5\text{Mo}_{32}\text{O}_{54}$, as shown in Figure 3.8.

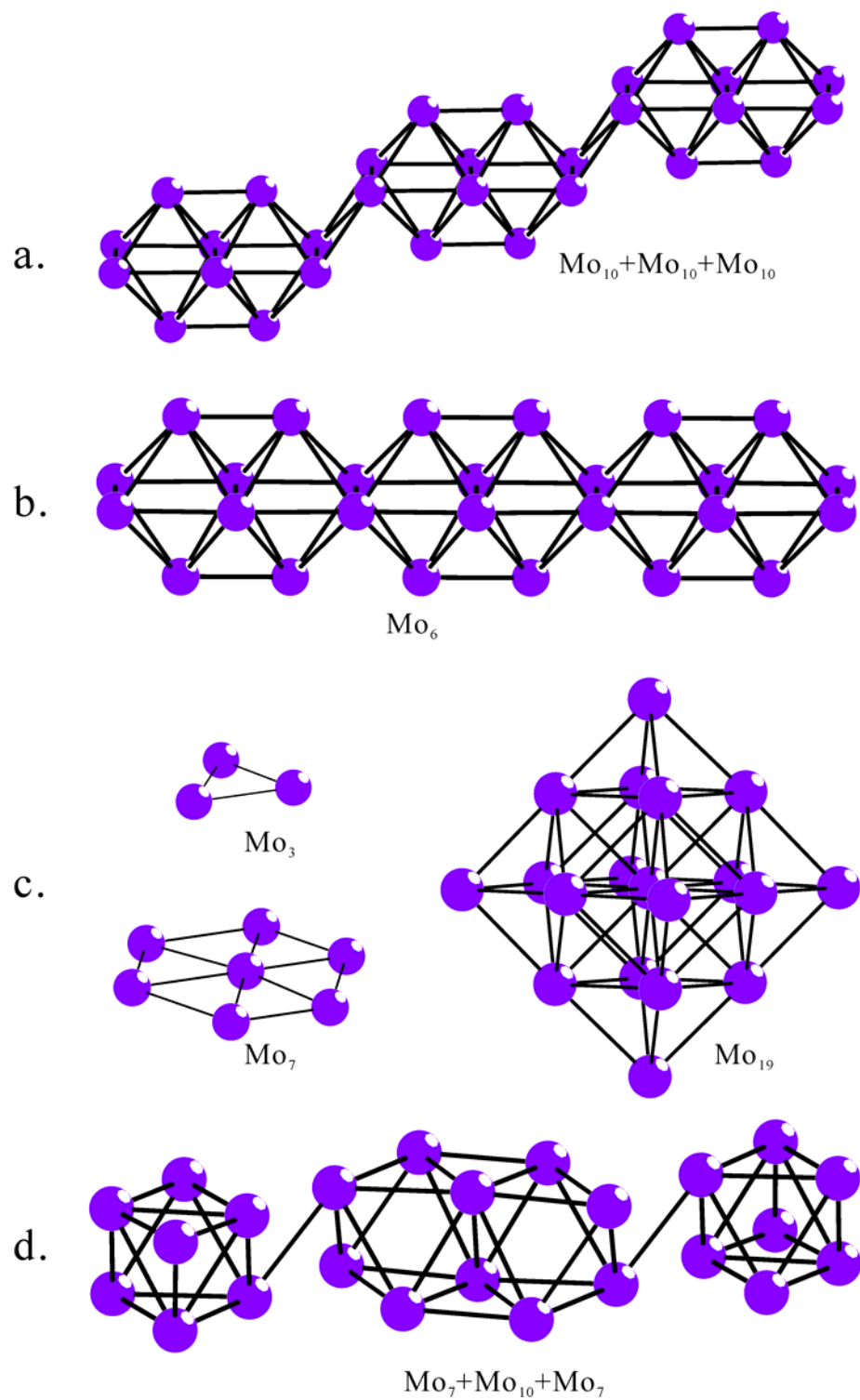


Figure 3.8 Mo clusters in a. LaMo_5O_8 , b. $\text{Y}_4\text{Mo}_4\text{O}_{11}$, c. $\text{Pr}_4\text{Mo}_9\text{O}_{18}$, d. $\text{La}_5\text{Mo}_{32}\text{O}_{54}$.

The electronic structure calculation of $Y_4Mo_4O_{11}$, shown as an example in Figure 3.9, suggests the band gap is around 0.1 eV. The flat bands around the Fermi level suggest a high Seebeck coefficient for this compound as well.

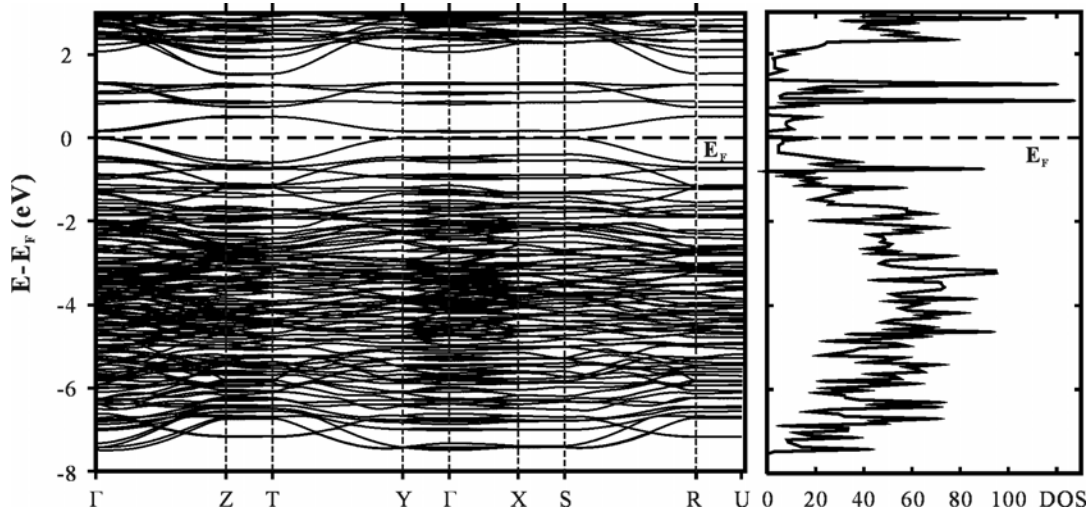


Figure 3.9 Band structure and densities of states of $Y_4Mo_4O_{11}$.

I was able to synthesize a phase pure sample of $LaMo_8O_{14}$ [20] containing isolated Mo_8 clusters and $Pb_{0.69}Mo_4O_6$ consisting of infinite chains of trans-edge-sharing octahedra. In the following concepts, their crystal structure, electronic structure, as well as transport properties of these two compounds will be presented.

3.2.2 Synthesis and phase analysis

$LaMo_8O_{14}$: Phase pure $LaMo_8O_{14}$ was prepared from stoichiometric mixtures of La_2O_3 , Mo and MoO_2 . The mixtures were thoroughly ground before pressing into a pellet of 6mm diameter. The pellet was then loaded into a Mo crucible, followed by putting into an induction furnace under a high vacuum. The furnace was ramped up to 1600 K in one hour,

and the sample was heated at this temperature for another two hours. Then the furnace was quickly ramped down to room temperature. The final products turned out to be black powder and were examined by powder X-ray diffraction at room temperature and no side products were detected in the X-ray powder pattern.

Pb_{0.69}Mo₄O₆: The compound, “Pb_{0.75}Mo₄O₆”, was firstly tried to be prepared from mixtures of PbO, Mo and MoO₃. The mixtures were treated as the same as starting materials for LaMo₈O₁₄ synthesis. The pellet was loaded into a Tamman crucible followed by sealing in an evacuated silica tube. The sample was heated at a rate of 2 K/min to 1473 K and this temperature was kept for two days. The furnace was switched off after cooling down to 773 K at a rate of 2 K/min. The final products were found to be black and microcrystalline with needle shaped crystals. A small black needle crystal was selected for the single crystal structure determination (details will be described later), which reveal that the Pb/Mo ratio is actually 0.69/4. The powder samples were characterized by X-ray diffraction and confirmed to be pure.

In order to check the phase width, other five reactions were done with different Pb/Mo ratios, (0.5, 0.6, 0.8, 0.9, and 0.1) : 4. The final products were characterized by X-ray diffraction. All of the products contain the significant side product, MoO₂, which suggests a rather small phase range for this lead molybdenum oxide.

A black needle crystal (100 × 20 × 20 μm³) was selected for data collection using the SMART Apex CCD (BRUKER). However, we were not able to deal with the unconventional incommensurate supercell reflections obtained. A full sphere data collection was carried out on another needle crystal via Excalibur3 diffractometer, with Mo Kα radiation at Stockholm University in Sweden. From the intensity distribution the data is seen to contain a set of

strong reflections and a set of weaker reflections. Furthermore the two sets show unusual extinction conditions and no 3D space group exists that will take into account all the observed extinction conditions. Therefore it was chosen to solve the structure using a modulation approach. Therein the strong reflections give the basic cell and the remaining reflections are indexed using a modulation vector (0, 0, 0.25). The basic cell is equivalent to the NaMo₄O₆ cell [21]. This results in the (3+1)D super space group *P4/mbm(00g)00ss*.

First, the basic structure was solved from the main reflections using SHELXTL packages [22] with the WINGX interface [23]. This indicates the position of the Pb to be strongly disordered around the high symmetry position (0, 0, 0). To change into the super space description the structure was transferred to Jana2000 [24] and the Pb orbit was given the ideal (0, 0, 0) position. The parameters were refined and finally the Pb atoms were allowed harmonic thermal parameters. The final model contains two O positions, two Mo positions and one Pb position. Crystallographic details are listed in Table A. 5-7 in the Appendix.

3.2.3 Crystal structures of two molybdenum oxides

LaMo₈O₁₄ crystallizes in orthorhombic crystal system with the space group *Pbcn*, even though there is another different modification [25] obtained from fused-salt electrolysis. The crystal structure of LaMo₈O₁₄ along with other lanthanides e.g., RMo₈O₁₄ (R = Ce, Pr, Nd, Sm) [26-29] has been fully described in detail. Therefore, only a short description will be given here. The crystal structure contains two different bicapped Mo₈ clusters with a 1:1 ratio. According to the different face capping, Mo₈ clusters were defined differently with *Cis* and *Trans* as shown in Figure 3.10. Each Mo atom is connected with 5 oxygen atoms and two

independent La^{III} cations are surrounded by 12 oxygen atoms forming a distorted cuboctahedron.

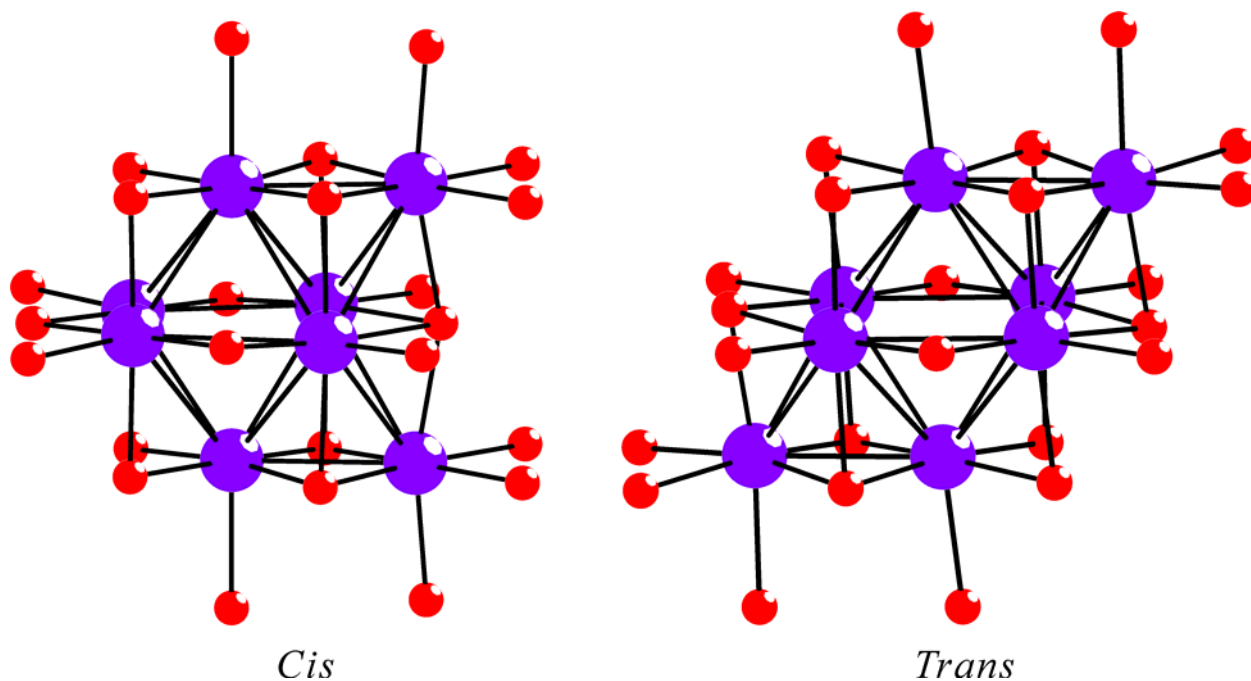


Figure 3.10 Two bicapped Mo_8 clusters in $\text{LaMo}_8\text{O}_{14}$. *Cis* (left) and *Trans* (right).

$\text{Pb}_{0.69}\text{Mo}_4\text{O}_6$, on the other hand, will be described with a new modulation. This structure type, which contains infinite chains of trans-edge-sharing Mo_6 octahedra, was first reported in NaMo_4O_6 [21] by Torardi and McCarley. Strongly related ternary molybdenum oxides, such as KMo_4O_6 [30,31], SnMo_4O_6 [32], and $\text{Ba}_{0.62}\text{Mo}_4\text{O}_6$ [33], have also been successfully synthesized in recent years. For $\text{Ba}_{0.62}\text{Mo}_4\text{O}_6$, the stoichiometric formula was determined to be $\text{Ba}_5\text{Mo}_{32}\text{O}_{48}$ based on weak supercell reflections found during the crystal structure determination. The structure of $\text{Pb}_{0.69}\text{Mo}_4\text{O}_6$ was first reported as $\text{Pb}_{0.75}\text{Mo}_4\text{O}_6$ [34] in 1991. The space groups $P4/mbm$ (No. 127) and $P4/mnc$ (No. 128) were selected for the subcell and supercell of this compound, respectively, based on the single crystal structure determination.

The model for the supercell structure with a formula $\text{Pb}_3\text{Mo}_{16}\text{O}_{24}$ exhibits the short distance (0.6 Å) between Pb atoms along the tunnel. There are also reduced molybdenum oxides like $\text{La}_{1.16}\text{Mo}_8\text{O}_{16}$ [35] with an incommensurate modulated crystal structure.

As shown in Figure 3.11, the basic structure from our subcell refinement is the same as reported by Wang et al. [34]. The structure consists of infinite chains of trans-edge sharing Mo_6 octahedra, which are linked by triangularly bonded oxygen atoms. The Pb cations occupy eight-coordinated sites within the tunnels between the cross-link chains. The Mo–O bond distances in the basic structure of $\text{Pb}_{0.69}\text{Mo}_4\text{O}_6$ range from 2.02 to 2.07 Å, which is quite comparable with those in other isostructural ternary molybdenum oxides like NaMo_4O_6 (2.00 – 2.06 Å), KMo_4O_6 (2.04 – 2.07 Å) and SnMo_4O_6 (2.01 – 2.08 Å). However, the bond distances between the cations and O atoms differ significantly, e.g., Sn–O: 2.29 Å; Pb–O: 2.52 Å; Na–O: 2.74 Å; K–O: 2.79 Å, as expected based on the different cation sizes. There are two types of Mo atoms, namely Mo (basal) and Mo (apical), respectively, in the basic structure of $\text{Pb}_{0.69}\text{Mo}_4\text{O}_6$. Each basal Mo atom connects with 7 other Mo atoms, and every apical Mo atom is connected to 6 other Mo atoms. The bond distances of Mo (basal)–Mo (basal) and Mo (apical)–Mo (apical) along the infinite chain direction are all 2.84 Å, and Mo (basal)–Mo (apical) is 2.79 Å. The shortest Mo–Mo bond distances (2.78 Å) are found between basal Mo atoms on the sharing edge of two Mo_6 octahedra. For comparison, three types of Mo–Mo bond distances in SnMo_4O_6 are the same as found in $\text{Pb}_{0.76}\text{Mo}_4\text{O}_6$. However, the Mo–Mo bond distances in KMo_4O_6 are slightly longer, i.e. 2.95, 2.81, and 2.76 Å, respectively. Based on the presence of weak superlattice reflections, Wang et al. built a commensurate supercell model with an intriguing Pb ordering, with the formula $\text{Pb}_3\text{Mo}_{16}\text{O}_{24}$. The $[\text{Mo}_8\text{O}_{12}^{2-}]$ framework, e.g., infinite chains of trans-edge sharing octahedra in this 3D

superstructure remains the same features as found in the basic cell. A similar scenario was found in $\text{Ba}_5\text{Mo}_{32}\text{O}_{48}$ [33], with eight times of the basic cell along the c direction.

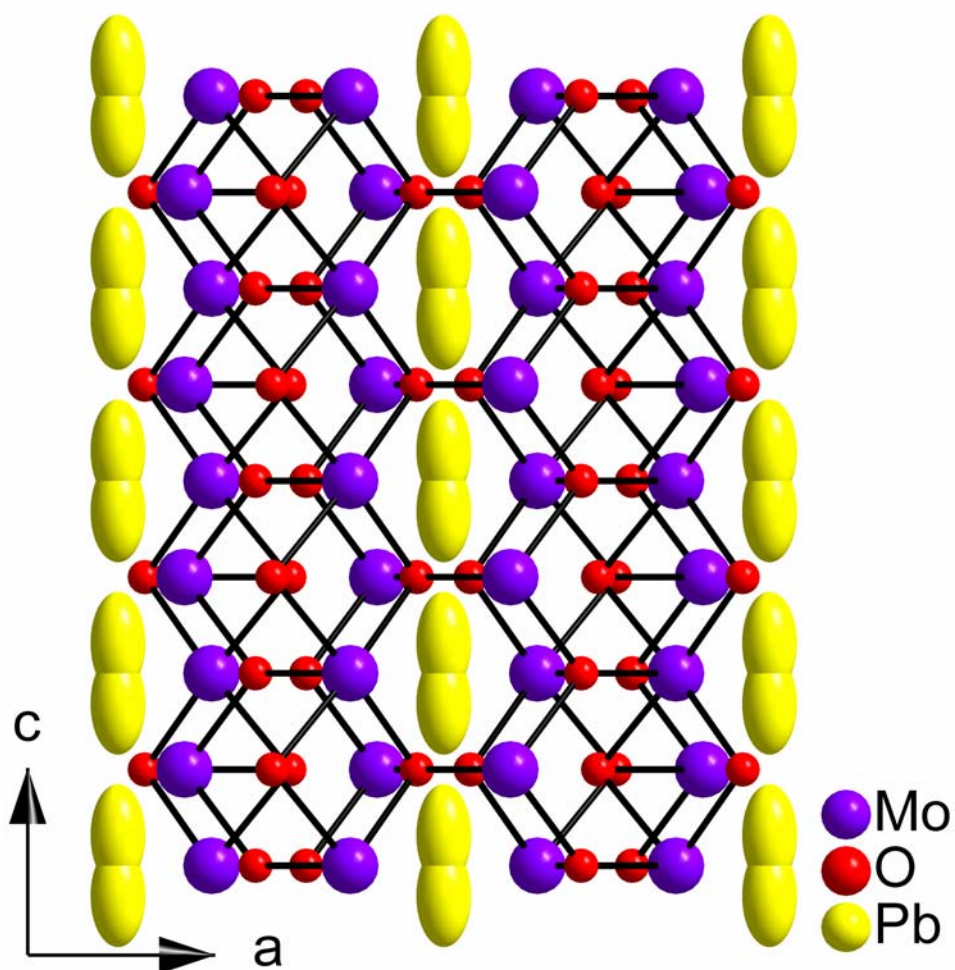


Figure 3.11 Basic $\text{Pb}_{0.69}\text{Mo}_4\text{O}_6$ structure obtained from the main reflections. The Pb atoms exhibit a split position around $(0, 0, 0)$.

The origin of the modulation is a mismatch between the repeat distances of the Pb chain and that of the cavities in the framework and thus empty cavities are needed (Figure 3.12). The result is that the Pb atoms order inside the channel, without affecting the

surrounding Mo_4O_6 framework that remains rigid. A low temperature X-ray investigation was attempted, but the crystals break when subjected to the cold N_2 gas stream.

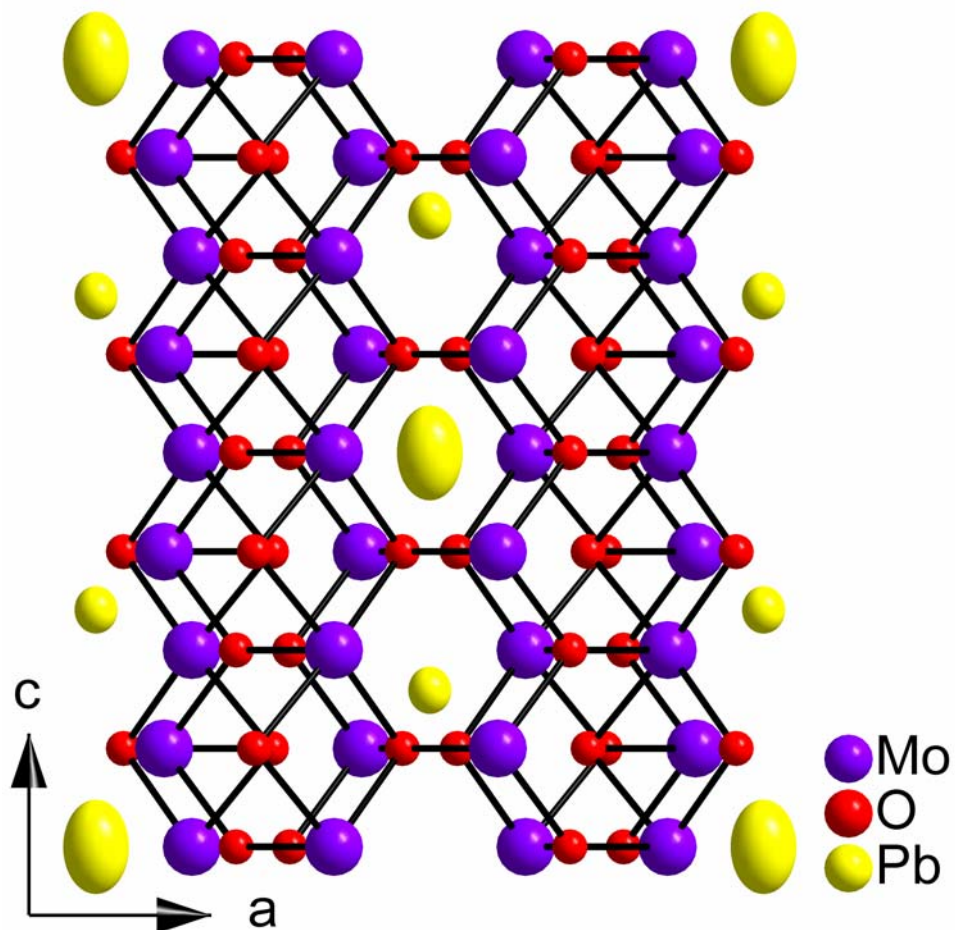


Figure 3.12 Modulated description of the structure. Thermal ellipsoids are indicated.

3.2.4 Electronic structure investigation

We utilized the LMTO method (LMTO = linear muffin tin orbitals) [36] for the electronic structure calculations for both Mo compounds. Since all atomic sites in the structure of $\text{LaMo}_8\text{O}_{14}$ are fully occupied, the model of this compound chosen for the calculation was taken directly from the single crystal structure determination [20] with the

Pbcn symmetry. On the other hand, the model used for the calculation for $\text{Pb}_{0.69}\text{Mo}_4\text{O}_6$ was generated from the (3+1)D superstructure resulting in the *P4/mnc* symmetry. As site deficiencies of the Pb positions can not be directly calculated with our methods, we had to propose an ordered model occurring with exclusively full occupancies, e.g., all Pb sites (2a, 4e), Mo sites (8g, 8h, 16i) and O sites (8g, 8h, $16i \times 2$) were treated as fully occupied, which leads to the formula $\text{Pb}_{0.75}\text{Mo}_4\text{O}_6$ without changing the space group *P4/mnc*.

The calculated electronic band structures of $\text{LaMo}_8\text{O}_{14}$ and “ $\text{Pb}_{0.75}\text{Mo}_4\text{O}_6$ ” are shown in Figure 3.13 and 3.14. In both cases, the Fermi level, E_F , is arbitrarily placed at 0 eV.

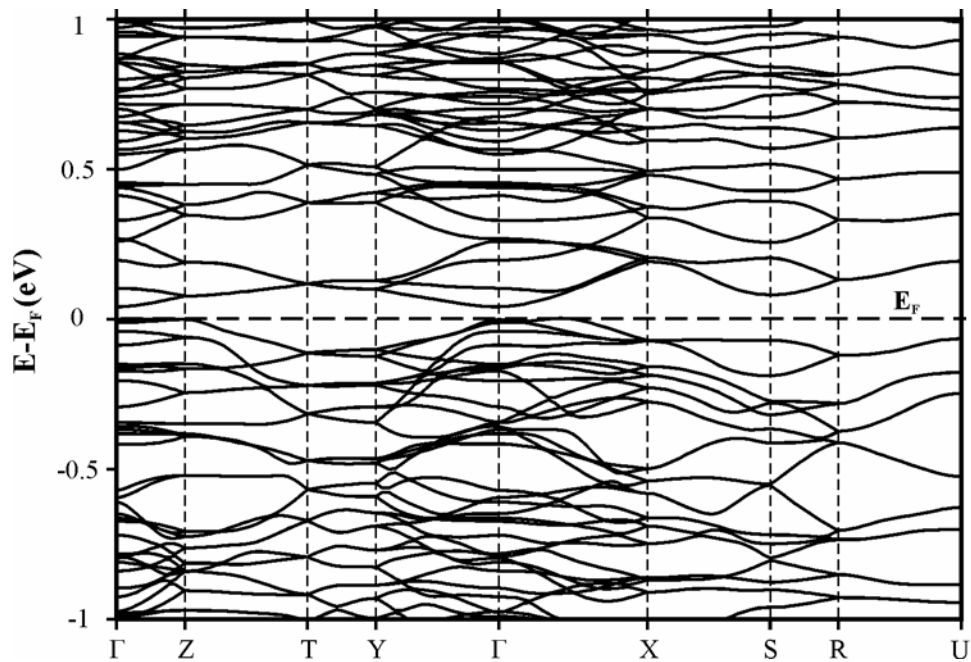


Figure 3.13 Band structure of $\text{LaMo}_8\text{O}_{14}$.

Compared with “ $\text{Pb}_{0.75}\text{Mo}_4\text{O}_6$ ”, the bands of $\text{LaMo}_8\text{O}_{14}$ are much more flat, indicating low mobility but higher Seebeck coefficient. On the other hand, the dispersion of the curves for “ $\text{Pb}_{0.75}\text{Mo}_4\text{O}_6$ ” is quite directionally dependent in the first Brillouin zone, e.g., the bands

from Γ to Z and A to M are quite steep, while all the other bands are relatively flat. The steep bands ($\Gamma \rightarrow Z$ and $A \rightarrow M$) are mostly dominated by strong intrachain Mo–Mo bonding. The flat bands ($\Gamma \rightarrow X$, $X \rightarrow M$, $M \rightarrow \Gamma$, $Z \rightarrow R$, and $R \rightarrow A$) represent the weak interchain interaction via oxygen atoms. Metallic character is most likely for “ $\text{Pb}_{0.75}\text{Mo}_4\text{O}_6$ ” at the room temperature because there is no band gap observed at Fermi level, while $\text{LaMo}_8\text{O}_{14}$ containing two different bicapped Mo_8 clusters is a semiconductor with a band gap around 0.1 eV.

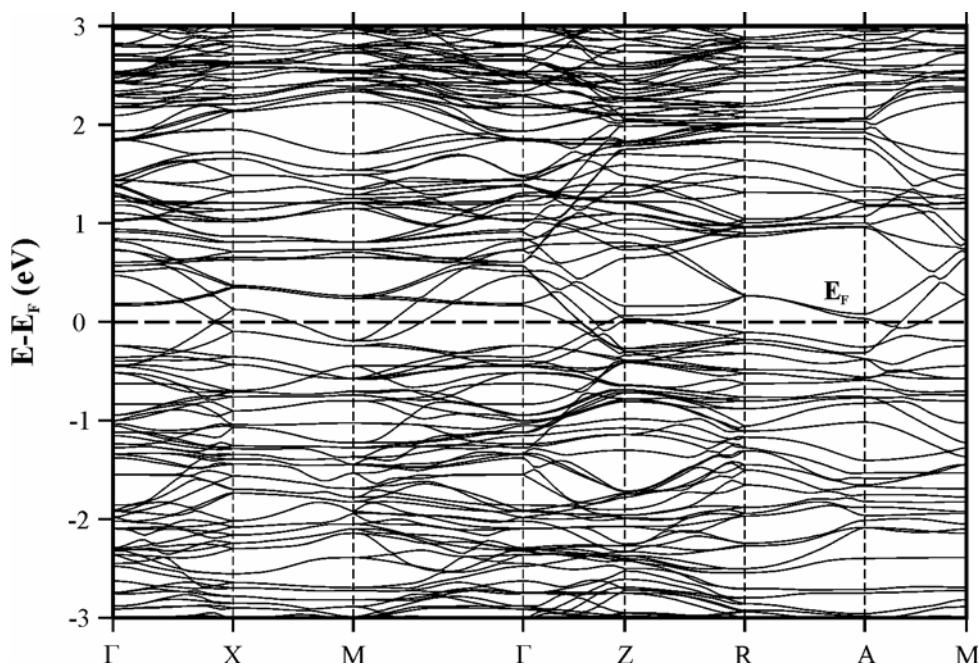


Figure 3.14 Band structure of $\text{Pb}_{0.75}\text{Mo}_4\text{O}_6$.

3.2.5 Transport property measurements

We pressed part of the ground phase-pure sample of $\text{LaMo}_8\text{O}_{14}$ and $\text{Pb}_{0.69}\text{Mo}_4\text{O}_6$ into a bar-shaped pellet for the temperature dependent electrical resistivity and Seebeck coefficient measurements.

The electrical resistivity as shown in Figure 3.15 suggests that $\text{LaMo}_8\text{O}_{14}$ is a semiconductor, with the resistivity from $\rho = 2.8 \Omega\text{cm}$ at 300 K to $\rho = 8.9 \Omega\text{cm}$ around 175 K. However, the room temperature resistivity we obtained is much higher than the reported value of $4.4 \times 10^{-2} \Omega\text{cm}$ [37], which is possibly because the density of our cold-pressed pellet (measured to be $4.08 \times 10^{-3} \text{gcm}^{-3}$) is only 56% of the calculated density of $7.32 \times 10^{-3} \text{gcm}^{-3}$ [20].

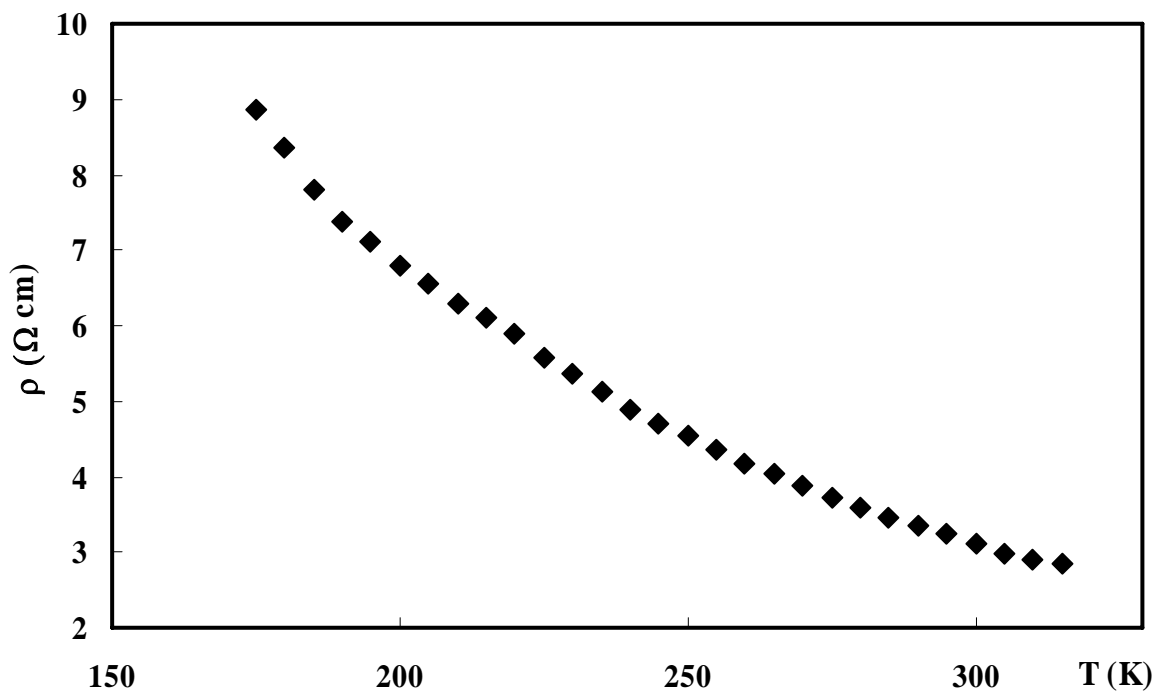


Figure 3.15 Electrical resistivity measurement of $\text{LaMo}_8\text{O}_{14}$.

In order to obtain transport properties from more condensed materials, e.g. high density of pellets, large amount sample of $\text{LaMo}_8\text{O}_{14}$ has been sent to our collaborators in the Department of Physics & Astronomy at Clemson University for measurements on the hot-pressed pellets.

The Seebeck measurement (Figure 3.16), on the other hand, shows that $\text{LaMo}_8\text{O}_{14}$ is an *n*-type semiconductor with a high Seebeck coefficient of $-94 \mu\text{VK}^{-1}$ at 300 K, the absolute value of which is comparable with one of the best thermoelectric oxide NaCo_2O_4 with Seebeck coefficient around $100 \mu\text{VK}^{-1}$ at room temperature [38].

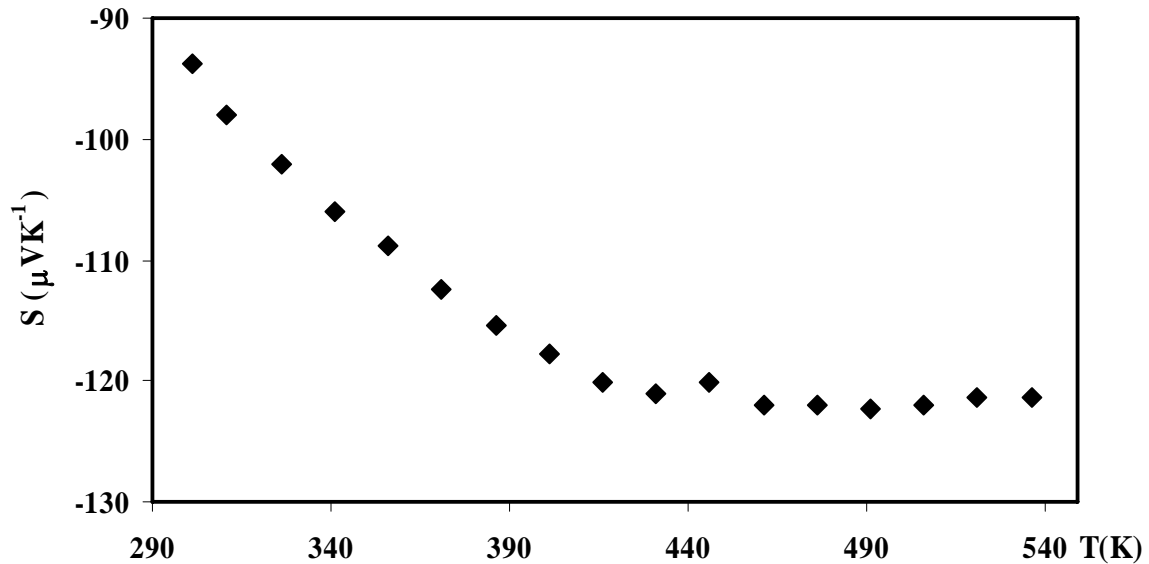


Figure 3.16 Seebeck coefficient measurement of $\text{LaMo}_8\text{O}_{14}$.

Electronic structure calculations suggest a metallic behavior for $\text{Pb}_{0.69}\text{Mo}_4\text{O}_6$. However, our experimental results show that the electrical resistivity increases with decreasing temperature, namely from $\rho = 0.2 \Omega\text{cm}$ at 295 K to $\rho = 6.9 \Omega\text{cm}$ around 5 K (Figure 3.17), which is typical for semiconductors. The electrical properties of $\text{Pb}_{0.69}\text{Mo}_4\text{O}_6$ we found from the room temperature down to 5 K are different from that of all the other $\text{A}_x\text{Mo}_4\text{O}_6$ reported so far, e.g., KMo_4O_6 [31], and SnMo_4O_6 [32] undergo a metal-nonmetal transition at low temperature; InMo_4O_6 [39] on the other hand is a metallic conductor with a normal temperature dependence of the resistivity down to 2 K.

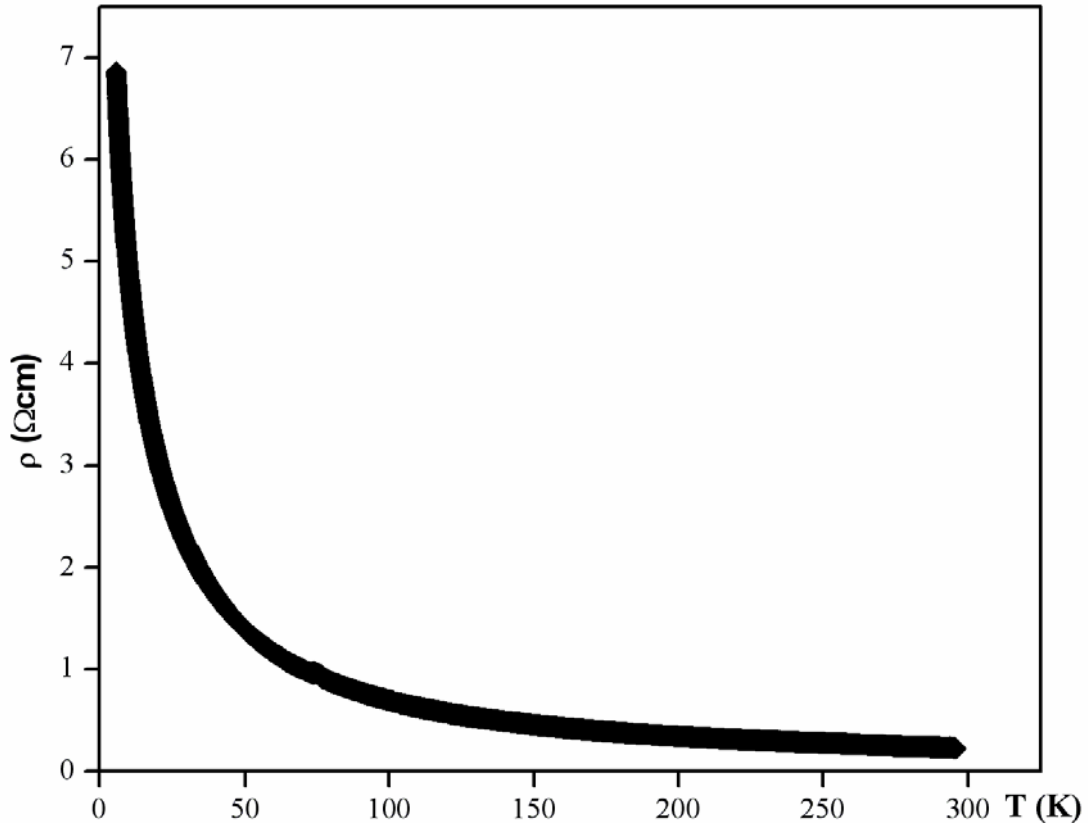


Figure 3.17 Electrical resistivity measurement of $\text{Pb}_{0.69}\text{Mo}_4\text{O}_6$.

The Seebeck coefficient (S) measurement (Figure 3.18) reveals that the charge carriers of $\text{Pb}_{0.69}\text{Mo}_4\text{O}_6$ are predominantly n -type. Between 300 K and 550 K, the Seebeck coefficient of $\text{Pb}_{0.69}\text{Mo}_4\text{O}_6$ decreases from $-6.9 \mu\text{VK}^{-1}$ at 305 K to $-1.3 \mu\text{VK}^{-1}$ at 550 K, which is typical for metals and very small band gap semiconductors.

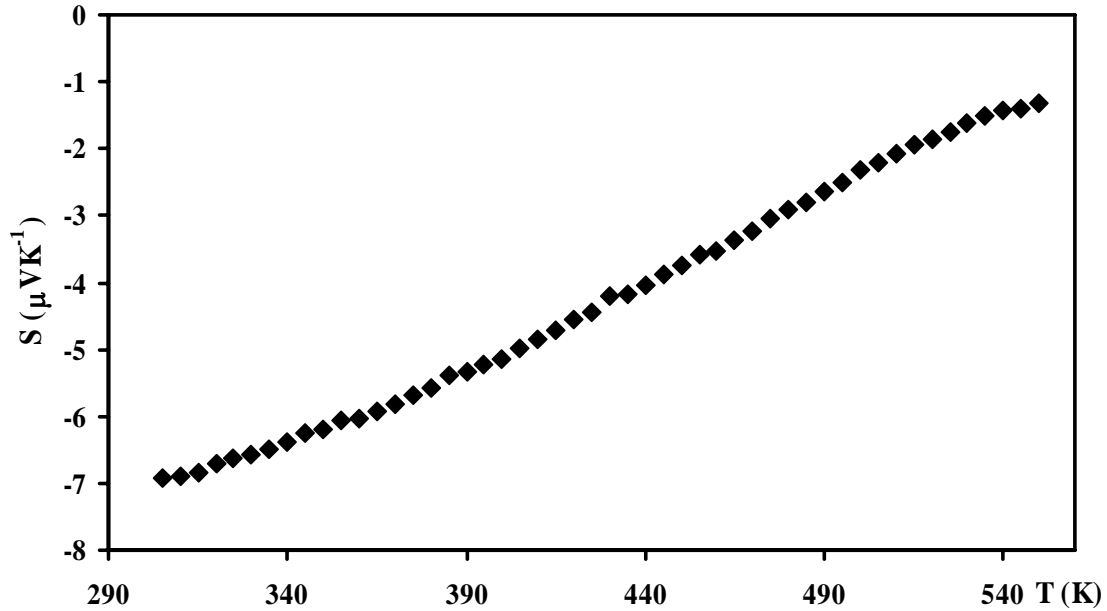


Figure 3.18 Seebeck coefficient measurement of $\text{Pb}_{0.69}\text{Mo}_4\text{O}_6$.

3.2.6 Conclusion

Two ternary molybdenum oxides, $\text{Pb}_{0.69}\text{Mo}_4\text{O}_6$ and $\text{LaMo}_8\text{O}_{14}$, were synthesized by high temperature solid state reactions. The new modulated structure of $\text{Pb}_{0.69}\text{Mo}_4\text{O}_6$ was presented, as well as the electronic structure investigation and transport property measurements from 5 K to 550 K. The Seebeck coefficient of $\text{Pb}_{0.69}\text{Mo}_4\text{O}_6$ was determined to be too low for the thermoelectric applications. On the other hand, $\text{LaMo}_8\text{O}_{14}$ shows very promising thermoelectric performances in a wide temperature range and further investigations of the properties of this oxide are in progress.

References

- [1] I. Terasaki; Y. Sasago; Uchinokura, K. *Phys. Rev. B* **1997**, *56*, 12685-12687.
- [2] A.C. Masset; C. Michel; A. Maignan; O. Toulononde; F. Studer; B. Raveau; Hejtmanek, J. *Phys. Rev. B* **2000**, *62*, 166-175.
- [3] R. Funahashi; I. Matsubara; H. Ikuta; T. Takeuchi; U. Mizutani; Sodeoka, S. *Jpn. J. Appl. Phys.* **2000**, *39*, 1127-1129.
- [4] H. Leigny; D. Grebille; O. Prez; A.C. Masset; M. Hervieu; Raveau, B. *Acta Crystallogr. B* **2000**, *56*, 173-182.
- [5] Koumoto, K.; Terasaki, I.; Funahashi, R. *Mat. Res. Bull.* **2006**, *31*, 206-210.
- [6] Takahata, K.; Yiguchi, Y.; Tanaka, D.; Itoh, T.; Terasaki, I. *Phys. Rev. B* **2000**, *61*.
- [7] Satake, A.; Tanaka, H.; Ohkawa, T.; Fujii, T.; Terasaki, I. *J. Appl. Phys.* **2004**, *96*, 931-933.
- [8] Xu, J.; Assoud, A.; Soheilnia, N.; Derakhshan, S.; Cuthbert, H. L.; Greendan, J. E.; Whangbo, M. H.; Kleinke, H. *Inorg. Chem.* **2005**, *44*, 5042-5046.
- [9] Xu, J.; Christensen, J.; Lidin, S.; Assoud, A.; Kleinke, H. *J. Solid Stat. Chem.*, submitted.
- [10] Schneemeyer, L. F.; Waszczak, J. V.; Siegrist, T.; Dover, R. B. V.; Rupp, L. W.; Batlogg, B.; Cava, R. J.; Murphy, D. W. *Nature* **1987**, *328*, 601-603.
- [11] Vershinin, M.; Misra, S.; Ono, S.; Abe, Y.; Ando, Y.; Yazdani, A. *Science* **2004**, *303*, 1995-1998.
- [12] Kratochvil, B.; Jensovsky, L. *Acta Crystallogr. B* **1977**, *33*, 2596-2598.
- [13] Falck, L.; Lindqvist, O.; Mark, W. *Acta Crystallogr. B* **1978**, *34*, 1450-1453.
- [14] Calos, N. J.; Forrester, J. S.; Schaffer, G. B. *J. Solid State Chem.* **1996**, *122*, 273-280.
- [15] Gougeon, P.; Gall, P.; Halet, J.-F.; Gautier, R. *Acta Crystallogr. B* **2003**, *59*, 472-478.
- [16] Koo, H.-J.; Whangbo, M.-H.; McCarroll, W. H.; Greenblatt, M.; Gautier, R.; Halet, J.-F.; Gougeon, P. *Solid State Commun.* **1998**, *108*, 539-544.
- [17] Gall, P.; Barrier, N.; Gautier, R.; Gougeon, P. *Inorg. Chem.* **2002**, *41*, 2879-2885.
- [18] Tortelier, J.; Gougeon, P. *Inorg. Chem.* **1998**, *37*, 6229-6236.
- [19] Tortelier, J.; Gall, P.; Noel, H.; Gougeon, P. *J. Solid Stat. Chem.* **2000**, *152*, 403-411.
- [20] Kerihuel, G.; Tortelier, J.; Gougeon, P. *Acta Crystallogr. C* **1996**, *52*, 2389-2393.
- [21] Torardi, C. C.; McCarley, R. E. *J. Am. Chem. Soc.* **1979**, *101*, 3963-3964.
- [22] Sheldrick, G. M. *SHELXTL*; Version 5.12 ed.; Siemens Analytical X-Ray Systems: Madison, WI., 1995.
- [23] Farrugia, L. J. *J. Appl. Cryst.* **1999**, *32*, 837-838.
- [24] Petricek, V.; Dusek, M.; Palatinus, L. *Jana2000. The crystallographic computing system*; Institute of Physics: Praha, Czech Republic, 2000.
- [25] Leligny, H.; Labbe, P.; Ledesert, M.; Hervieu, M.; Raveau, B.; McCarroll, W. H. *Acta Crystallogr. B* **1993**, *49*, 444-454.
- [26] Kerihuel, G.; Gougeon, P. *Acta Crystallogr. C* **1995**, *51*, 787-790.
- [27] Kerihuel, G.; Gougeon, P. *Acta Crystallogr. C* **1995**, *51*, 1475-1478.
- [28] Gougeon, P.; McCarley, R. E. *Acta Crystallogr. C* **1991**, *47*, 241-244.
- [29] Tortelier, J.; Gougeon, P. *Acta Crystallogr. C* **1997**, *53*, 668-671.
- [30] Hoffman, R.; Hoppe, R.; Bauer, K.; Range, K.-J. *J. Less-Common Met.* **1990**, *161*, 279-193.
- [31] Ramanujachary, K. V.; Greenblatt, M. *J. Solid State Chem.* **1993**, *102*, 69-78.

- [32] Jung, D.; Lee, B.-H.; Kim, S.-J.; Kang, W. *Chem. Mater.* **2001**, *13*, 1625-1629.
- [33] Torardi, C. C.; McCarley, R. E. *J. Solid State Chem.* **1981**, *37*, 393-397.
- [34] Wang, S. L.; Yeh, J. Y. *Acta Crystallogr. B* **1991**, *47*, 446-451.
- [35] Leligny, H.; Labbé, P.; Ledserté, M.; Raveau, B. *Acta Crystallogr. B* **1992**, *48*, 134-144.
- [36] Skriver, H. L. *The LMTO Method*; Springer: Berlin, Germany, 1984.
- [37] Ramanujachary, K. V.; Jones, E. B.; Greenblatt, M.; McCarroll, W. H. *J. Solid Stat. Chem.* **1995**, *117*, 261-268.
- [38] Motohashi, T.; Naujalis, E.; Ueda, K.; Isawa, K.; Karppinen, M.; Yamauchi, H. *Appl. Phys. Lett.* **2001**, *79*, 1480-1482.
- [39] McCarley, R. E. *Polyhedr.* **1986**, *5*, 51-61.

4. Ternary thallium chalcogenides

Most advanced thermoelectrics are narrow gap semiconductors with heavy main group elements [1-4]. Efforts into ternary main group thallium tellurides revealed excellent thermoelectric materials, which include Tl_2GeTe_5 and Tl_2SnTe_5 [5], TlSbTe_2 [6], Tl_9BiTe_6 [7], and TlBiTe_2 [8]. These materials bestow with their extremely low thermal conductivity. Thermoelectric properties of several quaternary thallium tellurides [9] have also been reported recently. On the other hand, thallium selenides have not been widely investigated as candidates for thermoelectric applications. There are only a few quaternary examples from DiSalvo et al. [10]: $\text{Tl}_2\text{Cu}_2\text{Sn}_2\text{Se}_6$ and $\text{Tl}_2\text{Au}_2\text{Sn}_2\text{Se}_6$ have very low electrical conductivities, hence poor thermoelectric properties; $\text{Tl}_5\text{AgTi}_6\text{Se}_{27}$ shows $\sigma = 8 \times 10^{-5} \Omega^{-1}\text{cm}^{-1}$ and $S = -820 \mu\text{VK}^{-1}$, $\text{Tl}_3\text{CuNb}_2\text{Se}_{12}$ shows $\sigma = 4 \times 10^{-5} \Omega^{-1}\text{cm}^{-1}$ and $S = +770 \mu\text{VK}^{-1}$, and $\text{Tl}_{11.5}\text{Sb}_{11.5}\text{Cu}_8\text{Se}_{27}$ $\sigma = 4 \Omega^{-1}\text{cm}^{-1}$ and $S = +75 \mu\text{VK}^{-1}$ (all at 300 K). Compared with other tellurides like TlSbTe_2 [6], which exhibits outstanding thermoelectric performance with $\sigma = 1 \times 10^{+3} \Omega^{-1}\text{cm}^{-1}$ and $S = +80 \mu\text{VK}^{-1}$ at room temperature, higher electrical conductivity of thallium selenides is required for the thermoelectric applications, while the Seebeck coefficient is acceptable. During the past few years, our group has characterized several new ternary tin selenides [11-13] and antimony selenides [14,15], all of which exhibit low electrical conductivity as well. In this chapter, the results on several new ternary thallium selenides including $\text{Tl}_{2.35}\text{Sb}_{8.65}\text{Se}_{14}$, $\text{Tl}_{1.93}\text{Sb}_{8.07}\text{Se}_{13}$, and $\text{Tl}_{2.04}\text{Bi}_{7.96}\text{Se}_{13}$ will be presented, as well as transport properties of two known compounds, Tl_2SnSe_3 [16] and Tl_2SnTe_3 [17,18].

4.1 Synthesis and single crystal structure determination of new compounds

4.1.1 Synthesis

The elements were loaded into silica tubes, which were then sealed under vacuum. Subsequently, the tubes were heated in a resistance furnace to 923 K for 12 hours, and then cooled to room temperature at a rate of 5 K per hour.

Tl_2SnSe_3 and Tl_2SnTe_3 are known compounds, and exact stoichiometric ratios were used in order to get phase pure samples. Black needle crystals were selected from other three reactions for the single crystal structure determination in order to find the exact stoichiometric ratio, which turned out to be $\text{Tl}_{2.35}\text{Sb}_{8.65}\text{Se}_{14}$, $\text{Tl}_{1.93}\text{Sb}_{8.07}\text{Se}_{13}$ and $\text{Tl}_{2.04}\text{Bi}_{7.96}\text{Se}_{13}$. Then the same reaction process was repeated by using starting materials with the ratio obtained from the structure refinement. All compounds except $\text{Tl}_{2.04}\text{Bi}_{7.96}\text{Se}_{13}$ were obtained phase-pure according to the X-ray diffractogram.

Five additional reactions were carried out in order to investigate the phase width of $\text{Tl}_{2.35}\text{Sb}_{8.65}\text{Se}_{14}$. The reactions started from different Tl/Sb ratios, from 1.5 : 9.5 to 3.5 : 7.5 in increments of 0.5, keeping $\{n(\text{Tl}) + n(\text{Sb})\}/n(\text{Se}) = 11/14$. The final products were characterized by X-ray diffraction. None of the reactions with $\text{Tl} \neq 2.35$ gave yields above $\approx 85\%$, which suggests a rather small phase range for $\text{Tl}_{2.35}\text{Sb}_{8.65}\text{Se}_{14}$.

4.1.2 Single crystal structure determination

Three needle shaped crystals were mounted onto a BRUKER Smart Apex CCD diffractometer utilizing Mo-K α_1 radiation. The data were collected by scans of 0.3° in ω in two blocks of 606 frames at $\phi = 0^\circ$ and 120° , with exposure times of 60 seconds per frame.

Tl_{2.35}Sb_{8.65}Se₁₄: The cell parameters indicated that the new thallium selenide may be isostructural with K_{2.5}Sb_{8.5}Se₁₄ [19]. We therefore used the atomic positions of the K_{2.5}Sb_{8.5}Se₁₄ structure (ignoring the disorder within the structure) as a starting point for our structure refinement, carried out with the SHELXTL program package [20]. After least-squares refinement, high electron density peaks of 17 e/Å³ and 15 e/Å³ remained at distances of 0.86 Å to Tl1 and 0.92 Å to Tl3, respectively, with R1/wR2 = 7.54/20.54%. A similar scenario was described in case of K_{2.5}Sb_{8.5}Se₁₄. In order to facilitate a comparison with K_{2.5}Sb_{8.5}Se₁₄, Sb5 and Sb7 were assigned to the electron density peaks near Tl1 and Tl3, assuming a disordered model with Tl/Sb split sites. Subsequently, their occupancy ratios were refined to Tl1/Sb5 = 65.1(5)/34.9% and Tl3/Sb7 = 69.6(6)/30.4%. The final refinement resulted in residual values of R1 = 4.4% and wR2 = 10.8%, the formula being Tl_{2.35}Sb_{8.65}Se₁₄. Crystallographic details are listed in Table A. 8, atomic positions and equivalent displacement parameters in Table A. 9 and selected bond distances in Table A. 10 in the Appendix.

Tl_{1.93}Sb_{8.07}Se₁₃ and Tl_{2.04}Bi_{7.96}Se₁₃: The cell parameters for the refinement were also firstly taken from their K analogues. Quite similar to Tl_{2.35}Sb_{8.65}Se₁₄, there are also disorders at Tl sites found in these two compounds. However, disorders are more complicated here. For Tl_{1.93}Sb_{8.07}Se₁₃, we found split sites in all Tl positions with Tl1/Sb8A/Sb8B = 21.6(3)/66.1(4)/12.3%, Tl2/Sb9A/Sb9B = 71.2(4)/19.9(3)/8.9%, and Tl3A/Tl3B =

88.4(2)/11.6% resulting in the formula, $\text{Tl}_{1.93}\text{Sb}_{8.07}\text{Se}_{13}$ and final residual values were $R1 = 6.5\%$ and $wR2 = 10.7\%$. For the Bi case, a disordered model was induced at all Tl sites as well with the short distances of 0.41 Å between Tl1 and Bi8, 0.61 Å between Tl2 and Bi9, and 0.54 Å between Tl3 and Bi10. Because of the similar scattering factor of Tl and Bi, they can not be distinguished by the X-ray diffraction and the refinements with switched Tl and Bi sites gave the same refinement residuals. However, the radius of Tl^+ is slightly larger than that of Bi^{3+} , e.g., Tl-Se bonds are longer than the Bi-Se bonds. The disordered atoms were treated as in the similar scenario in the structure of $\text{Tl}_{2.35}\text{Sb}_{8.65}\text{Se}_{14}$: Tl atoms were assigned to the sites coordinating with 8 or 9 Se atoms, and Bi atoms to the sites with more distorted coordination spheres. The final refinement residuals turned out to be $R1 = 7.9\%$ and $wR2 = 12.1\%$, with $\text{Tl1/Bi8} = 51.1(1)/48.9\%$, $\text{Tl2/Bi9} = 80.5(1)/19.5\%$, and $\text{Tl3/Bi10} = 72.4(1)/27.6\%$, resulting in the formula $\text{Tl}_{2.04}\text{Bi}_{7.96}\text{Se}_{13}$. Crystallographic details for both compounds are listed in Table A. 11-16 in the Appendix.

4.2 Crystal structures

Before we found $\text{Tl}_{2.35}\text{Sb}_{8.65}\text{Se}_{14}$ and $\text{Tl}_{1.93}\text{Sb}_{8.07}\text{Se}_{13}$, only three thallium antimony selenides were known, TlSbSe_2 [21], Tl_3SbSe_3 [22], and Tl_9SbSe_6 [23]. $\text{Tl}_{2.04}\text{Bi}_{7.96}\text{Se}_{13}$ is the third thallium bismuth selenide, the other two being TlBiSe_2 [24] and Tl_9BiSe_6 [25]. Since the crystal structures of $\text{Tl}_{2.35}\text{Sb}_{8.65}\text{Se}_{14}$, $\text{Tl}_{1.93}\text{Sb}_{8.07}\text{Se}_{13}$ and $\text{Tl}_{2.04}\text{Bi}_{7.96}\text{Se}_{13}$ are rather similar, we will describe the details for $\text{Tl}_{2.35}\text{Sb}_{8.65}\text{Se}_{14}$ and highlight the significant differences between these three compounds. The crystal structure of $\text{Tl}_{2.35}\text{Sb}_{8.65}\text{Se}_{14}$ is shown in Figure 4.1, which omits the Tl–Se bonds for clarity.

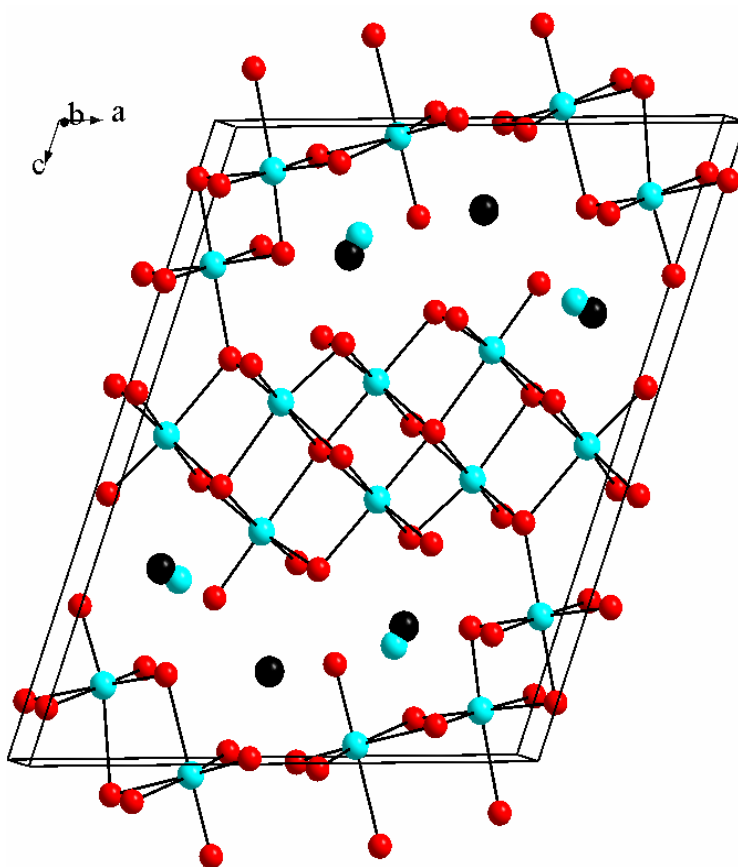


Figure 4.1 Crystal structure of $\text{Tl}_{2.35}\text{Sb}_{8.65}\text{Se}_{14}$ viewed along the b axis. Tl: black; Sb: cyan; Se: red.

Many thallium chalcogenides form the same structure type as their alkali analogues, such as Tl_2SnSe_3 [16] and $\text{Tl}_2\text{Ag}_2\text{SnTe}_4$ [10], while some compounds like $\text{Tl}_2\text{Ge}_2\text{Se}_5$ [26] and $\text{Tl}_6\text{Si}_2\text{Te}_6$ [27] show structures different to their formal alkali analogues. In this case, the new thallium selenide $\text{Tl}_{2.35}\text{Sb}_{8.65}\text{Se}_{14}$ is isostructural with its potassium analogue, $\text{K}_{2.5}\text{Sb}_{8.5}\text{Se}_{14}$. Within the structure of $\text{K}_{2.5}\text{Sb}_{8.5}\text{Se}_{14}$, disorder occurs both at the K and Se sites. However, $\text{Tl}_{2.35}\text{Sb}_{8.65}\text{Se}_{14}$ contains disorder only at the Tl1 and Tl3 sites with Sb5 and Sb7. No disorder was found at the Se sites of the structure of $\text{Tl}_{2.35}\text{Sb}_{8.5}\text{Se}_{14}$. The Tl–Se coordination spheres including contacts between the disordered Sb and Se atoms are depicted in Figure 4.2.

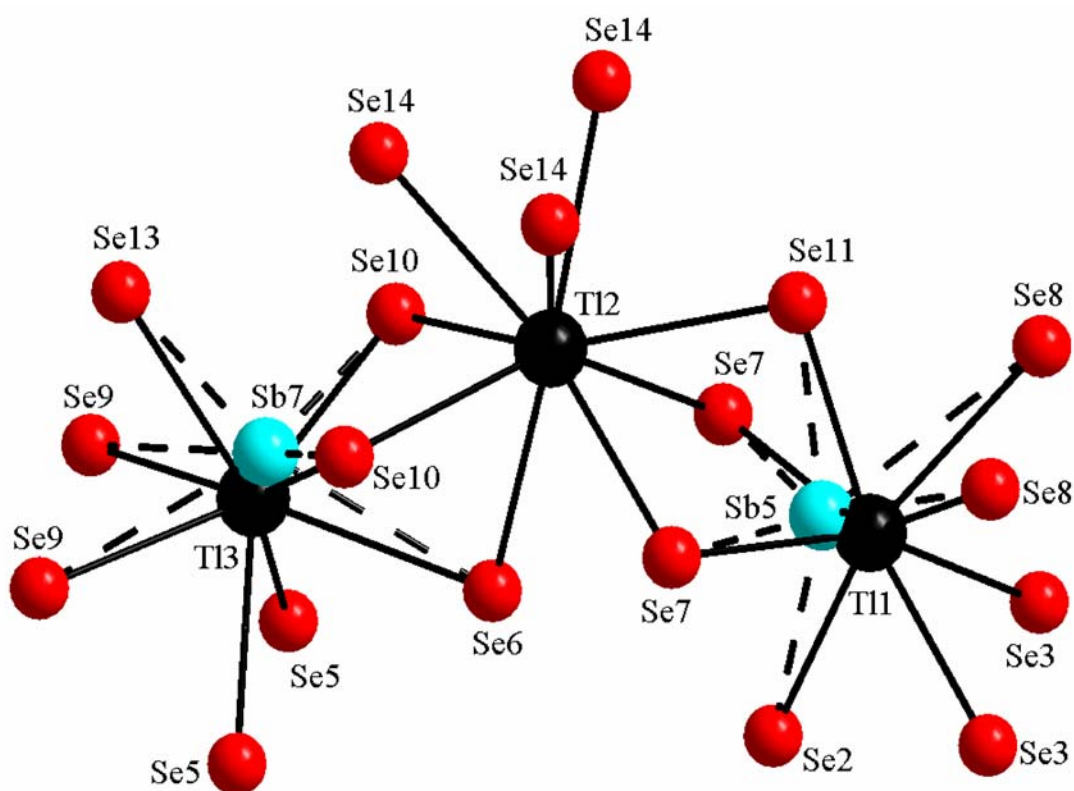


Figure 4.2 Coordination spheres of the three independent Tl sites of $\text{Tl}_{2.35}\text{Sb}_{8.65}\text{Se}_{14}$ with the disordered Sb atoms at the Tl1 and Tl3 sites.

It is noted that the Tl1–Sb5 and Tl3–Sb7 distances are too short for these atoms to occur together at a given site. Tl1 is coordinated by eight Se atoms with bond distances ranging from 3.15 Å to 3.37 Å, forming a distorted bicapped trigonal prism. The coordination environment of the Tl3 site is very similar to that of the Tl1 site with eight Tl–Se bonds ranging from 3.12 Å to 3.42 Å. On the other hand, the Tl2 sites are occupied solely by Tl, exhibiting nine Tl–Se bonds ranging from 3.28 Å to 3.59 Å in form of a distorted tricapped trigonal prism. These Tl–Se distances are comparable to the Tl–Se distances of the Tl atoms connected by eight Se atoms in TlSe (3.43 Å) [28].

Like $K_{2.5}Sb_{8.5}Se_{14}$, $Tl_{2.35}Sb_{8.65}Se_{14}$ contains infinite Sb–Se blocks reminiscent of the NaCl and Bi_2Te_3 motifs. All Sb atoms, except for Sb5 and Sb7, are coordinated by six Se atoms, forming edge-sharing severely distorted octahedra with Sb–Se bonds ranging from 2.62 Å to 3.45 Å, which compares nicely with the Sb–Se bonds in $K_{2.5}Sb_{8.5}Se_{14}$ (2.61 Å – 3.46 Å). Typically, related Sb–Se interactions occur in the binary compound Sb_2Se_3 [29] with its two symmetry-independent sites: Sb1 forms three bonds to Se atoms between 2.66 Å and 2.68 Å, plus three longer distances from 3.22 Å to 3.25 Å; Sb2 forms three short bonds to Se between 2.59 Å and 2.80 Å, plus two intermediate contacts of 3.00 Å, and two long distances of 3.49 Å. The different distances are caused by the steric effect of the lone pair of Sb^{3+} . Based on these Sb2–Se distances of Sb_2Se_3 , one could distinguish between short Sb–Se bonds, e.g., < 2.8 Å, intermediate contacts between 2.8 Å and 3.0 Å, and long distances, e.g., up to 3.6 Å. Then, Sb1 comprises two short bonds, two intermediate ones and one long distance to Se atoms. Sb2, Sb4, Sb8, Sb9 and Sb10 form three short bonds and three long contacts, and Sb3 and Sb6 are coordinated by Se atoms with six intermediate distances.

The Sb5 atom of $\text{Tl}_{2.35}\text{Sb}_{8.65}\text{Se}_{14}$, the atom with the formal distance of 0.68 Å to Tl1, is shifted towards the Se7 atoms, compared to Tl1. The bond distance between Sb5 and Se7 (2.67 Å) is significantly shorter than that between Tl3 and Se7 (3.15 Å). Accordingly, the Sb5–Se11 (3.00 Å) and Sb5–Se2 (3.25 Å) distances are shorter than the Tl1–Se11 (3.33 Å) and Tl1–Se2 (3.27 Å) bonds. On the other hand, the Sb5–Se8 distance (3.71 Å) is much longer than the Tl1–Se8 bond (3.37 Å). In contrast to the Tl1–Se3 bond of 3.37 Å, the distance between Sb5 and Se3 (3.88 Å) is too long for a significant interaction. Similarly, the Sb7 atom is closer to Se10 and Se13 than Tl3, which is reflected in distances of Sb7–Se10 (2.71 Å) and Sb7–Se13 (2.89 Å) being shorter than Tl3–Se10 (3.12 Å) and Tl3–Se13 (3.30 Å). Moreover, the distances Sb7–Se5 (3.97 Å), Sb7–Se6 (3.53 Å) and Sb7–Se9 (3.60 Å) are longer than Tl3–Se5 (3.42 Å), Tl3–Se6 (3.42 Å) and Tl3–Se9 (3.31 Å), respectively. The significantly different interactions lead to different coordination numbers of eight for Tl3 and six for Sb7. This situation is reminiscent of the $\text{La}_7\text{Sb}_9\text{S}_{24}$ structure with mixed La/Sb occupancies [30], and stems from the smaller size of Sb, compared to Tl and La, and its strong lone pair effect, in particular compared to La.

$\text{Tl}_{1.93}\text{Sb}_{8.07}\text{Se}_{13}$ and $\text{Tl}_{2.04}\text{Bi}_{7.96}\text{Se}_{13}$ are isostructural to each other and consists of a 3D framework which is very similar to that of $\text{Tl}_{2.35}\text{Sb}_{8.65}\text{Se}_{14}$. Like $\text{Tl}_{2.35}\text{Sb}_{8.65}\text{Se}_{14}$, $\text{Tl}_{1.93}\text{Sb}_{8.07}\text{Se}_{13}$ and $\text{Tl}_{2.04}\text{Bi}_{7.96}\text{Se}_{13}$ have also the same structure type as their corresponding K analogues [19]. The crystal structure of $\text{Tl}_{2.04}\text{Bi}_{7.96}\text{Se}_{13}$ is shown in Figure 4.3, and again the Tl–Se bonds were omitted for clarity. Unlike $\text{Tl}_{2.35}\text{Sb}_{8.65}\text{Se}_{14}$ containing only disorders at the Tl1 and Tl3 sites, $\text{Tl}_{1.93}\text{Sb}_{8.07}\text{Se}_{13}$ and $\text{Tl}_{2.04}\text{Bi}_{7.96}\text{Se}_{13}$ comprise disorders at all Tl sites. Especially in $\text{Tl}_{1.93}\text{Sb}_{8.07}\text{Se}_{13}$, three split sites occur both at Tl1 and Tl2, namely Tl1/Sb8A/Sb8B and Tl2/Sb9A/Sb9B respectively, and instead of having Tl/Sb disorder, there

is a Tl split position appearing at the Tl3 site. $\text{Tl}_{2.04}\text{Bi}_{7.96}\text{Se}_{13}$ contains only Tl/Bi order at all Tl sites.

Compared with Sb–Se blocks in $\text{Tl}_{2.35}\text{Sb}_{8.65}\text{Se}_{14}$, the infinite Sb–Se and Bi–Se blocks in $\text{Tl}_{1.93}\text{Sb}_{8.07}\text{Se}_{13}$ and $\text{Tl}_{2.04}\text{Bi}_{7.96}\text{Se}_{13}$ not only contain motifs like NaCl and Bi_2Te_3 , but also like CdI_2 . The distances of Sb–Se and Bi–Se bonds are ranging from 2.61 to 3.03 Å and from 2.74 to 3.21 Å, respectively, which are comparable with those in $\text{Tl}_{2.35}\text{Sb}_{8.65}\text{Se}_{14}$ and in $\text{K}_2\text{Bi}_8\text{Se}_{13}$.

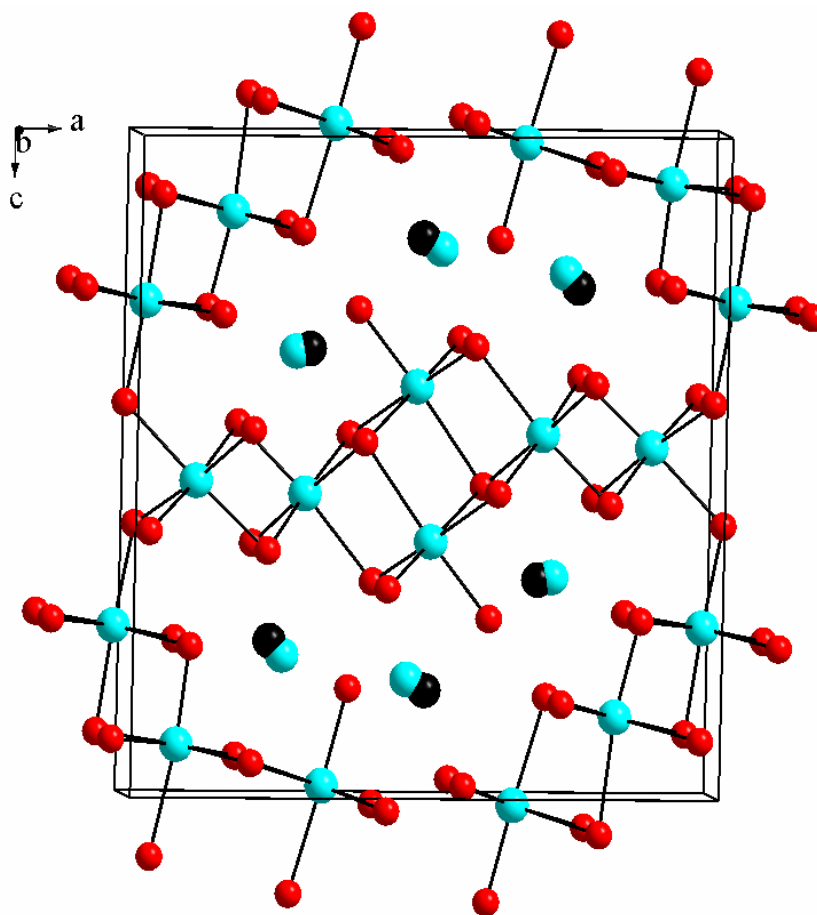


Figure 4.3 Crystal structure of $\text{Tl}_{2.04}\text{Bi}_{7.96}\text{Se}_{13}$ viewed along the b axis. Tl: black; Bi: cyan; Se: red.

Since there are no Sb–Sb and Se–Se bonding interactions, the oxidation states are readily assigned: $(\text{Tl}^+)_{2.5}(\text{Sb}^{3+})_{8.5}(\text{Se}^{2-})_{14}$, $(\text{Tl}^+)_2(\text{Sb}^{3+})_8(\text{Se}^{2-})_{13}$ and $(\text{Tl}^+)_2(\text{Bi}^{3+})_8(\text{Se}^{2-})_{13}$ like in the other Tl Sb selenides, TlSbSe_2 [24], Tl_3SbSe_3 [25] and Tl_9SbSe_6 [26]. No Tl–Tl distances ($< 4 \text{ \AA}$) occur in all these three thallium selenides in contrast to the shortest Tl–Tl contact of 3.54 \AA in $\text{Tl}_6\text{Si}_2\text{Te}_6$ [27].

Tl_2SnSe_3 and Tl_2SnTe_3 adopt the same structure type and the details of the crystal structures were discussed elsewhere [16,17]. Tl_2SnTe_3 crystallizes in the orthorhombic crystal system with the space group $Pnma$, and the structure contains double layers of SnTe_4 tetrahedra and TlTe_8 square antiprisms alternating with layers of Tl atoms, as shown in Figure 4.4. In both cases, the oxidation states can be assigned to be Tl^+ , Sn^{4+} and $(\text{Se/Te})^{2-}$.

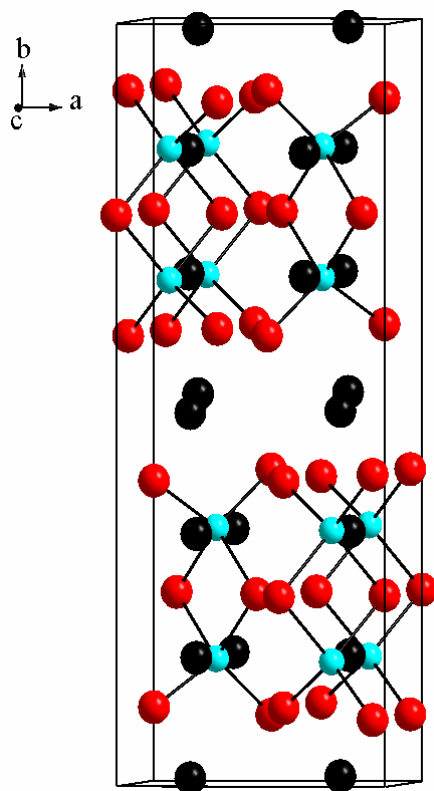


Figure 4.4 Crystal structure of Tl_2SnTe_3 . Tl: black; Sn: cyan; Te: red.

4.3 Electronic structures

4.3.1 Model descriptions

Self-consistent tight-binding first principles LMTO calculations [31] were performed for $\text{Tl}_{2.35}\text{Sb}_{8.65}\text{Se}_{14}$, Tl_2SnSe_3 , and Tl_2SnTe_3 . The electronic structure of Tl_2SnTe_5 [32], the known compound showing outstanding thermoelectric performances, was also obtained for comparison with Tl_2SnSe_3 and Tl_2SnTe_3 . Since the disorders in the crystal structure of $\text{Tl}_{2.35}\text{Sb}_{8.65}\text{Se}_{14}$ can not be directly dealt with by our LMTO program, we chose two ordered models for the calculation, both of the stoichiometry $\text{Tl}_{2.5}\text{Sb}_{8.5}\text{Se}_{14}$: the first one with one Sb5 but no Sb7 at the Tl/Sb split sites, called model I, and the second one with one Sb7 and no Sb5, called model II. Both models require a symmetry reduction from $P2_1/m$ to Pm . We analyzed the electronic structure by extracting information from the band structure and densities of states (DOS). Since there is no disorder in the structures of Tl_2SnTe_5 , Tl_2SnSe_3 , and Tl_2SnTe_3 , the structure information achieved from the database was directly used for the calculations in each case.

4.3.2 Calculation results

Both charge-balanced models with the formula $\text{Tl}_{2.5}\text{Sb}_{8.5}\text{Se}_{14}$ suggest semiconducting behaviour with a very small band gap. The actual stoichiometry from the refinement (Tl : Sb : Se = 2.35 : 8.65 : 14) is more Sb-rich, i.e. comprises more valence-electrons. In either of the two models, flat bands occur around Fermi level, suggesting low electrical conductivity and high Seebeck coefficient. Since no significant differences exist between model I and II, we show only the electronic band structure of model I for $\text{Tl}_{2.5}\text{Sb}_{8.5}\text{Se}_{14}$, together with selected

paths of the first Brillouin zone for the band structure calculation in Figure 4.5, with the Fermi level, E_F , arbitrarily placed at 0 eV.

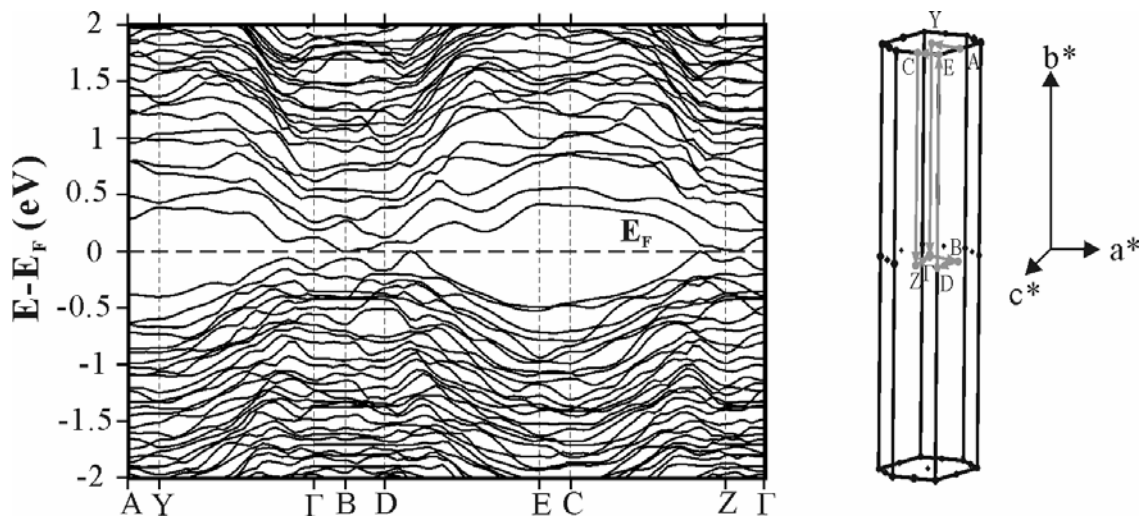


Figure 4.5 Band structure (left) of $Tl_{2.5}Sb_{8.5}Se_{14}$ and its first Brillouin zone (right).

The computed DOS including the partial projections onto the Tl and Sb orbitals of model I are shown in Figure 4.6.

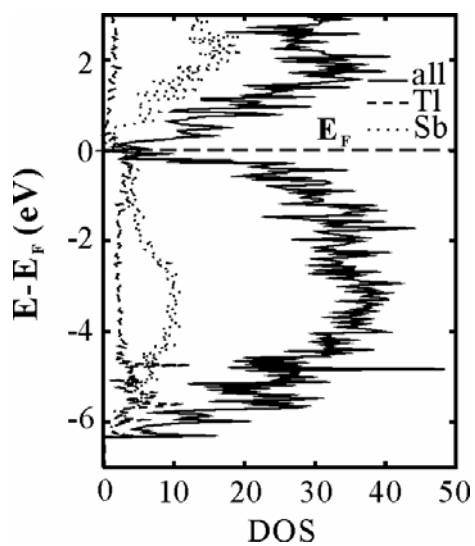


Figure 4.6 Computed densities of states of $Tl_{2.5}Sb_{8.5}Se_{14}$.

Outside of the chosen energy window below -7 eV are the filled Tl-6s and Sb-5s and Se-4s states. The DOS are dominated by Se-4p orbitals between -6.2 eV and E_F . The conduction band above the Fermi level comprises mainly Tl-6p orbitals.

DOS of these three compounds are shown in Figure 4.7. The densities of states are dominated by Se-4p orbitals for Tl_2SnSe_3 between -5.5 eV and E_F , while Te-5p for Tl_2SnTe_3 and Tl_2SnTe_5 . The conduction band above the Fermi level comprises mainly Tl-6p orbitals for all cases.

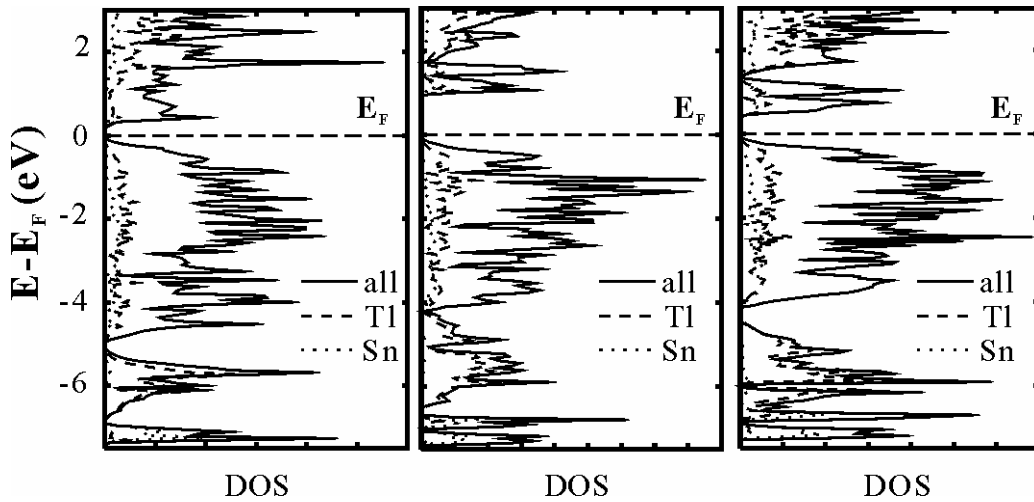


Figure 4.7 Computed densities of states of Tl_2SnTe_5 (left), Tl_2SnSe_3 (middle), and Tl_2SnTe_3 (right).

Tl_2SnSe_3 shows the largest band gap of around 0.9 eV among these three compounds. Because Te is less electronegative than Se, its p -states occur at higher energy level, i.e. closer to the empty Sn-5s states. Tl_2SnTe_5 has a smaller band gap around 0.2 eV compared with 0.4 eV of Tl_2SnTe_3 , which was further indicated by the higher electrical conductivity of Tl_2SnTe_5 .

4.4 Physical property measurements

4.4.1 $\text{Tl}_{2.35}\text{Sb}_{8.65}\text{Se}_{14}$, $\text{Tl}_{1.93}\text{Sb}_{8.07}\text{Se}_{13}$, and $\text{Tl}_{2.04}\text{Bi}_{7.96}\text{Se}_{13}$

The electronic structure calculations indicate semiconducting behaviour for $\text{Tl}_{2.35}\text{Sb}_{8.65}\text{Se}_{14}$. This is confirmed by the infrared diffuse reflectance measurement. The spectrum was recorded in an extended region of 8000 to 800 cm^{-1} at room temperature with a VERTEX 70 Fourier Transform Infrared Spectrometer from Bruker Optics Ltd. Absorption data (k/S) were calculated from the reflectance data using the Kubelka-Munk function [33]: $k/S = (1 - R)^2/2R$, where k is the molar absorption coefficient, S is the scattering coefficient, and R is the absolute reflectance of the sample at a given wavenumber. The band gap was determined from the intersection of the extended baseline and the tangent of the absorption increase to be 0.6 eV (Figure 4.8).

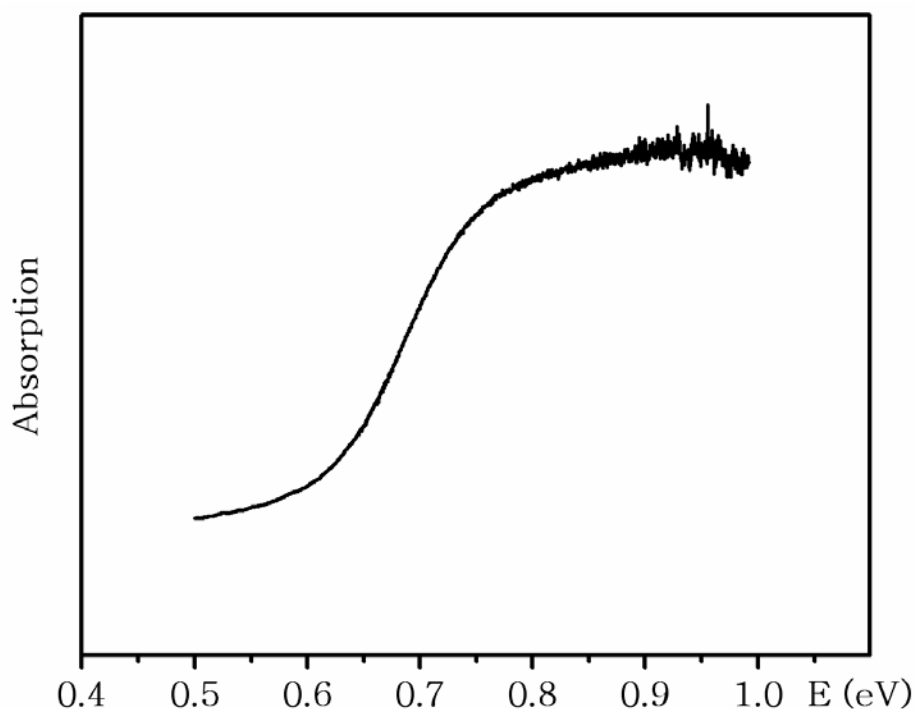


Figure 4.8 Infrared diffuse reflectance spectrum of $\text{Tl}_{2.35}\text{Sb}_{8.65}\text{Se}_{14}$.

In the case of the K analogue, $\text{K}_{2.5}\text{Sb}_{8.5}\text{Se}_{14}$, the band gap was found to be 0.8 eV [19]. The smaller gap of the Tl selenide is likely a consequence of the higher electronegativity of Tl, compared to K, leading to more covalent character for $\text{Tl}_{2.35}\text{Sb}_{8.65}\text{Se}_{14}$. That the LMTO calculation pointed towards a much smaller gap, may have been caused by the calculation method underestimating the band gap [34], and the actual disorder having only been approximated.

The electrical conductivity of $\text{Tl}_{2.35}\text{Sb}_{8.65}\text{Se}_{14}$ and $\text{Tl}_{1.93}\text{Sb}_{8.07}\text{Se}_{13}$ was measured on cold-pressed pellets with the dimension of $6 \times 1 \times 1 \text{ mm}^3$. As is typical for semiconductors, the electrical conductivity increases exponentially with increasing temperature in both cases, namely from $\sigma = 1.4 \times 10^{-6} \Omega^{-1}\text{cm}^{-1}$ at 205 K to $\sigma = 5.8 \times 10^{-4} \Omega^{-1}\text{cm}^{-1}$ at 310 K for $\text{Tl}_{2.35}\text{Sb}_{8.65}\text{Se}_{14}$ (Figure 4.9) and from $4.4 \times 10^{-4} \Omega^{-1}\text{cm}^{-1}$ at 170 K to $\sigma = 4.3 \times 10^{-2} \Omega^{-1}\text{cm}^{-1}$ for $\text{Tl}_{1.93}\text{Sb}_{8.07}\text{Se}_{14}$ (Figure 4.10).

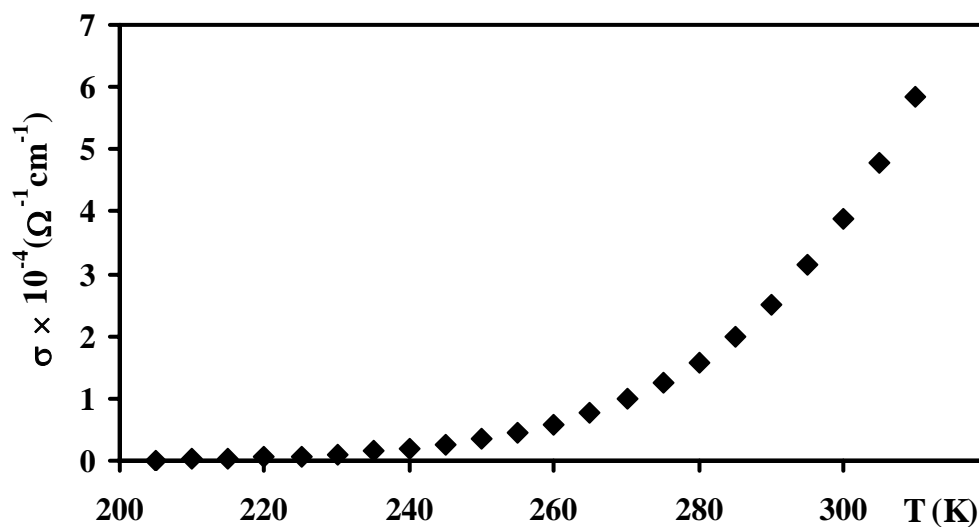


Figure 4.9 Electrical conductivity of $\text{Tl}_{2.35}\text{Sb}_{8.65}\text{Se}_{14}$.

Because of the strong temperature dependence combined with the low conductivity at room temperature, the current and hence the conductivity of the sample could not be determined below 205 K for $\text{Tl}_{2.35}\text{Sb}_{8.65}\text{Se}_{14}$ and 170 K for $\text{Tl}_{1.93}\text{Sb}_{8.07}\text{Se}_{13}$. For comparison, the room-temperature electrical conductivity value of TlSbSe_2 [24] was reported to be $1.0 \times 10^{-4} \Omega^{-1}\text{cm}^{-1}$.

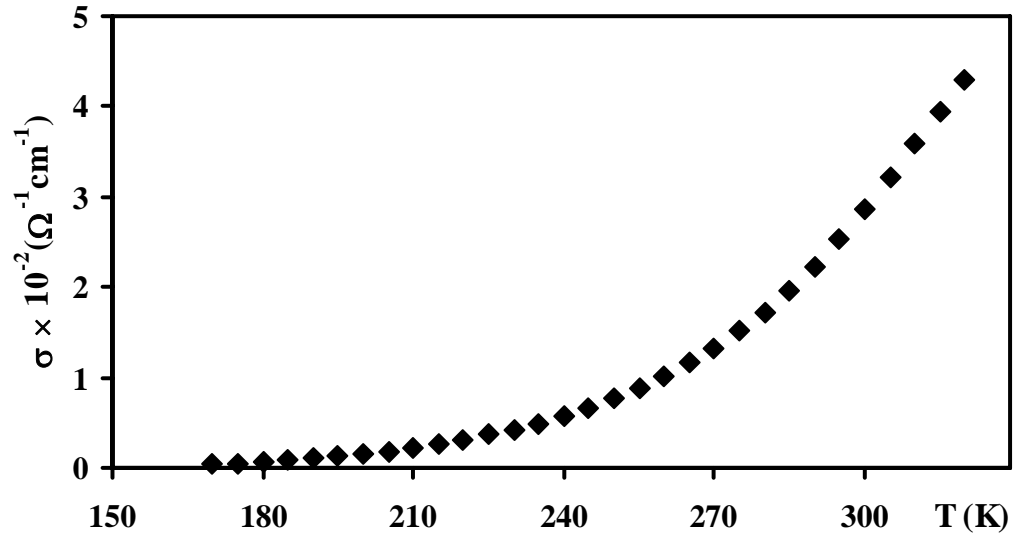


Figure 4.10 Electrical conductivity of $\text{Tl}_{1.93}\text{Sb}_{8.07}\text{Se}_{13}$.

Since I was unable to achieve the required large amount of phase pure samples for $\text{Tl}_{2.04}\text{Bi}_{7.96}\text{Se}_{13}$, the electrical conductivity of $\text{Tl}_{2.04}\text{Bi}_{7.96}\text{Se}_{13}$ was measured on a long needle crystal with dimensional of $4 \times 0.02 \times 0.01 \text{ mm}^3$. The high internal resistance of the needle crystal (above $20 \text{ M}\Omega$, resulting the $\rho > 100 \Omega\text{cm}$), prevented the measurement.

For intrinsic semiconductors, Arrhenius' Law for thermally activated conduction applies: $\ln\sigma/\sigma_0 = \exp(-\Delta_A/k_B T)$, with $\Delta_A = \frac{1}{2} E_{\text{gap}}$ [35]. The plot of $\ln(\sigma)$ versus $1/T$ resulting in a linear curve with a slope of $-\frac{1}{2} E_{\text{gap}}/k_B$ is shown in the right part of Figure 4.11 and 4.12.

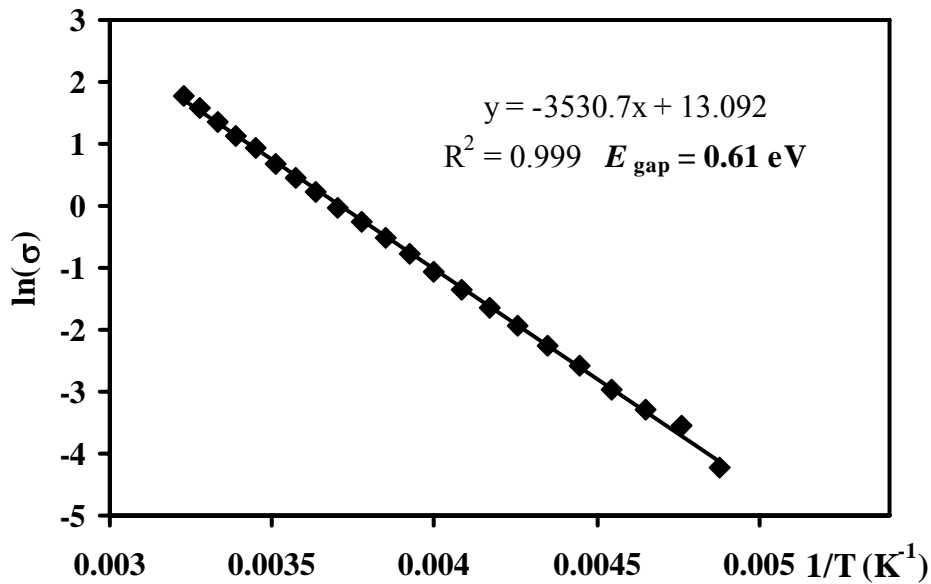


Figure 4.11 Plot of $\ln(\sigma)$ versus $1/T$ for $\text{Tl}_{2.35}\text{Sb}_{8.65}\text{Se}_{14}$.

A linear curve was obtained over the whole temperature range from 205 K to 310 K for $\text{Tl}_{2.35}\text{Sb}_{8.65}\text{Se}_{14}$ with a regression coefficient of $R^2 = 0.999$ and $E_{\text{gap}} = 0.6$ eV, in accord with the result of the experimental gap determination via IR spectroscopy; while a linear curve can only be extracted from 210 K to 275 K for $\text{Tl}_{1.93}\text{Sb}_{8.07}\text{Se}_{14}$ with a regression coefficient of $R^2 = 0.999$ and $E_{\text{gap}} = 0.3$ eV, which is smaller than that of $\text{Tl}_{2.35}\text{Sb}_{8.65}\text{Se}_{14}$ resulting in the higher conductivity.

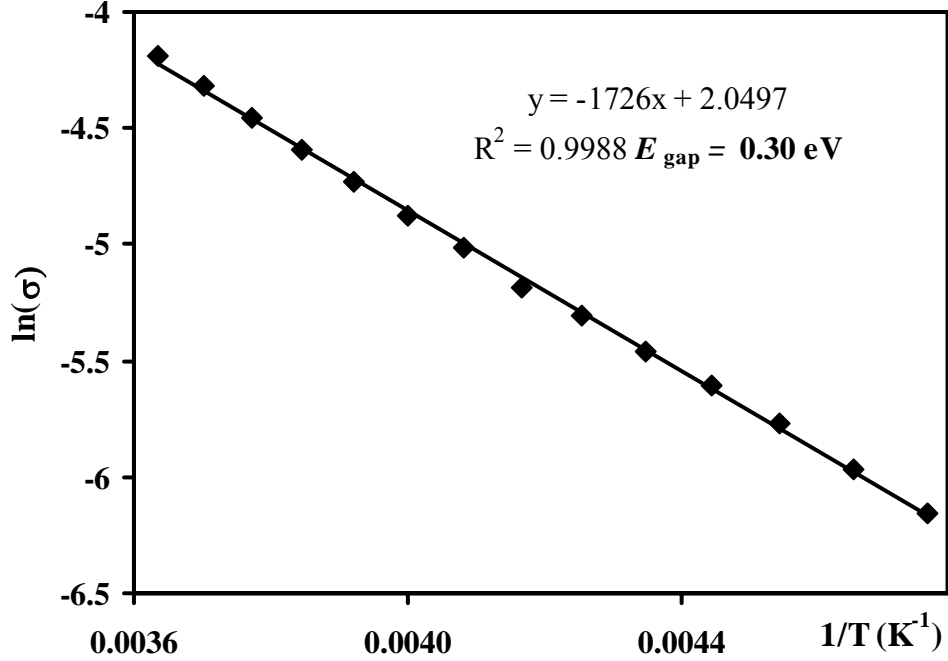


Figure 4.12 Plot of $\ln(\sigma)$ versus $1/T$ for $\text{Tl}_{1.93}\text{Sb}_{8.07}\text{Se}_{13}$.

The Seebeck coefficient (S) measurement of $\text{Tl}_{2.35}\text{Sb}_{8.65}\text{Se}_{14}$ and $\text{Tl}_{1.93}\text{Sb}_{8.07}\text{Se}_{13}$ (Figure 4.13 and 4.14) reveals that the charge carriers of $\text{Tl}_{2.35}\text{Sb}_{8.65}\text{Se}_{14}$ are predominantly n -type, while $\text{Tl}_{1.93}\text{Sb}_{8.07}\text{Se}_{13}$ contains p -type charge carriers. As for $\text{Tl}_{2.35}\text{Sb}_{8.65}\text{Se}_{14}$, the material is slightly electron-rich because of the Sb excess, compared with the charge balanced formula $\text{Tl}_{2.5}\text{Sb}_{8.5}\text{Se}_{14}$. Between 300 K and 550 K, the Seebeck coefficient of $\text{Tl}_{2.35}\text{Sb}_{8.65}\text{Se}_{14}$ increases from $-450 \mu\text{VK}^{-1}$ at 300 K to a maximum of $-760 \mu\text{VK}^{-1}$ at 430 K. Similarly, Seebeck coefficient of $\text{Tl}_{1.93}\text{Sb}_{8.07}\text{Se}_{13}$ increases slight from $400 \mu\text{VK}^{-1}$ at 300 K to the maximum of $530 \mu\text{VK}^{-1}$ at 445 K. For comparison, the isostructural $\text{K}_{2.5}\text{Bi}_{8.5}\text{Se}_{14}$ [17] was reported to be an n -type semiconductor with a Seebeck coefficient of $-100 \mu\text{VK}^{-1}$ at room temperature.

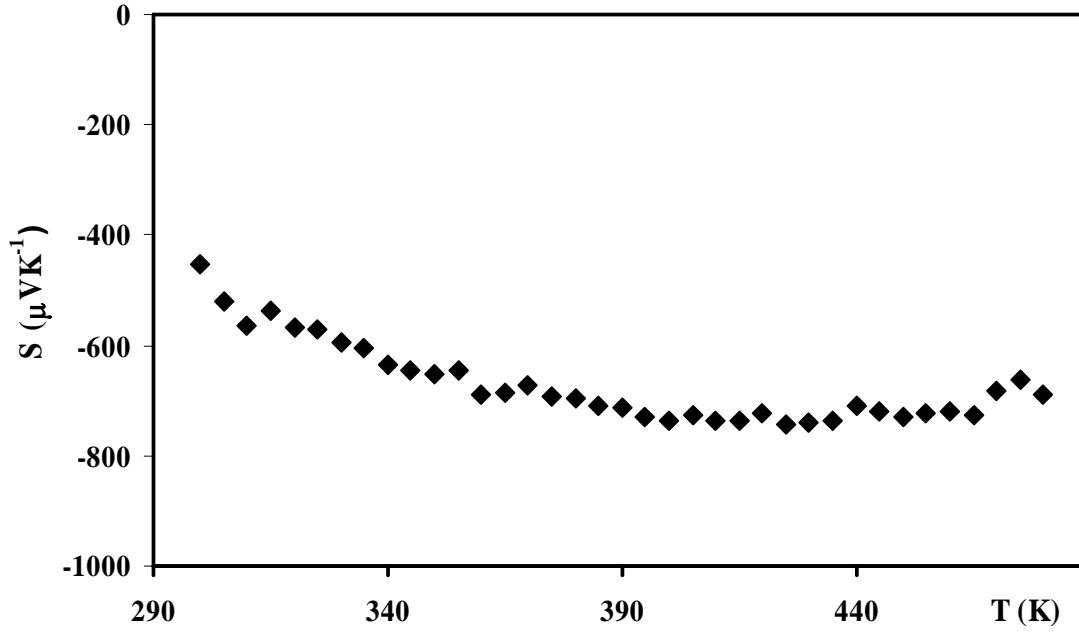


Figure 4.13 Seebeck coefficient of $\text{Tl}_{2.35}\text{Sb}_{8.65}\text{Se}_{14}$.

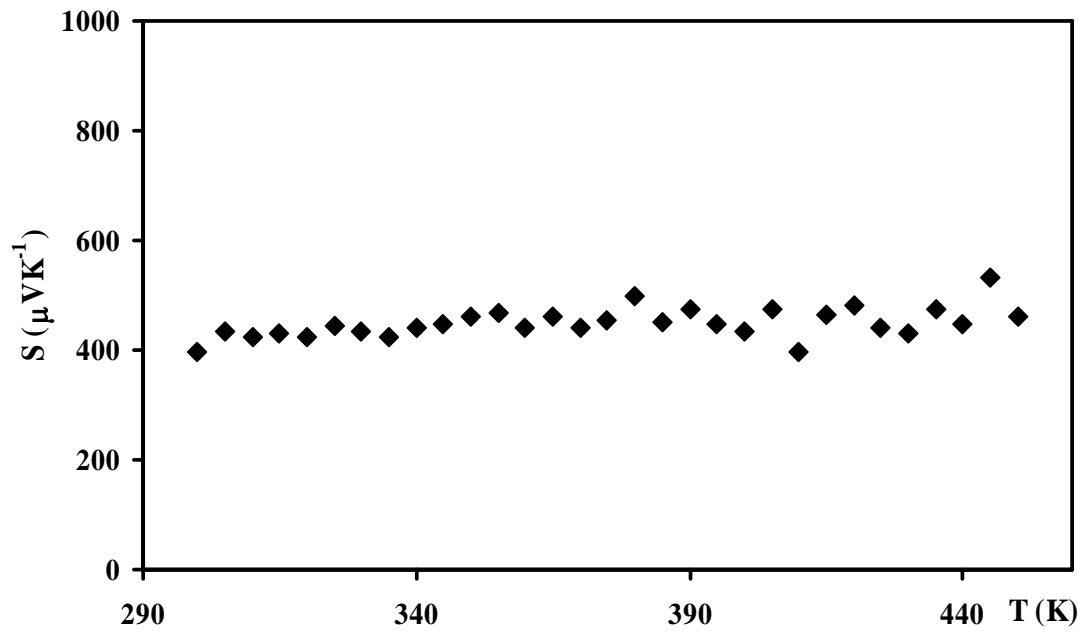


Figure 4.14 Seebeck coefficient of $\text{Tl}_{1.93}\text{Sb}_{8.07}\text{Se}_{13}$.

4.4.2 Tl_2SnSe_3 and Tl_2SnTe_3

The electrical conductivity of Tl_2SnSe_3 and Tl_2SnTe_3 were measured on the cold-pressed pellets as well. As for Tl_2SnSe_3 , the electrical conductivity increases from $1.1 \times 10^{-7} \Omega^{-1}\text{cm}^{-1}$ at 230 K to $\sigma = 5.4 \times 10^{-5} \Omega^{-1}\text{cm}^{-1}$ at 320 K (Figure 4.13). The E_{gap} (0.84 eV) extracted from the Arrhenius' Law as shown in Figure 4.14, is quite comparable with the one obtained from the LMTO calculation (0.9 eV).

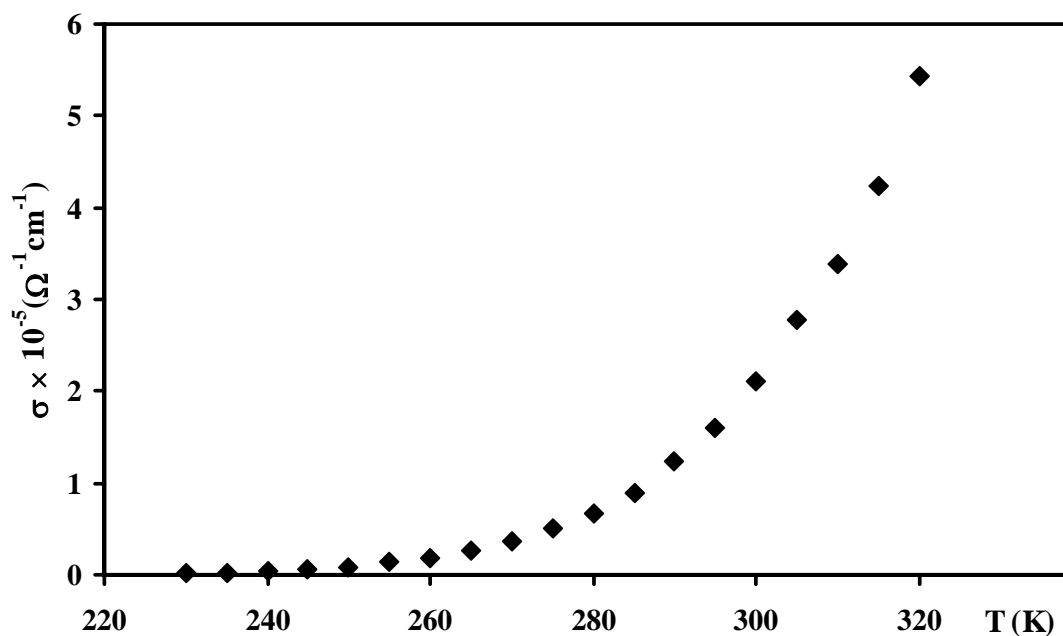


Figure 4.15 Electrical conductivity of Tl_2SnSe_3 .

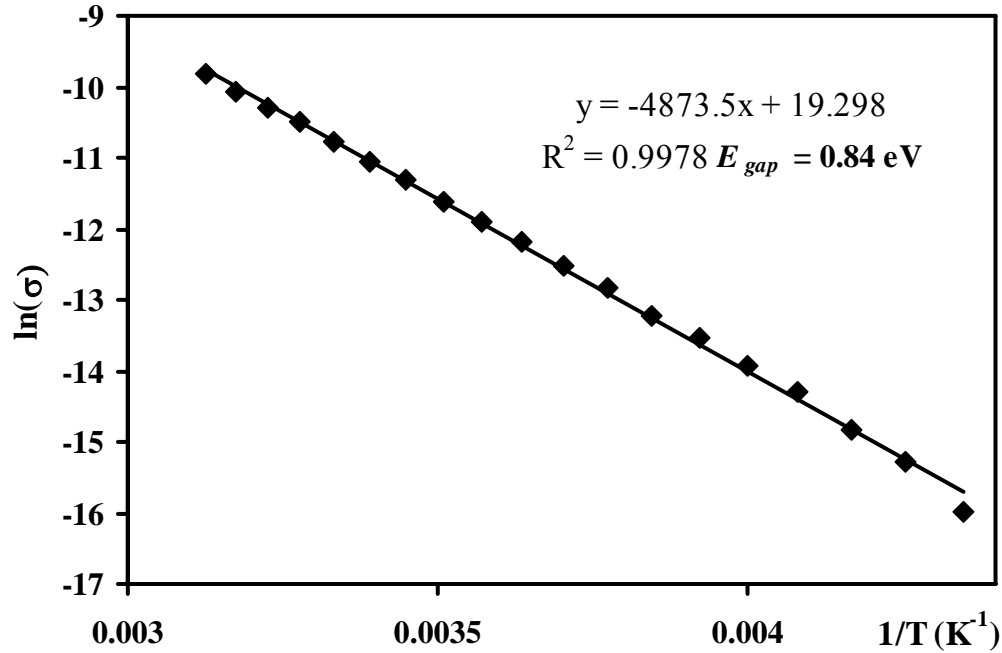


Figure 4.16 Plot of $\ln(\sigma)$ versus $1/T$ for Tl_2SnSe_3 .

On the other hand, Tl_2SnTe_3 is much more conductive than Tl_2SnSe_3 with the electrical conductivity of $20 \Omega^{-1}\text{cm}^{-1}$ at 300 K, as expected from its smaller calculated band gap (Figure 4.17). The existence of significant grain boundaries from the cold-pressed pellet might cause the conductivity of Tl_2SnTe_3 to be measured much smaller than it should be. The optimized transport property measurements based on the hot-pressed pellet of powdery samples are in progress. Furthermore, the Seebeck coefficient measurement (Figure 4.18) shows the high Seebeck coefficient of $105 \mu\text{VK}^{-1}$ at room temperature, which increases with the increasing of the temperature until the maximum $150 \mu\text{VK}^{-1}$ at 395 K is reached. However, the Seebeck coefficient starts to drop dramatically at 450 K until negative values are attended, which could be caused by the phase changes of Tl_2SnTe_3 at moderate temperatures [36].

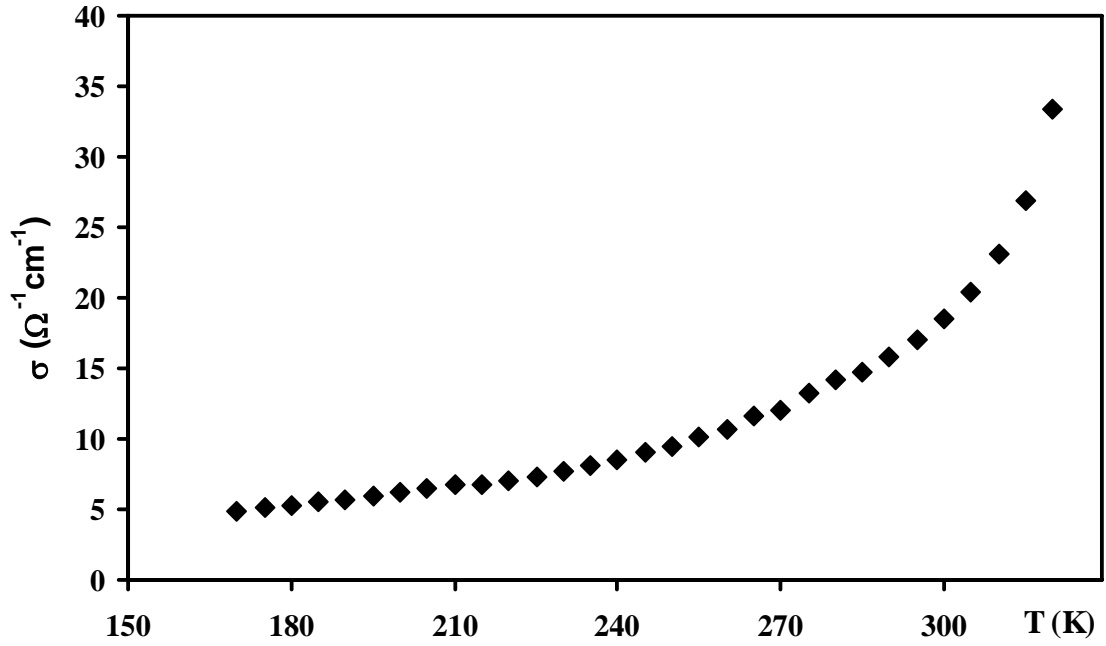


Figure 4.17 Electrical conductivity of Tl_2SnTe_3

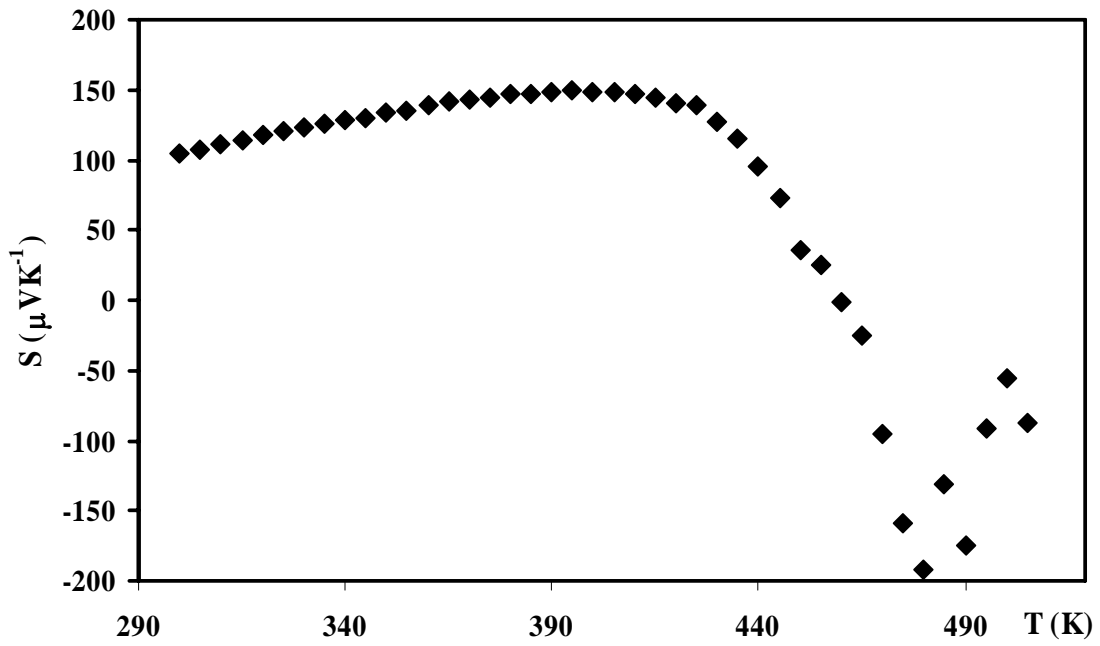


Figure 4.18 Seebeck coefficient of Tl_2SnTe_3 .

4.5 Conclusion

The new selenides, $\text{Tl}_{2.35}\text{Sb}_{8.65}\text{Se}_{14}$, $\text{Tl}_{1.93}\text{Sb}_{8.07}\text{Se}_{13}$ and $\text{Tl}_{2.04}\text{Bi}_{7.96}\text{Se}_{13}$ have been synthesized by solid state reactions and characterized by several experimental methods. The structures, similar with their potassium analogues, are composed of different (Sb/Bi) Se_6 networks and distorted Tl-Se polyhedra. $\text{Tl}_{2.35}\text{Sb}_{8.65}\text{Se}_{14}$ contains mixed occupancies of Tl and Sb atoms at two cation sites, while $\text{Tl}_{1.93}\text{Sb}_{8.07}\text{Se}_{13}$ and $\text{Tl}_{2.04}\text{Bi}_{7.96}\text{Se}_{13}$ contain mixed occupied positions at all three cation sites. No disorder was found at the Se sites within the structure of thallium selenides, while it occurs in their potassium analogues. Physical property measurements revealed that two new thallium antimony selenides are both semiconductors with electrical conductivities of $3.9 \times 10^{-4} \Omega^{-1}\text{cm}^{-1}$ and $1.4 \times 10^{-6} \Omega^{-1}\text{cm}^{-1}$, and Seebeck coefficients of $-450 \mu\text{VK}^{-1}$ and $400 \mu\text{VK}^{-1}$ at the room temperature for $\text{Tl}_{2.35}\text{Sb}_{8.65}\text{Se}_{14}$ and $\text{Tl}_{1.93}\text{Sb}_{8.07}\text{Se}_{13}$, respectively. Although the Seebeck coefficient of both compounds is high enough for thermoelectrics, the electrical conductivity is too low for a competitive thermoelectric material. Hence no further optimization was attempted.

Furthermore, the electronic structures and thermoelectric properties of two known compounds, Tl_2SnSe_3 and Tl_2SnTe_3 , have been studied. Both of the compounds were predicted to be the semiconductors with the band gap of 0.9 eV for Tl_2SnSe_3 and 0.4 eV for Tl_2SnTe_3 by our calculations, which were then confirmed by physical property measurements. Tl_2SnTe_3 stands out to be promising for the thermoelectric applications with the electrical conductivity of $20 \Omega^{-1}\text{cm}^{-1}$ and Seebeck coefficient of $105 \mu\text{VK}^{-1}$ at 300 K based on the cold-pressed pellets. Further optimizations for Tl_2SnTe_3 , like doping and hot-pressing, will be attempted in order to get better thermoelectric performances.

References

- [1] Tritt, T. M. *Science* **1995**, 272, 1276-1277.
- [2] Rowe, D. M. *CRC Handbook of Thermoelectrics*; CRC Press: Boca Raton, FL, 1995.
- [3] DiSalvo, F. J. *Science* **1999**, 285, 703-706.
- [4] Tritt, T. M. *Science* **1999**, 283, 804-805.
- [5] Sharp, J. W.; Sales, B. C.; Mandrus, D. G.; Chakoumakos, B. C. *Appl. Phys. Lett.* **1999**, 74, 3794-3796.
- [6] Kurosaki, K.; Uneda, H.; Muta, H.; Yamanaka, S. *J. Alloys Compd.* **2004**, 376, 43-48.
- [7] Wolfing, B.; Kloc, C.; Teubner, J.; Bucher, E. *Phys. Rev. Lett.* **2001**, 86, 4350-4353.
- [8] Kurosaki, K.; Kosuga, A.; Yamanaka, S. *J. Alloys Compd.* **2003**, 351, 279-282.
- [9] McGuire, M. A.; Scheidemantel, T. J.; Badding, J. V.; DiSalvo, F. J. *Chem. Mater.* **2005**, 17, 6186-6191.
- [10] McGuire, M. A.; Reynolds, T. K.; DiSalvo, F. J. *Chem. Mater.* **2005**, 17, 2875-2884.
- [11] Assoud, A.; Soheilnia, N.; Kleinke, H. *Chem. Mater.* **2004**, 16, 2215-2221.
- [12] Assoud, A.; Soheilnia, N.; Kleinke, H. *J. Solid State Chem.* **2005**, 178, 1087-1093.
- [13] Assoud, A.; Soheilnia, N.; Kleinke, H. *Chem. Mater.* **2005**, 17, 4509-4513.
- [14] Soheilnia, N.; Kleinke, K. M.; Assoud, A.; Kleinke, H. *J. Mater. Chem.* **2004**, 14, 2768-2774.
- [15] Derakhshan, S.; Assoud, A.; Taylor, N. J.; Kleinke, H. *Intermet.* **2006**, 14, 198-207.
- [16] Jaulmes, S.; Houenou, P. *Mat. Res. Bull.* **1980**, 15, 911-915.
- [17] Agafonov, V.; Legendre, B.; Rodier, N.; Cense, J. M.; Dichi, E.; Kra, G. *Acta Crystallogr. C* **1991**, 39, 1300-1301.
- [18] Dichi, E.; Kra, G.; R., E. *J. Alloys Compd.* **1993**, 194, 147-154.
- [19] Chung, D. Y.; Choi, K. S.; Iordanidis, L.; Schindler, J. L.; Brazis, P. W.; Kannewurf, C. R.; Chen, B.; S., H.; Uher, C.; Kanatzidis, M. G. *Chem. Mater.* **1997**, 9, 3060-3071.
- [20] Sheldrick, G. M. *SHELXTL*; Version 5.12 ed.; Siemens Analytical X-Ray Systems: Madison, WI., 1995.
- [21] Wacker, K.; Buck, P. *Mat. Res. Bull.* **1980**, 15, 1105-1111.
- [22] Olsen, A.; Goodman, P.; Whitfield, H. J. *J. Solid State Chem.* **1985**, 60, 305-315.
- [23] Wacker, K. *Z. Kristallogr.* **1991**, 3, 281-281.
- [24] Kolomiets, B. T.; Goryunova, N. A. *Zh. Sakha Promyshl.* **1955**, 25, 984-994.
- [25] Voroshilov, Y. V.; Gurzan, M. I.; Kish, Z. Z.; Lada, L. V. *Izvestiya Akademii Nauk SSSR, Neorganicheskie Materialy* **1988**, 24, 1479-1484.
- [26] Eulenberger, G. *Z. Naturforsch. B* **1981**, 36, 521-523.
- [27] Assoud, A.; Soheilnia, N.; Kleinke, H. *J. Solid State Chem.* **2006**, 179, 2707-2713.
- [28] Bradtmoeller, S.; Kremer, R. K.; Boettcher, P. *Z. Anorg. Allg. Chem.* **1994**, 620, 1073-1080.
- [29] Caracas, R.; Gonze, X. *Phys. Chem. Min.* **2005**, 32, 295-300.
- [30] Assoud, A.; Kleinke, K. M.; Kleinke, H. *Chem. Mater.* **2006**, 18, 1041-1046.
- [31] Skriver, H. L. *The LMTO Method*; Springer: Berlin, Germany, 1984.
- [32] Agafonov, V.; Legendre, B.; Rodier, N.; Cense, J. M.; Dichi, E.; Kra, G. *Acta Crystallogr. C* **1991**, 47, 850-852.
- [33] Tandon, S. P.; Gupta, J. P. *Phys. Stat. Solidi* **1970**, 38, 363-367.
- [34] Yanagi, H.; Inoue, S.-I.; Ueda, K.; Kawazoe, H. *J. Appl. Phys.* **2000**, 88, 4159-4163.

- [35] Kittel, C. Introduction to Solid State Physics; 7th ed.; John Wiley & Sons Inc.: New York, 1996.
- [36] Dichi, E.; Kra, G.; Eholie, R.; Legendre, B. J. Alloys Compd. 1993, 194, 147-154.

5 Electronic structure investigation of unusual Sb–Sb bonding in high temperature thermoelectric materials

5.1 Introduction

In addition to the classical TE materials Bi_2Te_3 and PbTe [1], today's known TE materials are dominated by antimonides and tellurides, including the skutterudites $A/Ln_xM_4\text{Sb}_{12}$ (A = alkaline earth, Ln = lanthanide, M = transition metal) [2-5], $\beta\text{-Zn}_4\text{Sb}_3$ [6], $\text{Yb}_{14}\text{MnSb}_{11}$ [7], $A/M_x\text{Mo}_3\text{Sb}_{5+\delta}\text{Te}_{2-\delta}$ [8-10], CsBi_4Te_6 [11], $\text{Bi}_2\text{Te}_3/\text{Sb}_2\text{Te}_3$ thin films [12], and $\text{AgPb}_m\text{SbTe}_{2+m}$ [13]. All of these tellurides are related to the NaCl structure, mostly containing edge-sharing BiTe_6 or PbTe_6 octahedra. On the other hand, crystal structures of antimonides are much more complex, all of them comprising different kinds of Sb–Sb bonds. In this chapter various structures of the thermoelectric antimonides will be compared, mainly focusing on the different Sb atom substructures. Moreover, Hf_5Sb_9 [14] with rather interesting hypervalent Sb–Sb interactions will also be introduced even though it is a metal with a small Seebeck coefficient. The electronic structures are presented for the molecular, as well as three-dimensional models.

5.2 Theoretical methodology

Three-dimensional electronic band structures were calculated via the LMTO method [15]. The crystal orbital Hamilton population (COHP) [16] curves were extracted employing the LMTO package to gain insight into the Sb–Sb bonding. The special points of the respective Brillouin zones were selected according to Bradley and Cracknell [17].

The structural parameters of β -Zn₄Sb₃ were taken from recent work of Snyder et al. [18] with a refined formula of Zn_{6.4}Sb₅ \equiv Zn_{3.83}Sb₃. The Zn sites with less than 7% occupancy were left out, and Zn1 with its occupancy of 90% was treated as fully occupied, resulting in a Zn-deficient formula, Zn₆Sb₅ \equiv Zn_{3.60}Sb₃. The LMTO calculation was performed on a grid of 417 independent k points in the first Brillouin zone.

To avoid the difficulties arising from the partly filled f and d orbitals of Yb and Mn, respectively, of Yb₁₄MnSb₁₁, we calculated the band structure of its aristotype, Ca₁₄AlSb₁₁ [19], by utilizing the LMTO method with 163 independent k points.

To model a filled skutterudite band structure, we used the parameters published for LaRu₄Sb₁₂ [20]. The LMTO method was applied for the COHP calculation (on 98 k points). The same was done for Mo₃Sb₇, which contains 20 atoms in its primitive cell, using 145 k points in the LMTO calculation. The structural data were taken from our single crystal structure determination [8]. Mo₃Sb₅Te₂ was modeled by replacing two Sb atoms with Te in the former calculation, leading to a reduction in symmetry (from space group $Im\bar{3}m$ to $I4/mmm$), as discussed before in our previous calculations [8], where we used the structural data from Kjekshus [21]. The influence of the additional cation was investigated by adding Ni atoms into all cubic voids, keeping the space group and attaining the formula

$Ni_{0.5}Mo_3Sb_5Te_2$. Last, a model for $Ni_{0.25}Mo_3Sb_5Te_2$ was analyzed as well, in space group $P4/mmm$ where half of the cubic voids are filled with Ni atoms.

The electronic structure of Hf_5Sb_9 was calculated with the LMTO method on a grid of 594 independent k points of the first Brillouin zone of the primitive cell. The structural information for the calculation was extracted from our reported single crystal structure determination [22].

Molecular orbital diagrams of the finite Sb motifs were extracted from the Gaussian03 [23] via the B3LYP method [24,25] with the 3-21G basis set [26]. The atomic positions were taken from the respective solid structures mentioned above, and the charges were assigned as 2– for each Sb atom of the linear chain of β - Zn_4Sb_3 , 7– for the Sb_3 unit of $Ca_{14}AlSb_{11}$, 4– for the Sb_4 ring of $LaRu_4Sb_{12}$, 16– for the Sb_8 unit of Hf_5Sb_9 .

5.3 Results and Discussion

5.3.1 β -Zn₄Sb₃

In 1997, β -Zn₄Sb₃ was reported to reach a high $ZT = 1.3$ at 670 K, which was related to its extraordinarily low thermal conductivity [6]. Early structure determinations of this antimonide indicated the presence of 36 Zn and 30 Sb sites per unit cell, hence a crystallographic formula of Zn₆Sb₅ (six formula units per cell). In a most recent study by Snyder et al. [18], additional Zn sites were detected with small occupancy factors between 5% and 6%, as well as a 10% deficiency on the Zn1 site, which was originally reported to be fully occupied. The additional Zn sites and the deficiency on the major Zn site contribute to the low thermal conductivity of β -Zn₄Sb₃, as do the complex crystal structures.

For clarity, the structure of β -Zn₄Sb₃ is shown excluding the additional Zn sites in Figure 5.1. The structure is comprised of a three-dimensional network of edge- and corner-sharing ZnSb₄ tetrahedra and Sb₂ pairs formed by the Sb2 atoms. The Sb–Sb bond of 2.82 Å (bold lines in Figure 1) is typical for a classical 2-electron-2-center, $2e-2c$, (single) bond, which also occurs in the infinite chains of KSb (2.83 Å and 2.85 Å) [27]. These Sb₂ pairs run along the c axis, where the distance between the pairs of 3.38 Å (dashed lines in Figure 5.1) may still correspond to a weakly bonding Sb–Sb interaction. The Sb1 atoms, on the other hand, do not participate in any Sb–Sb contacts < 4 Å.

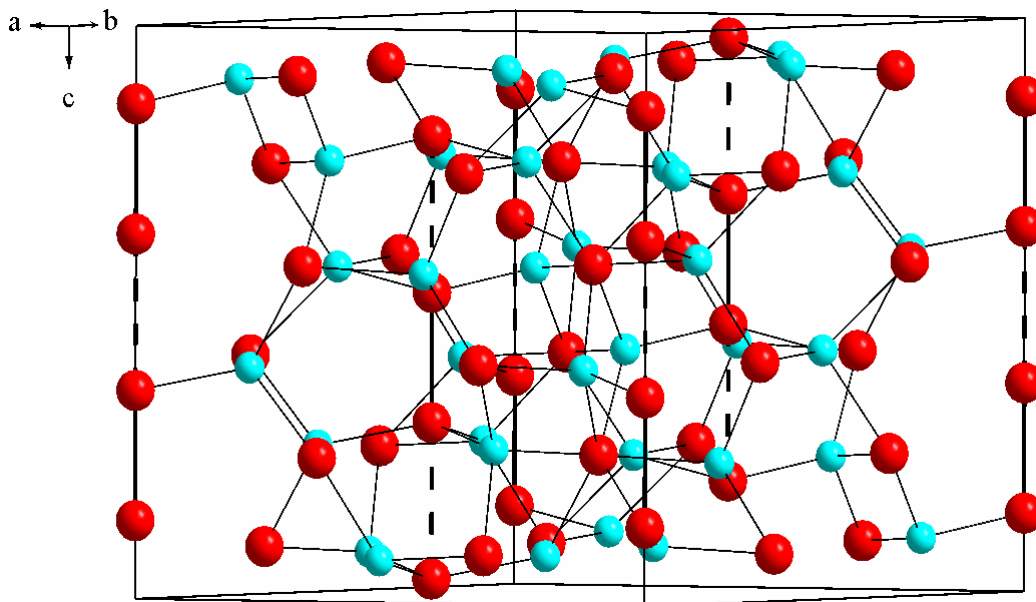


Figure 5.1 Crystal structure of β - Zn_4Sb_3 ($R\bar{3}c$). Zn: cyan; Sb: red.

Assuming that the Sb atoms reach full octet and neglecting the Sb–Sb contact of 3.38 Å, charges can easily be assigned based on the $(8 - N)$ rule [28]: main group elements exhibit $(8 - N)$ valence-electrons, v.e., with $N =$ number of single bonds. For Sb1, $N = 0$, hence v.e. = 8, and for Sb2, $N = 1$, hence v.e. = 7. Since a neutral Sb atom comprises five v.e., the charges are then 3[−] for Sb1 and 2[−] for Sb2. Therefore, the three Sb1 and two Sb2 atoms of Zn_6Sb_5 combined have $3 \times 3 + 2 \times 2 = 13$ negative charges. To achieve charge balance, 6.5 Zn^{2+} atoms are required, as in $\text{Zn}_{6.5}\text{Sb}_5 \equiv \text{Zn}_{13}\text{Sb}_{10} \equiv \text{Zn}_{3.9}\text{Sb}_3$. All physical property measurements thus far show that “ β - Zn_4Sb_3 ” is a (degenerate) *p*-type semiconductor [29], in accord with the latest structure refinements: the three formulas, $\text{Zn}_{3.83}\text{Sb}_3$, $\text{Zn}_{3.81}\text{Sb}_3$ and $\text{Zn}_{3.55}\text{Sb}_3$ are Zn deficient compared to the charged balanced formula of $\text{Zn}_{3.9}\text{Sb}_3$.

The MO diagram of the Sb_2^{4-} dumbbell (Figure 5.2) closely resembles that of the well-known isoelectronic I_2 pair. All molecular orbitals except for the strongly antibonding p_σ

combination $2\sigma_u$, formed by the p_z orbitals (lowest unoccupied molecular orbital, LUMO), are filled, resulting in a bond order of 1, as postulated above. The highest occupied molecular orbital, the HOMO $1\pi_g$, is degenerated, formed by the π antibonding combinations of the p_x and p_y orbitals.

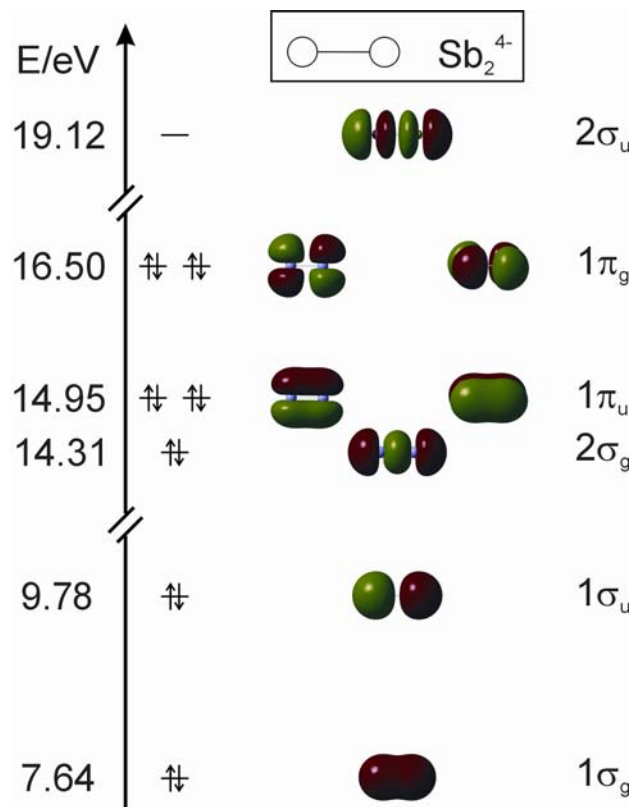


Figure 5.2 MO diagram of the Sb_2^{4-} unit of β - Zn_4Sb_3 .

To gain insight into the relevance of the 3.38 Å distance between the Sb_2^{4-} pairs, we computed the MO diagram of a linear Sb_4^{8-} unit with alternating Sb–Sb distances of 2.82 Å, 3.38 Å and 2.82 Å, respectively (Figure 5.3). The significance of the 3.38 Å interaction is reflected in the energy difference of the original $2\sigma_g$ orbitals of the Sb_2^{4-} pairs, amounting to

1.2 eV, with the bonding combination, $3\sigma_g$, occurring at 23.0 eV and the antibonding combination, $3\sigma_u$, at 24.2 eV.

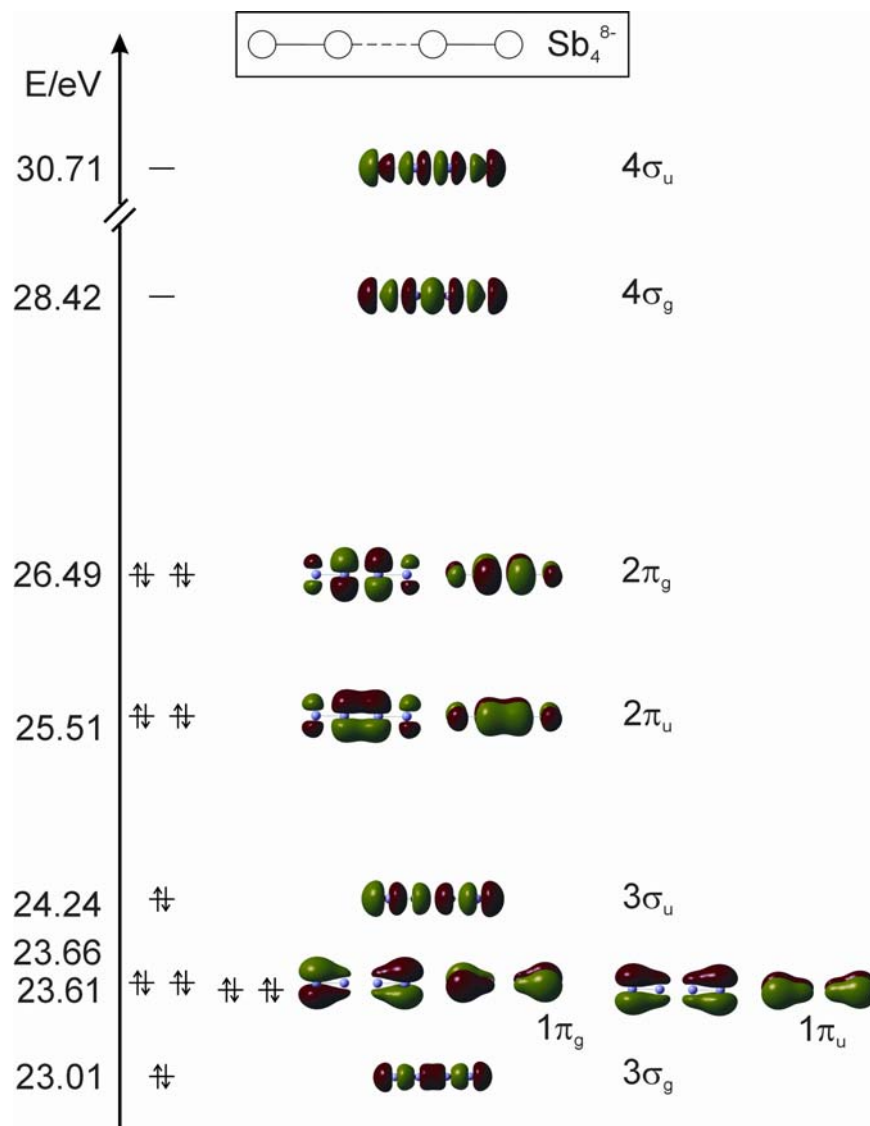


Figure 5.3 MO diagram of the Sb_4^{8-} unit of $\beta\text{-Zn}_4\text{Sb}_3$.

Similarly, the two unfilled MO's stemming from the p_σ interactions, originally $2\sigma_u$, exhibit an energy difference of 2.3 eV, occurring at 28.4 eV ($4\sigma_g$) and 30.7 eV ($4\sigma_u$). Thereby the HOMO/LUMO gap decreases from 2.6 eV in the Sb_2^{4-} unit to 1.9 eV in the

Sb_4^{8-} unit. Finally, adding another Sb_2^{4-} group to Sb_4^{8-} gives a linear Sb_6^{12-} unit with an even smaller HOMO/LUMO gap of 0.88 eV. Hence, the gap will likely be smaller in the experimentally observed infinite chain.

Related linear Sb atom chains can exhibit alternating Sb–Sb distances as short as 2.80 Å and 2.88 Å, observed in $\text{Zr}_{7.5}\text{V}_{5.5}\text{Sb}_{10}$ [30] and as long as 2.97 Å and 3.56 Å, observed in Li_2Sb [31]. The linear chains with the alternating distances all exhibit band gaps located at seven valence-electrons per Sb atom, e.g. Sb^{2-} [32,33].

The densities of states, DOS, computed via the LMTO method, confirm the assumption that Zn_6Sb_5 is electron deficient, with a narrow band gap of 0.3 eV occurring 0.45 eV above the Fermi level, E_F (left part of Figure 5.4). The existence of such a narrow gap is a major criterion for advanced thermoelectrics, as discussed before. Moreover, the DOS exhibit steep slopes around the Fermi level, E_F , a finger print for the high Seebeck coefficient. The crystal orbital Hamilton population (COHP) curves of the two different Sb–Sb interactions are shown in the right part of Figure 5.4. In contrast to the calculation on the molecular units Sb_2^{4-} and Sb_4^{8-} , only bonding states exist below E_F for the shorter interaction of 2.82 Å. This is a consequence of the strong covalent Zn–Sb bonds in the three-dimensional structure that were not included in the calculations on Sb_2^{4-} and Sb_4^{8-} units. On the other hand, the longer contact of 3.38 Å causes a sharp antibonding peak to occur directly below E_F . Correspondingly, the integrated COHP value (ICOHP) of the shorter bond is much larger, with -1.70 eV/bond compared to -0.11 eV/bond. Directly above the band gap, on the other hand, the shorter bond exhibits a steep antibonding peak, strongly contributing to the steep DOS at that point, whereas the weaker interaction is nonbonding. Hence the impact of the short Sb–Sb bond onto the band gap size is evident.

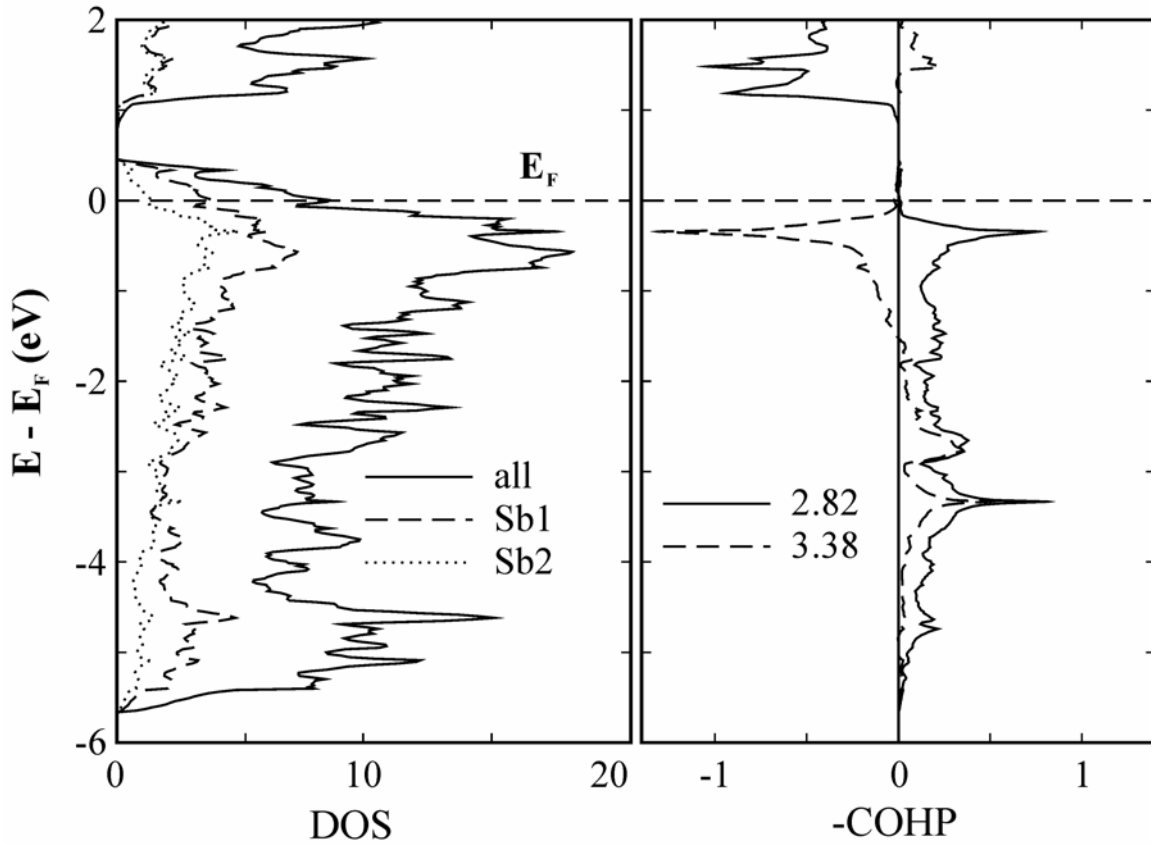


Figure 5.4 Densities of states (left) and Sb–Sb crystal orbital Hamilton populations (right) of Zn_6Sb_5 .

5.3.2 Filled skutterudites

Skutterudites, as introduced in Chapter 1, are composed of corner-sharing MQ_6 octahedra, and crystallize in a distorted variant of the ReO_3 structure type. Filled skutterudites exhibit additional atoms, e.g. lanthanide atoms, Ln , located in the large voids formed by the Q atoms [20] (Figure 5.5). With the maximum multiplicity of the Ln atoms being $\frac{1}{4}$ of the M atoms, filled skutterudites are usually written as $Ln_xM_4Q_{12}$ (with $x \leq 1$).

In 1995, a variant of CoSb_3 , namely $\text{Co}_{0.97}\text{Ir}_{0.03}\text{As}_{0.15}\text{Sb}_{2.81}\text{Te}_{0.04}$, was measured to reach $ZT = 0.6$ at 700 K [34]. Adding additional cations into the voids leads to the rattling effect, thereby to a significant decrease of the thermal conductivity [35]. The filled skutterudites were discussed as examples for Slack's phonon-glass electron-crystal (PGEC) concept [5], which implies that advanced thermoelectrics should act like a glass with respect to phonon scattering (leading to low thermal conductivity) and like a crystal with respect to the electrical transport properties (leading to high electrical conductivity).

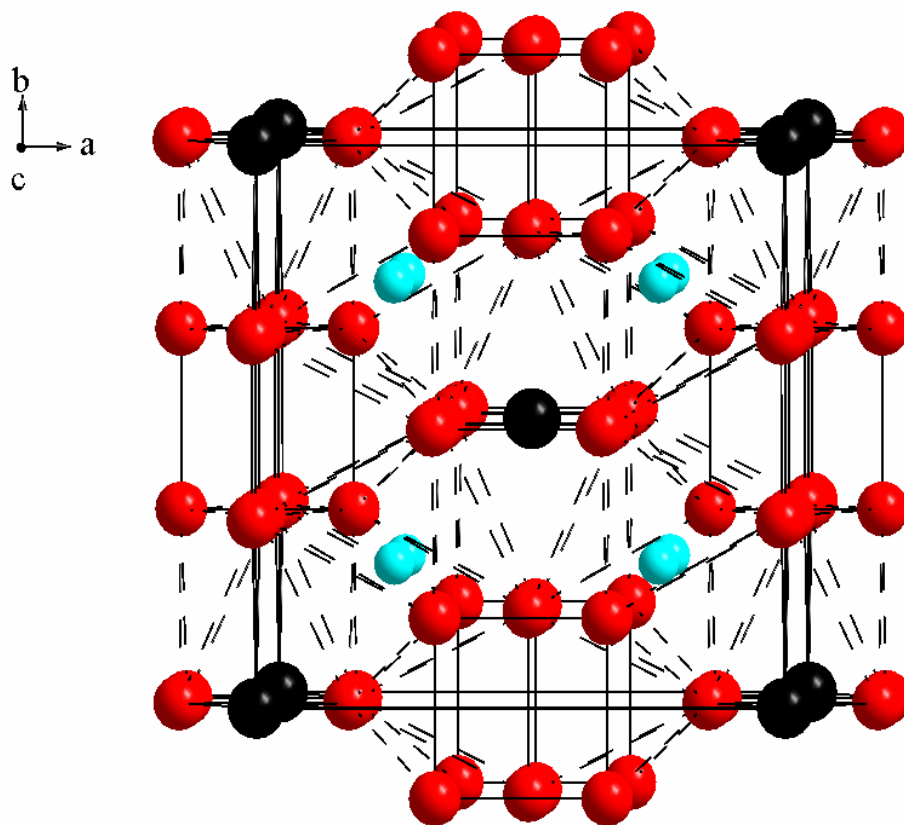


Figure 5.5 Crystal structure of $\text{LaRu}_4\text{Sb}_{12}$ ($Im\bar{3}$). La: black; Ru: cyan; Sb: red.

The Q atoms form planar, almost square rectangles, where the $Q-Q$ distances are comparable to single bonds, yet slightly elongated. These distances are 2.90 Å and 2.98 Å in

CoSb₃, and 2.80 Å and 2.92 Å in RhSb₃ [36]. Longer Sb–Sb contacts between the rectangles, for example 3.41 Å in CoSb₃ and 3.53 Å in RhSb₃, give rise to a three-dimensional Sb network. Commonly the Sb₄ ring of CoSb₃ is regarded as an Sb₄⁴⁻, because each Sb atom participates in two single Sb–Sb bonds. Hence, via the (8 – N) rule one obtains 8 – N = 8 – 2 = 6 valence-electrons, i.e. a charge of 1– per Sb atom. The MO diagram of the Sb₄⁴⁻ unit omitting the *s* orbitals, shown in Figure 5.6 with the dimensions found in LaRu₄Sb₁₂, can be understood based on two interacting Sb₂ pairs.

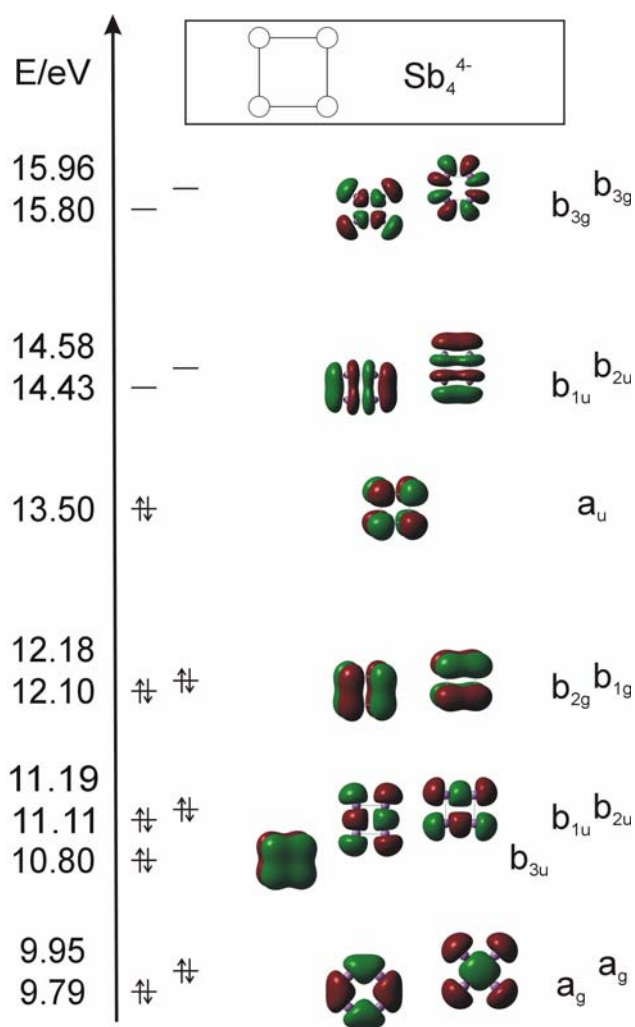


Figure 5.6 MO diagram of the Sb₄⁴⁻ unit of LaRu₄Sb₁₂.

The HOMO, a_u , is π antibonding along x and y , and the LUMO, b_{1u} , is π bonding along x and σ antibonding along y , separated from the HOMO by a gap of 0.93 eV. Because the bond along x is slightly shorter than along y (2.97 Å vs. 3.02 Å), the energy of the next unoccupied orbital, b_{2u} , π bonding along y and σ antibonding along x , is slightly higher (by 0.15 eV). With five bonding and one antibonding orbitals filled, the bond order is 1 for each Sb atom.

Several band structure calculations performed on skutterudites usually revealed a gap to occur at 24 v.e. with respect to the formula MQ_3 , e.g. realized in $CoSb_3$ [37], and correspondingly $4 \times 24 = 96$ v.e. for $Ln_xM_4Q_{12}$, e.g. realized in $LaFe_3CoSb_{12}$ and $LaRu_3RhSb_{12}$ [38-40]. This can be related to the electron precise formulas, e.g. $La^{3+}(Fe^{2+})_3Co^{3+}(Sb^-)_{12}$. Hence, undoped $LaRu_4Sb_{12}$ is metallic with its 95 v.e, as confirmed by its band structure (Figure 5.7).

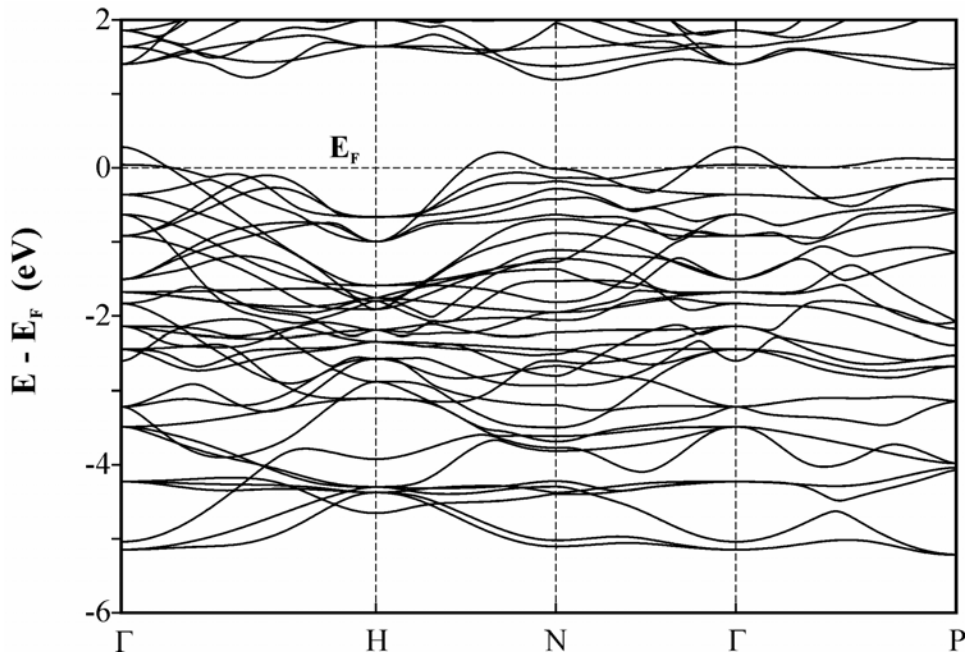


Figure 5.7 Band structure of $LaRu_4Sb_{12}$.

The gap (0.9 eV) is indirect, with the top of the valence band occurring at the Γ point, and the bottom of the conduction band, a multi valley, at the N point.

The DOS (left part of Figure 5.8) exhibit very steep regions on both sides of the band gap, pointing towards high effective masses resulting in the high Seebeck coefficient. A steep bonding peak in the Sb–Sb COHP curves (right part of Figure 5.8) occurring at the top of the valence band stems from the shorter interaction within the Sb_4 rectangle, and the antibonding peak directly at the bottom of the conduction band from the longer interaction. That the region below E_F is strongly bonding for both interactions, while the HOMO of the molecular unit Sb_4^{4-} is antibonding (π^*), is caused by the high covalent character of the Ru–Sb bonds.

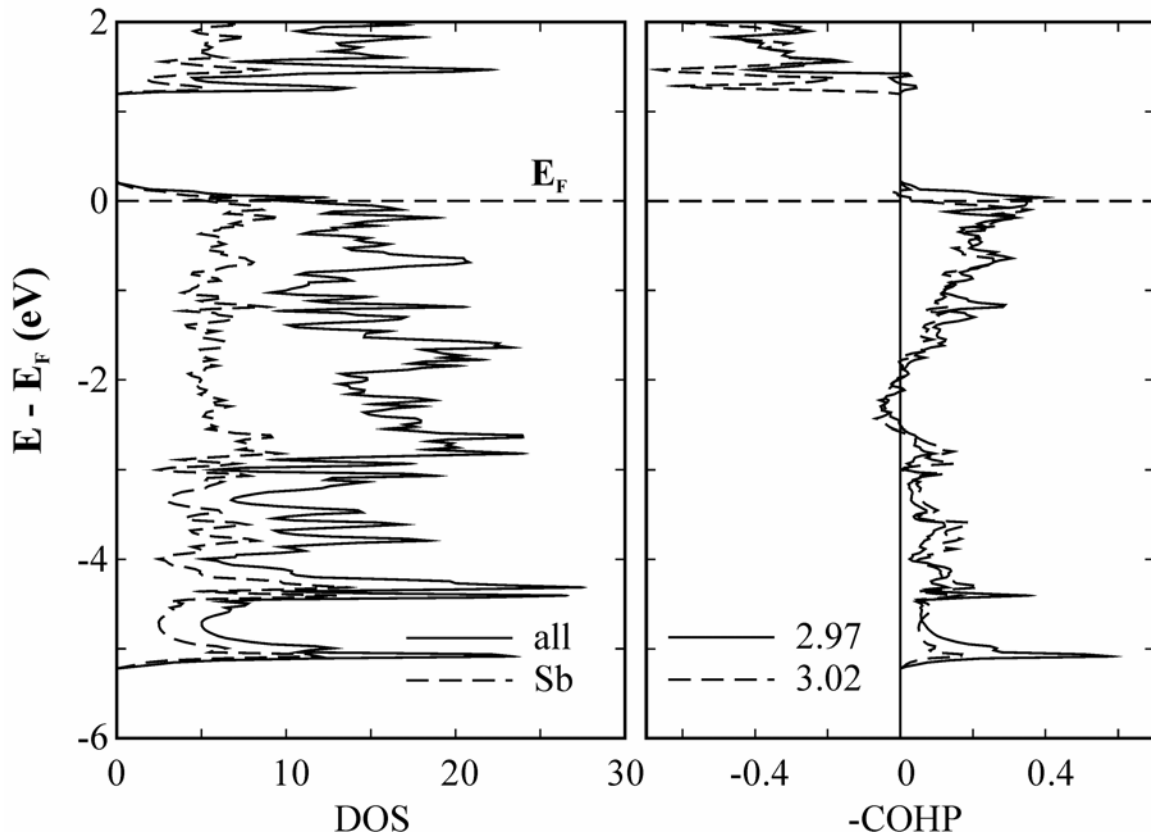


Figure 5.8 Densities of states (left) and Sb–Sb crystal orbital Hamilton populations (right) of

$\text{LaRu}_4\text{Sb}_{12}$.

Both interactions of the rectangle have similar bond strengths, reflected in ICOHP values of -0.82 eV and -0.67 eV, respectively, while the contacts between the rectangles of 3.49 Å are very weak with ICOHP = -0.06 eV per bond. That the shorter Sb–Sb interactions strongly contribute to the regions both above and below the gap reflects their importance both to the conductivity and the Seebeck coefficient of this skutterudite.

5.3.3 Yb₁₄MnSb₁₁

Very recently, *p*-type Yb₁₄MnSb₁₁ was reported to reach $ZT = 1.2$ at 1200 K, a big improvement over the Si-Ge solid solution typically used around such high temperatures [7]. The isostructural compound, Ca₁₄AlSb₁₁ [19], is comprised of isolated AlSb₄ tetrahedra and linear nonclassical Sb₃ units with equidistant Sb–Sb interactions of 3.20 Å shown in Figure 5.9.

These Sb₃ units are regarded as 7^- , i.e. isoelectronic with the more common XeF₂ and I₃[−] units, as found in CsI₃ [41] and [Ph₄As]I₃ [42]. Arguably the first MO model for these linear units was introduced in 1963 [43], based on the three *p* orbitals of XeF₂ that lie on the F-Xe-F axis, e.g. the *p_z* orbitals, while the *s* and the other *p* orbitals were treated as lone pairs. Two of the *p_z*-based MO's are filled, namely a σ bonding and a nonbonding molecular orbital, and the σ antibonding combination is unfilled. Overall a bond order of $\frac{1}{2}$ results, because only one bonding MO is available for the two bonds, explaining the unusual lengths of these linear units.

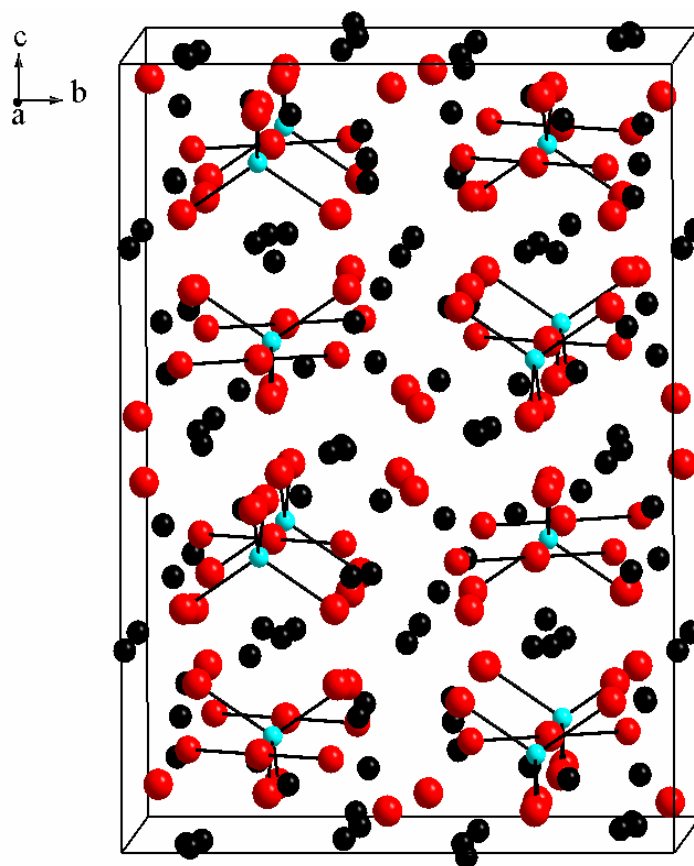


Figure 5. 9 Crystal structure of $\text{Ca}_{14}\text{AlSb}_{11}$ ($I4_1/acd$). Ca: black; Al: cyan; Sb: red.

The full MO diagram (Figure 5.10), computed using Gaussian03 for the Sb_3^{7-} fragment of $\text{Ca}_{14}\text{AlSb}_{11}$, confirms this early model in principle: the only unfilled orbital is strongly σ antibonding ($3\sigma_u$), mainly composed of the p_z orbitals, but the postulated nonbonding combination with a nodal plane in the center is actually antibonding ($3\sigma_g$), hence located above the nonbonding MO $1\pi_g$. That difference is a consequence of the s and p mixing of the MO's of σ_g symmetry. A large gap of 3.4 eV separates the HOMO, the antibonding $2\pi_u$, from the LUMO, the antibonding $3\sigma_u$.

There are numerous examples of pnictides containing P_3^{7-} , As_3^{7-} , Sb_3^{7-} and Bi_3^{7-} . However, the isolated linear triatomic chalcogen anion was not known until recently the truly linear Se_3^{4-} unit in $Ba_2Ag_4Se_5$ [44] was reported by our group.

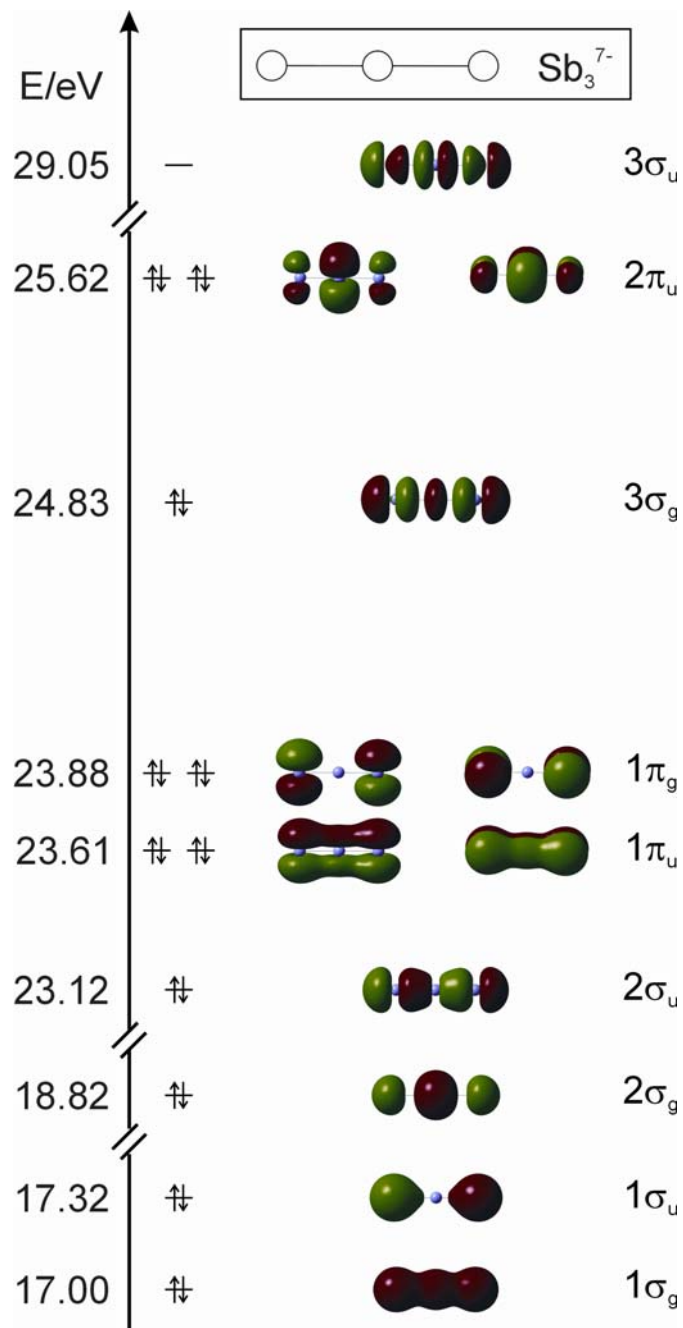


Figure 5.10 MO diagram of the Sb_3^{7-} unit of $Ca_{14}AlSb_{11}$.

The Se_3 unit in $\text{Ba}_2\text{Ag}_4\text{Se}_5$ contains longer Se–Se interactions of 2.77 Å than most of bent cases, e.g. 2.38 Å in K_2Se_3 [45] and 2.38 in Cs_2Se_3 [46], which is the similar scenario found in Sb_7^{3-} . The MO diagram computed for Se_3^{4-} by Gaussian03 is quite comparable to Sb_3^{7-} in terms of symmetry and sequences of molecular orbitals. A larger gap of 4.2 eV separates the HOMO from LUMO for the Se_3^{4-} unit, which is probably the consequence of stronger overlapping of Se atomic orbitals.

It is interesting to note that in many examples of the $\text{Ca}_{14}\text{AlSb}_{11}$ structure type, the central atom of the linear unit exhibits elongated thermal parameters along the molecular axis. Examples are $\text{Ca}_{14}\text{GaAs}_{11}$ [47] and $\text{Ca}_{14}\text{AlSb}_{11}$ [19], and split sites were refined in the cases of $\text{Ba}_{14}\text{InP}_{11}$ [48], $\text{Sr}_{14}\text{ZnSb}_{11}$ [49] and $\text{Ba}_{14}\text{MnSb}_{11}$ [50], reflected in the formation of a short bond and a longer, possibly nonbonding interaction. Such anomalies are known to lead to lower thermal conductivity, a desired feature in thermoelectrics. However, inconspicuous thermal expansion parameters were found in the thermoelectric $\text{Yb}_{14}\text{MnSb}_{11}$, as well as in $\text{Yb}_{14}\text{MnBi}_{11}$ [51], $\text{Ca}_{14}\text{MnSb}_{11}$ and $\text{Sr}_{14}\text{MnSb}_{11}$ [50].

One Sb_3^{7-} unit exists per formula unit, $\text{Ca}_{14}\text{AlSb}_{11}$. As the other Sb atoms do not participate in any Sb–Sb interactions < 4 Å, their formal charge can be assigned as 3–. This results in the electron-precise formulation $(\text{Ca}^{2+})_{14}\text{Al}^{3+}\text{Sb}_3^{7-}(\text{Sb}^{3-})_8$, so does $(\text{Yb}^{2+})_{14}\text{Mn}^{3+}\text{Sb}_3^{7-}(\text{Sb}^{3-})_8$. Hence, a band gap may occur between nonbonding Sb-*p* states and the empty Sb–Sb antibonding states of the Sb_3 units. This assumption is confirmed by the DOS (left part of Figure 5.11). More precisely, the Sb2 and Sb3 atoms, which are not part of the Sb_3 units, dominate the area below E_F (dotted line in Figure 5.11). On the other hand, the Sb1 and Sb4 atoms, forming the Sb_3^{7-} units, contribute most significantly to the steep peak directly above the gap of 0.7 eV. The COHP curve of the Sb–Sb bond of 3.20 Å confirms

that this peak is strongly antibonding, as determined for the molecular Sb_3^{7-} unit. Overall its shape is very comparable to the COHP curve of the corresponding interaction of the linear Se_3^{4-} unit of $\text{Ba}_2\text{Ag}_4\text{Se}_5$ [44]. In contrast to the Sb–Sb bonds of $\text{LaRu}_4\text{Sb}_{12}$, the contributions of the Sb–Sb bonds to the top of the valence band are negligible in case of $\text{Ca}_{14}\text{AlSb}_{11}$, but the impact onto the gap size as well as the bottom of the conduction band is evident in both cases.

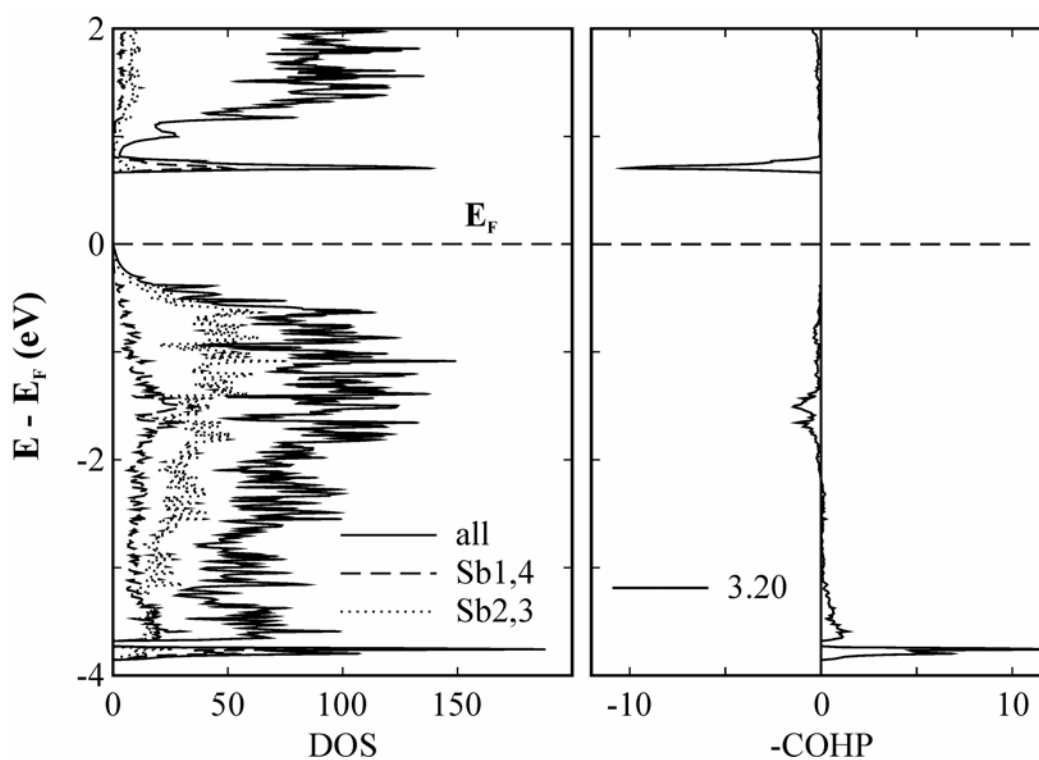


Figure 5.11 Densities of states (left) and Sb–Sb crystal orbital Hamilton populations (right) of $\text{Ca}_{14}\text{AlSb}_{11}$.

5.3.4 Mo_3Sb_7

Mo_3Sb_7 is a metal [52,53], and was therefore originally not considered for the thermoelectric energy conversion. Its potential was unveiled in 2002, when we showed that

partial Sb/Te substitution leads to semiconducting properties, and increased Seebeck coefficient [8]. *P*-type $\text{Mo}_3\text{Sb}_{5.4}\text{Te}_{1.6}$ was reported in 2007 to reach $ZT = 0.8$ at 1050 K [10], and adding small Ni atoms into the cubic voids of $\text{Mo}_3\text{Sb}_{5.4}\text{Te}_{1.6}$ occurs with an increase in the Seebeck coefficient and electrical conductivity, culminating in $ZT = 1.0$ at 1000 K [54,55].

Mo_3Sb_7 crystallizes in the cubic Ir_3Ge_7 type, space group $Im\bar{3}m$. Its structure (Figure 5.12) contains pairs of face-sharing Mo-centered square antiprisms, interconnected to infinite chains via Sb2–Sb2 bonds of 3.10 Å. The common face of each antiprism pair contains Sb1–Sb1 distances of 3.38 Å, and the Mo–Mo distance running through this face is 3.00 Å. Parallel running chains are interconnected via shorter Sb2–Sb2 bonds of 2.91 Å, and penetrate each other between the antiprisms.

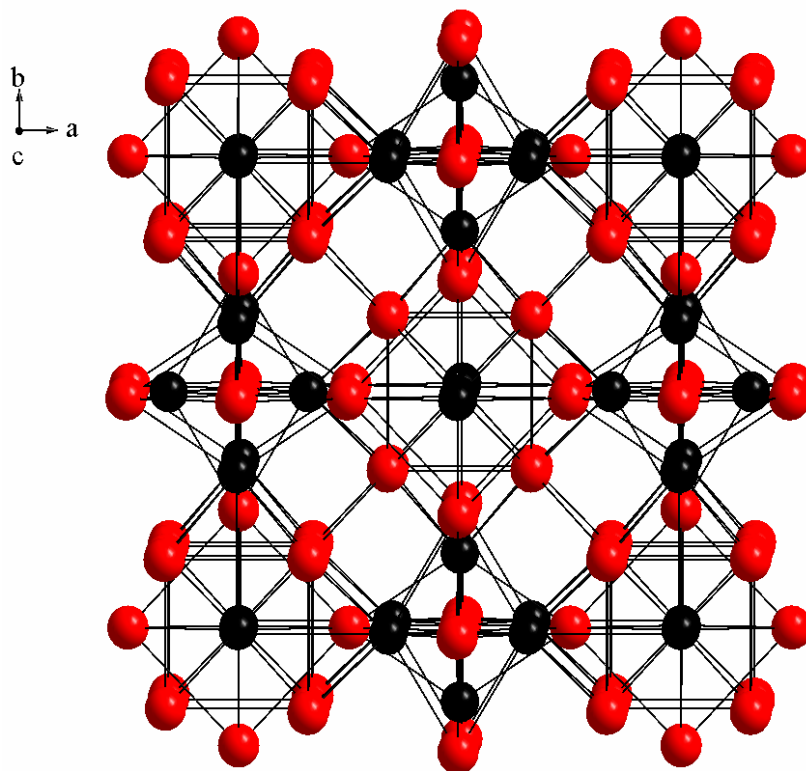


Figure 5.12 Crystal structure of Mo_3Sb_7 ($Im\bar{3}m$). Mo: black; Sb: red.

The Sb–Sb bonds between the pairs of Mo-centered antiprisms lead to the formation of empty Sb_8 cubes as shown in Figure 5.13. A three-dimensional network of Sb atoms is formed via the short Sb–Sb bond between the cubes. A similar network was also observed in the skutterudites, but the longer interactions between the rectangles there were above 3.4 Å, compared to 2.91 Å and 3.10 Å in Mo_3Sb_7 . Moreover, Mo_3Sb_7 exhibits metal–metal bonds in contrast to the skutterudites, namely the Mo–Mo bond within the pair of MoSb_8 antiprisms.

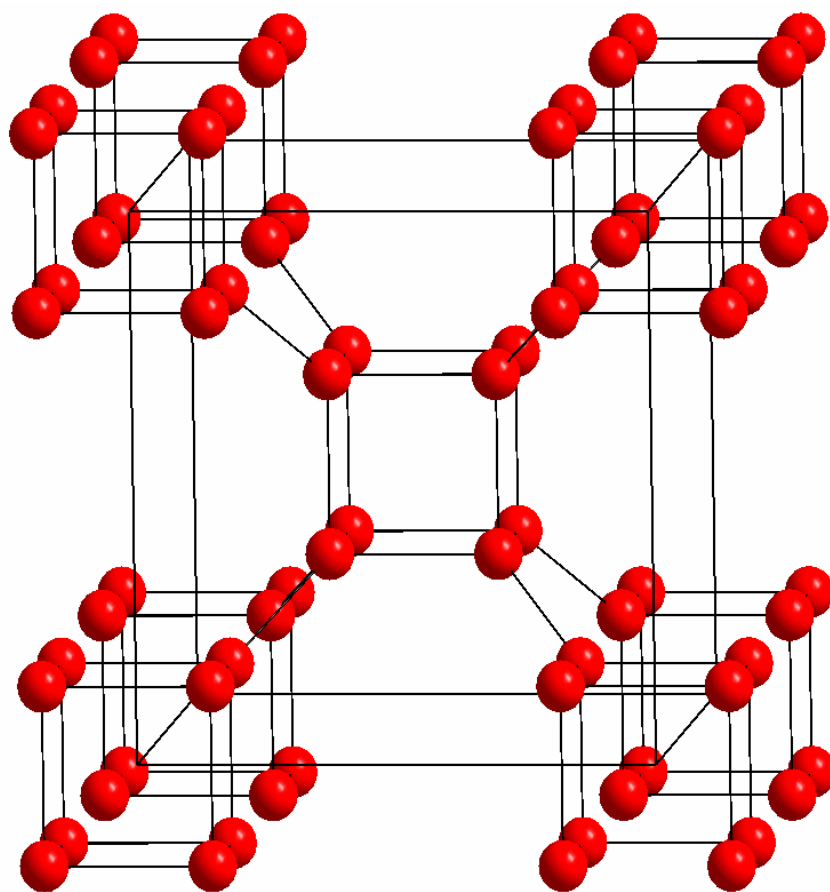


Figure 5.13 Three-dimensional network of Sb cubes of Mo_3Sb_7 .

With its 53 v.e., unsubstituted Mo_3Sb_7 is metallic, confirmed by our band structure calculation with the LMTO program packages (Figure 5.14). An indirect band of 0.7 eV gap

occurs well above E_F between the Γ and H point, while the direct gap at Γ is only slightly larger. Both the lowest unfilled and the highest filled bands have both steep and flat parts, depending on the direction within the Brillouin zone.

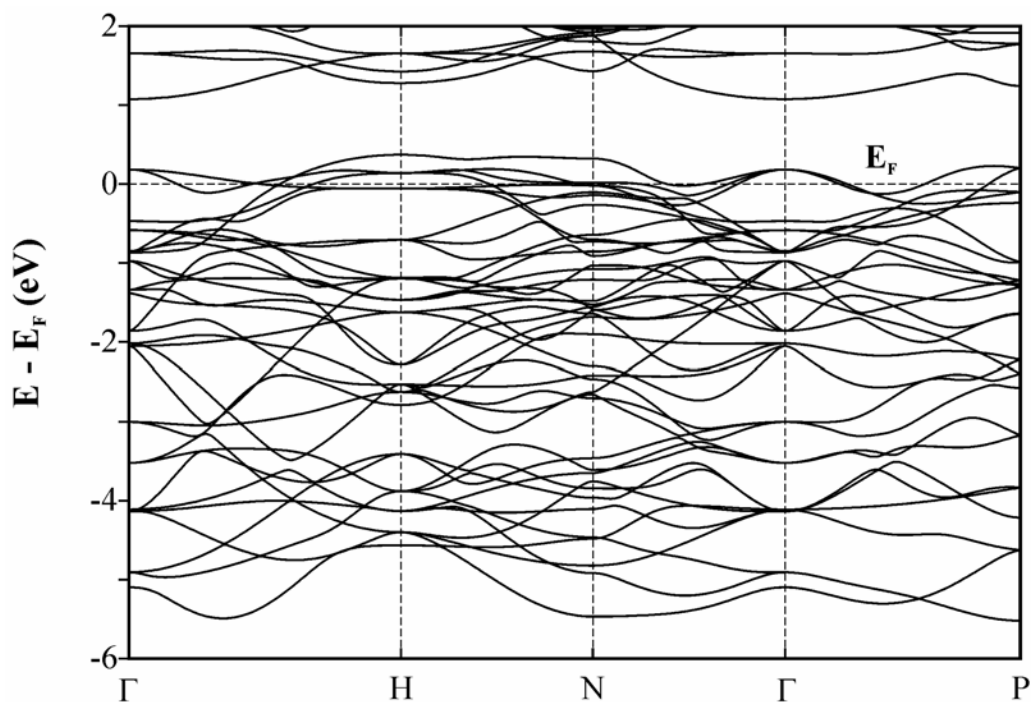


Figure 5.14 Band structure of Mo₃Sb₇.

Correspondingly, the densities of states exhibit a steep region just below the gap, and a very pronounced peak stemming from Mo-*d* orbitals, i.e. the Mo–Mo bond, slightly below E_F (left part of Figure 15). The peaks below the gap are related to the shortest Sb–Sb interaction (2.91 Å) within the structure, which is strongly bonding in the region above E_F and below the gap, to become strongly antibonding above the gap (right part of Figure 5.15). On the other hand, the longer two Sb–Sb interactions of 3.10 Å and 3.38 Å are antibonding already below the gap, but remain overall (slightly) bonding. This is reflected in negative, i.e. bonding,

ICOHP values of -0.45 eV for the 3.10 Å interaction and -0.08 eV for the 3.38 Å, compared to -0.78 eV for the shortest bond of 2.91 Å. Therefore, as is the case in $\text{LaRu}_4\text{Sb}_{12}$, a three-dimensional Sb atom network exists with a significant impact onto the regions around the band gap.

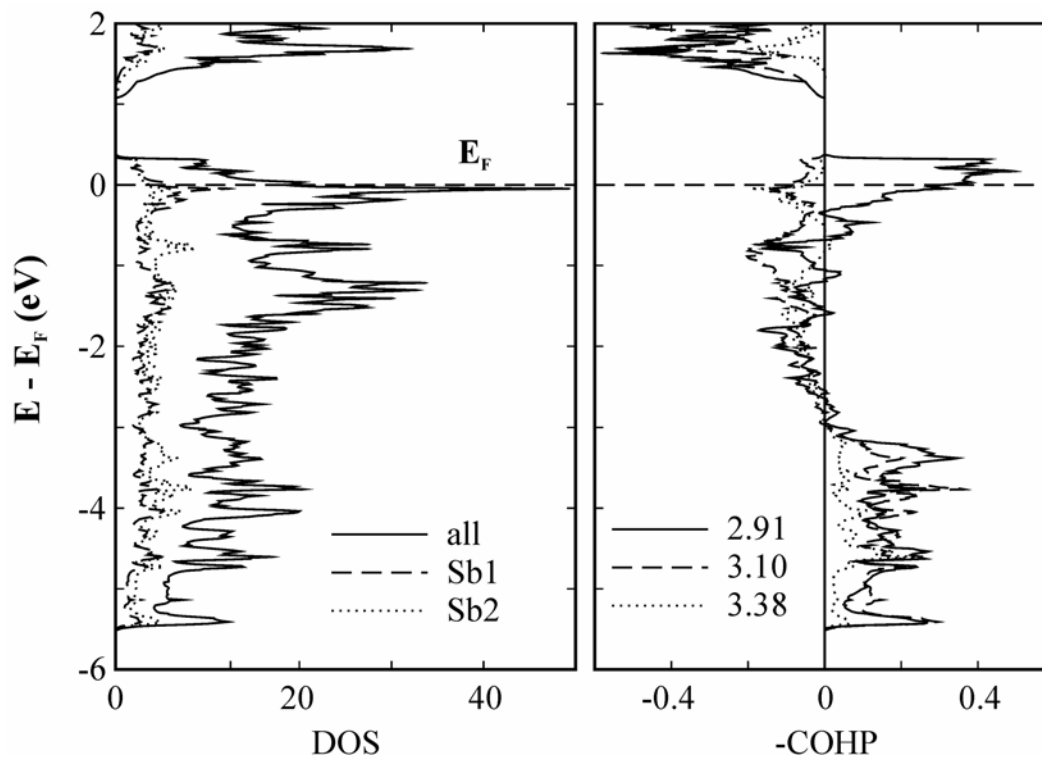


Figure 5.15 Densities of states (left) and Sb–Sb crystal orbital Hamilton populations (right) of Mo_3Sb_7 .

Partial replacements of Sb by Te atoms lead to the semiconducting material $\text{Mo}_3\text{Sb}_5\text{Te}_2$. It is assumed that Te substitutes preferentially the Sb1 site, because it is more electronegative than Sb, hence avoids the formation of Te–Te bonds. This trend was proven via neutron diffraction for the preferences of As, compared to Ge, in the isostructural Re_3GeAs_6 [56], noting that the neutron scattering lengths of Sb and Te are too similar for an analogous

investigation. Treating both the Mo–Mo bond and the Sb2–Sb2 bond of 2.91 Å as single bonds, the charges can be assigned to Mo^{5+} , Sb^{3-} , Sb^{2-} and Te^{2-} , again yielding a balanced formula: $(\text{Mo}^{5+})_3\text{Sb}^{3-}(\text{Sb}^{2-})_4(\text{Te}^{2-})_2$. The DOS computed for such a model confirm that E_F falls into the band gap of $\text{Mo}_3\text{Sb}_5\text{Te}_2$ (left part of Figure 5.16).

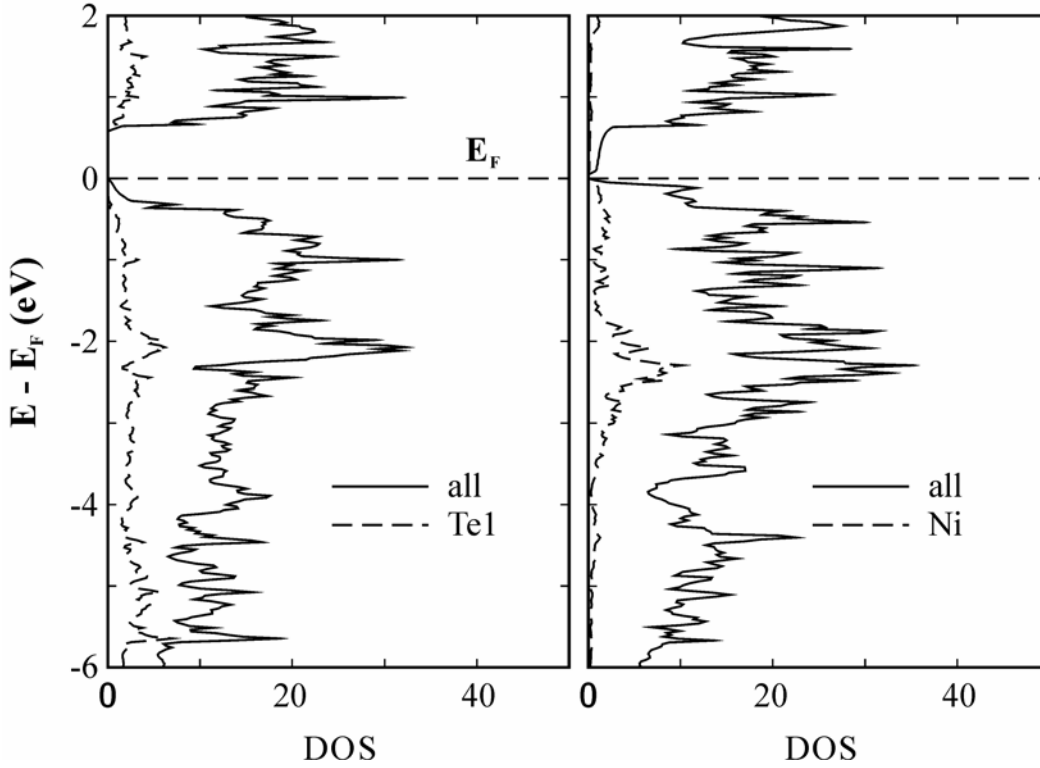


Figure 5.16 Densities of states of $\text{Mo}_3\text{Sb}_5\text{Te}_2$ (left) and $\text{Ni}_{0.5}\text{Mo}_3\text{Sb}_5\text{Te}_2$ (right).

Most features of the band structure remain unchanged from Mo_3Sb_7 , while the gap slightly decreased from 0.7 eV to 0.6 eV. The partial densities of Te are smeared out throughout the energy window shown.

Filling all cubic holes of this structure with Ni atoms results in $\text{Ni}_{0.5}\text{Mo}_3(\text{Sb},\text{Te})_7$. It is noted that experimentally the filling degree did not exceed 12%, however, as in $\text{Ni}_{0.06}\text{Mo}_3\text{Sb}_{5.4}\text{Te}_{1.6}$. As modeling such a composition requires a tenfold supercell, we

computed the DOS of the hypothetical $Ni_{0.5}Mo_3Sb_5Te_2$, shown in the right part of Figure 16. It is evident that the band gap significantly decreased, namely to 0.05 eV, and the addition of nickel does not formally change the electron count, because E_F is still located in the band gap, like in the unfilled $Mo_3Sb_5Te_2$. The DOS of the model for $Ni_{0.25}Mo_3Sb_5Te_2$ exhibits a gap of 0.5 eV, which is only slightly smaller than the unfilled $Mo_3Sb_5Te_2$ model, indicating that the actual material $Ni_{0.06}Mo_3Sb_{5.4}Te_{1.6}$ should have a gap comparable to that of $Mo_3Sb_{5.4}Te_{1.6}$. Therefore, it is concluded that nickel gets added as $Ni^{\pm 0}$, hence exhibits d^{10} configuration. The Ni states show a distinct maximum in the DOS around -2 eV, but add to the states directly below E_F as well. The latter explains why the electrical conductivity increases from $Mo_3Sb_{5.4}Te_{1.6}$ to $Ni_{0.06}Mo_3Sb_{5.4}Te_{1.6}$.

5.3.5 Hf₅Sb₉

The most common structure types exhibiting square nets include ZrSiS [57], NdTe₃ [58] and HfCuSi₂ [59], with the nets formed by elements of the groups 14 - 16. Materials comprising planar square nets of main group elements have fascinated the researcher for decades because of the nonclassical bonding, the tendency to distortions and formation of (possibly modulated) superstructures, and phase transitions often occurring with metal-nonmetal transitions [60-62]. Hf₅Sb₉ crystallizes in its own structure type, as shown in Figure 5.17. The Hf1 atom is surrounded by nine Sb atoms in form of a capped square antiprism. Because of the defects of the Sb3 layer, Hf2 is only bonded to eight Sb atoms forming a capped square antiprism with a vacancy at one corner. Hf-Sb distances are ranging from 2.89 Å to 3.18 Å.

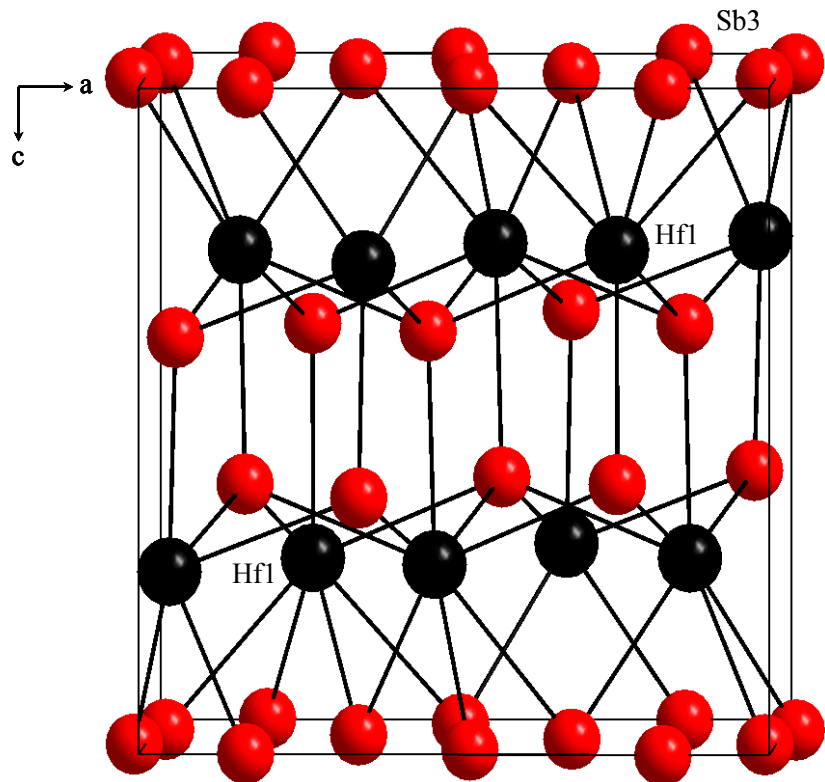


Figure 5.17 Crystal structure of Hf_5Sb_9 . Hf: black; Sb: red. Hf1 is highlighted; the other black atoms are Hf2.

Hf_5Sb_9 represents a uniquely distorted T net formed by the Sb3 atoms (Figure 5.18). Each Sb3 atom is then surrounded by three Sb atoms. The planar squares are composed of Sb–Sb bonds of 3.03 Å, and are connected via additional Sb–Sb bonds of 2.99 Å to an infinite net of Sb3 atoms. An additional Sb3–Sb3 contact of 3.47 Å (dashed line in Figure 5.18) may be weakly bonding as well. Because the two squares per layer and unit cell differ in their height (z parameter) by 0.04 Å, the layer is slightly puckered.

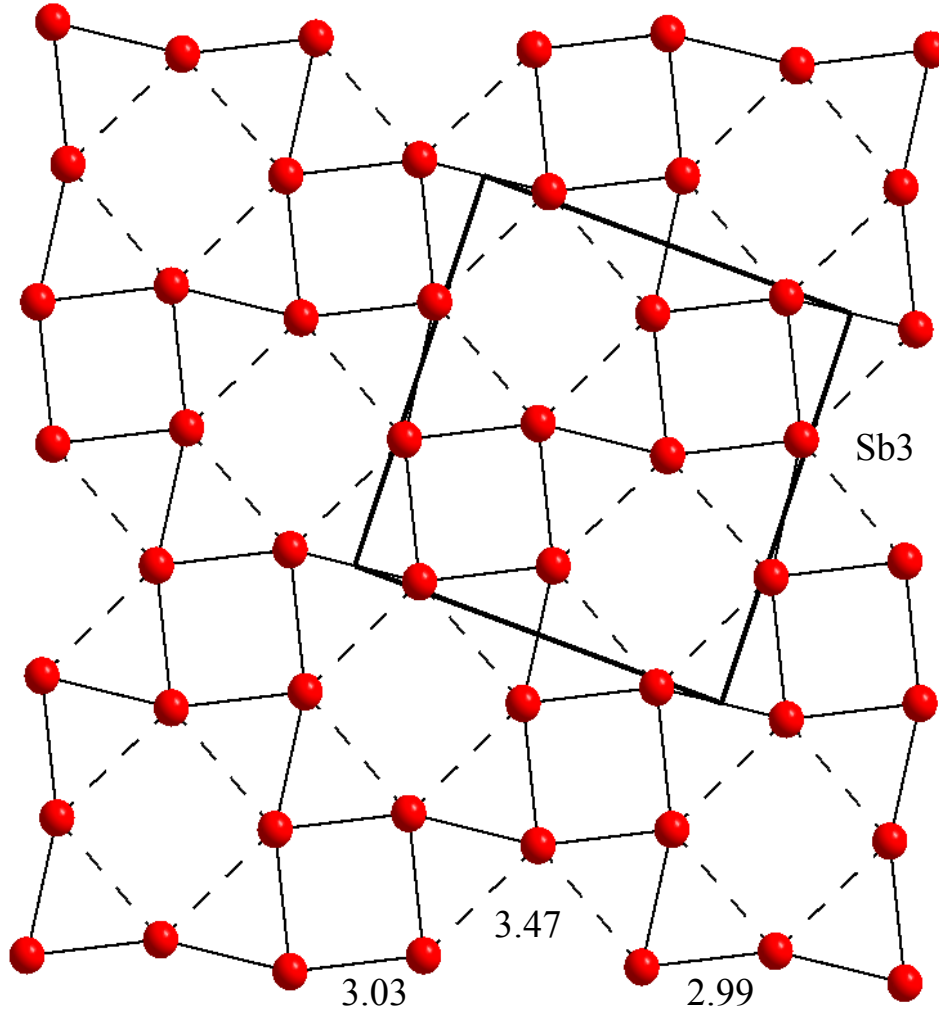


Figure 5.18 T net of Hf_5Sb_9 .

The band structure of Hf_5Sb_9 indicates a metallic property, as several bands cross the Fermi level (Figure 5.19). Because an Sb3 p_y band, depicted via the fat band representation [63], crosses E_F from X to M and M to Γ , the T net itself exhibits two-dimensional metallic properties. The other bands around E_F are predominately of Hf d character, which begin to dominate above -2 eV, and lead to the three-dimensional metallic character.

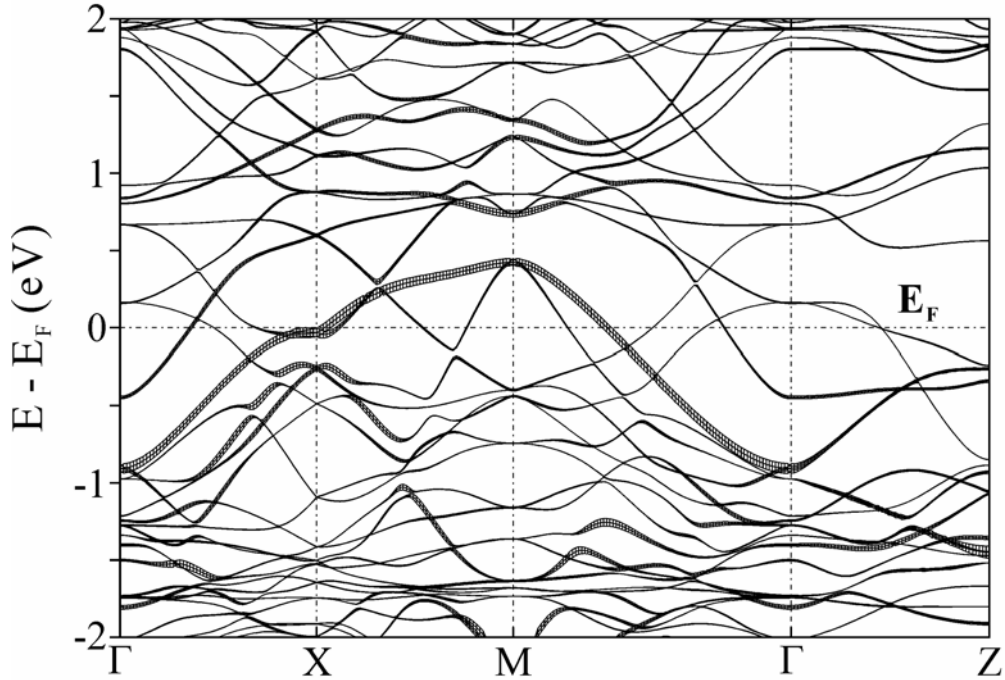


Figure 5.19 Band structure of Hf₅Sb₉, with emphasis on the Sb3 p_y contributions.

The energy window chosen for the densities of states, DOS, in the left part of Figure 5.20 exhibits mostly Hf 5*d* and Sb 5*p* character, with the Sb 5*s* bands occurring below -6 eV outside of that figure. The Hf1–Sb and Hf2–Sb crystal orbital Hamilton population (COHP) curves indicate that these interactions contribute significantly to the metallic character (right part of Figure 5.20). Moreover an increase of the valence electron concentration should lead to stronger Hf–Sb bonding, because more bonding states would be filled.

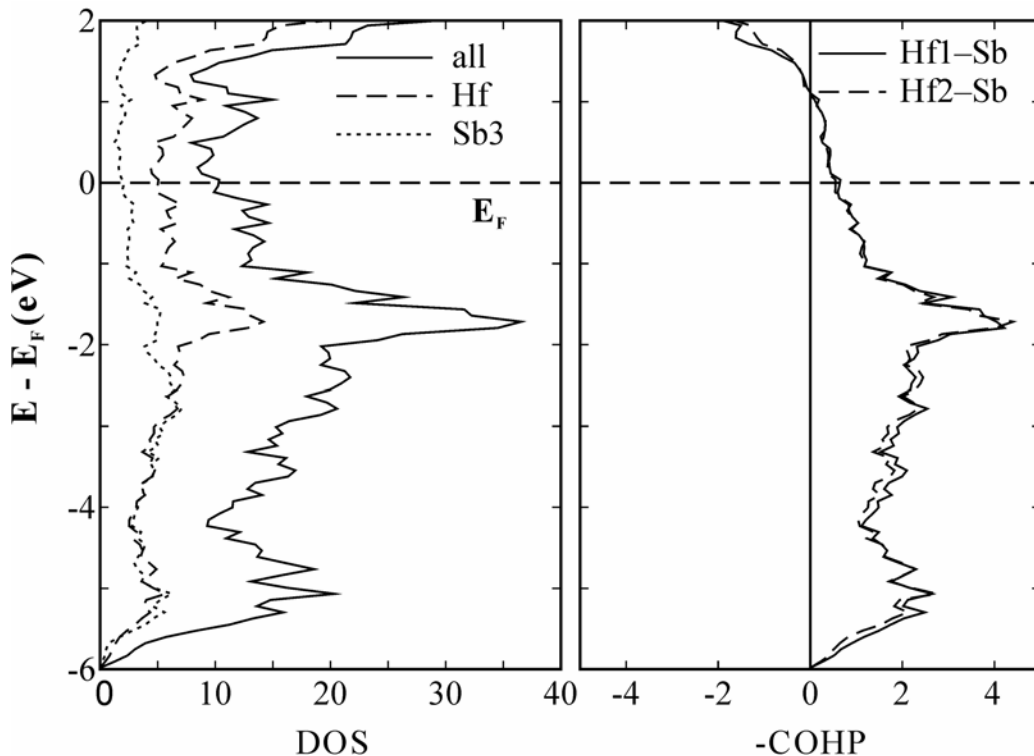


Figure 5.20 Densities of states (left) and Hf-Sb crystal orbital Hamilton population (right) curves.

The frontier orbitals of two hypothetical planar Sb_8^{16-} units, point group C_{4h} in both cases, are depicted in Figure 5.21, with the bond distances of the T net of Hf_5Sb_9 (2.99 Å and 3.03 Å, respectively). On the left, the bond angles were optimized towards a perfect T coordination ($\beta = 90^\circ$), and on the right, the bond angles were taken from the structure refinement of Hf_5Sb_9 ($\beta = 71^\circ$). The dashed lines indicate the additional contacts of 3.47 Å generated by the distortion.

In general, the molecular orbitals, MO's, of the ideal T shaped unit and the actually observed one have the same symmetry, but their energies are shifted in some cases because of the additional interaction of 3.47 Å (dashed lines).

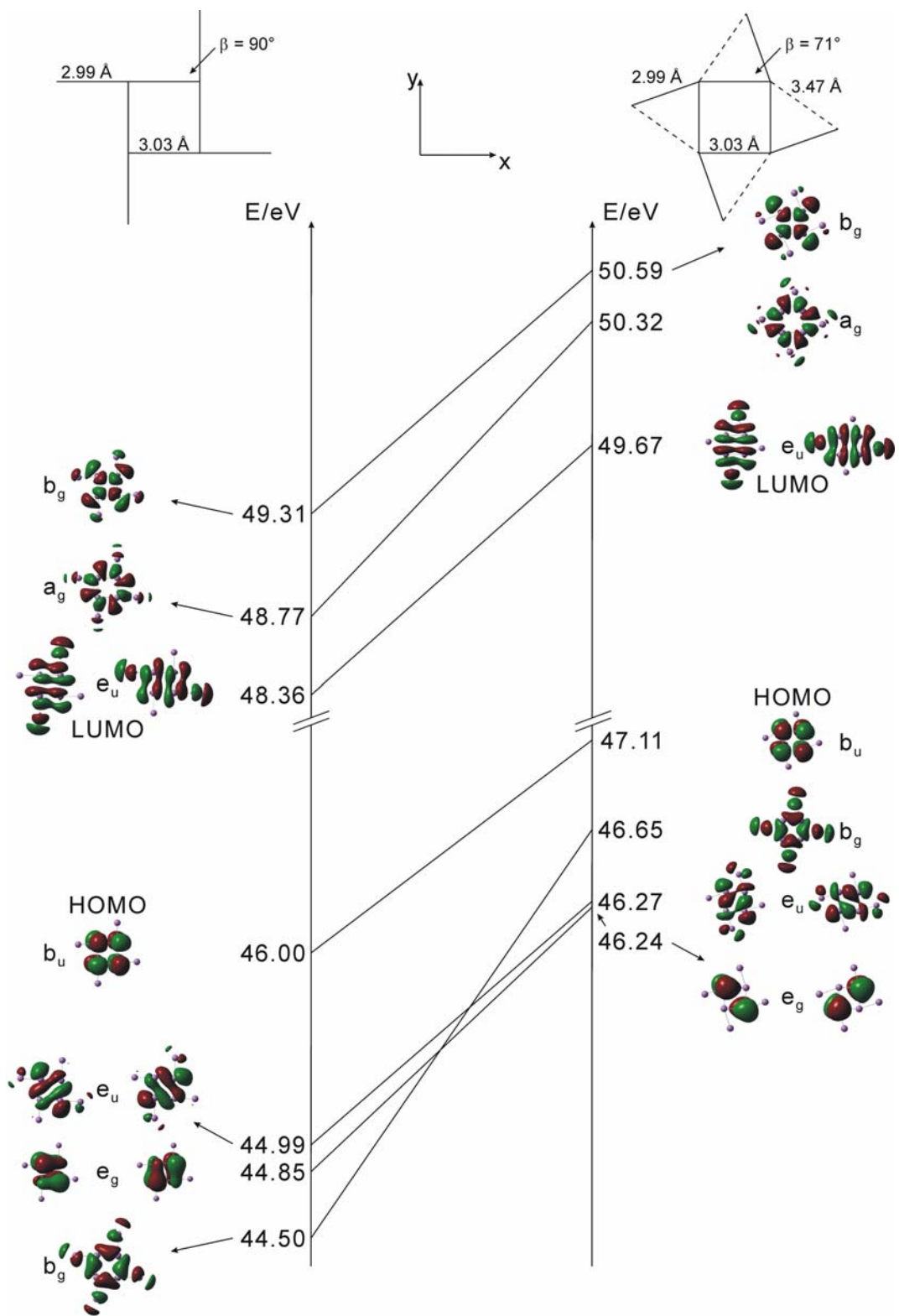


Figure 5.21 MO diagram comparison of Sb_8^{16-} units.

All p_z based MO's are filled, with two occurring about 1.15 eV below the HOMO for the undistorted model ($\beta = 90^\circ$ variant). These two are degenerate, e_g , and one of them is π antibonding along x and π bonding along y , and the other vice versa. Similarly, the corresponding MO's occur 0.9 eV below the HOMO for the $\beta = 71^\circ$ variant.

A larger difference is in the energy of the b_g orbital, which is the second highest occupied MO in the $\beta = 71^\circ$ variant, 0.5 eV below the HOMO, while four MO's are located between this b_g and the HOMO in the $\beta = 90^\circ$ variant. In both cases, the interactions between the in-ring and the terminal Sb atoms are all σ antibonding. The tilt in the distorted form then adds an antibonding contact from each terminal Sb atom to a second in-ring Sb atom, as expressed via the dashed lines on top of Figure 5.21.

The energy differences of the unoccupied MO's are quite comparable between the two variants. The lowest unoccupied molecular orbital, LUMO, is degenerate, of e_u symmetry. These two e_u MO's are σ antibonding and π bonding within the square, while two of the four interactions to the terminal atoms are nonbonding and two σ antibonding. In summary, the four unoccupied MO's are σ antibonding, and thus four more bonding MO's are filled than antibonding. These four bonding MO's are distributed over eight bonds, yielding on average a bond order of $\frac{1}{2}$. The HOMO-LUMO gaps are 2.4 eV when $\beta = 90^\circ$, compared to 2.6 eV when $\beta = 71^\circ$. The total energy of the ideal T-shaped unit is lower by 14.4 eV. Thus the experimentally observed distortion to $\beta = 71^\circ$ is a steric effect, because that variant can be packed more efficiently. The metallic character of Hf_5Sb_9 , predicted via the electronic structure calculation, was confirmed by the electrical conductivity measurement: Furthermore, the Seebeck coefficient was determined to be $+3 \mu\text{VK}^{-1}$ at 300 K, typical for metallic materials.

5.4 Conclusion

The electronic structures of four different antimonides with excellent thermoelectric properties were discussed, focusing on the Sb–Sb interactions. Figure 5.22 compares the figure of merits, ZT , of selected p -type examples, all of them reaching ZT_{\max} at elevated temperatures roughly of the order of one [7,10].

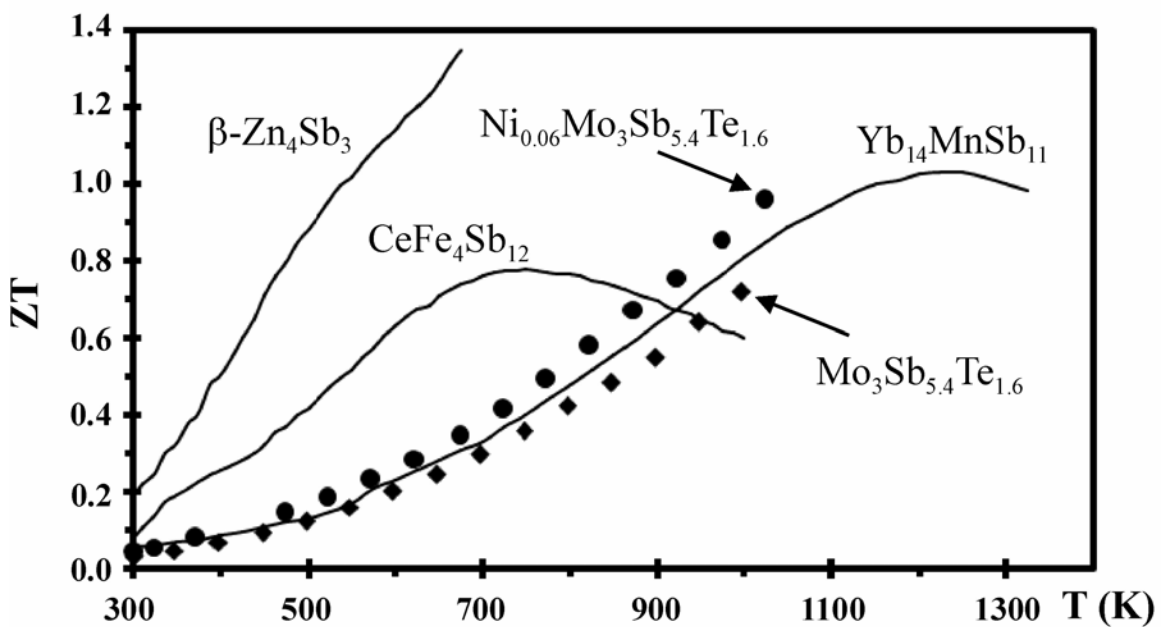


Figure 5.22 Temperature dependence of the thermoelectric figure-of-merit, ZT , for selected p -type antimonides.

The Sb atom substructures are all quite different. In $\beta\text{-Zn}_4\text{Sb}_3$, pairs of Sb atoms are interconnected via longer Sb–Sb interactions to linear chains, while in the filled skutterudites, Sb_4 rectangles are interconnected via longer interactions to a three-dimensional network. In these two examples, short Sb–Sb bonds of the order of single bond distances coexist with long, only slightly bonding Sb–Sb interactions. $\text{Yb}_{14}\text{MnSb}_{11}$ stands out, for its structure

comprises only isolated Sb motifs with only one kind of Sb–Sb interactions, namely intermediate bonds. The Sb atom substructure of Mo_3Sb_7 is the most multifaceted here, exhibiting different contacts, reflected in a three-dimensional network of Sb squares based on long interactions, Sb cubes formed by intermediate interactions, and short Sb–Sb bonds occurring between the Sb cubes. The various Sb atom substructures occur with rather complex crystal structures of these antimonides, beneficial for the low thermal conductivity. Hf_5Sb_9 , on the other hand, contains infinite layers of unusually T-connected Sb–Sb interactions.

All electronic structures except for Hf_5Sb_9 exhibit band gaps < 0.7 eV, and the size of the gap is strongly influenced by the various Sb–Sb interactions dominating the area around the gap in all cases. The importance of the gap size for the thermoelectric properties is evident, since the optimal band gaps of thermoelectrics may vary between $6 k_{\text{B}}T$ and $10 k_{\text{B}}T$, amounting to for example 0.16 eV – 0.26 eV at 300 K and 0.52 eV – 0.86 eV at 1000 K. Our calculations confirm this trend, with $\beta\text{-Zn}_4\text{Sb}_3$ having the smallest gap of 0.3 eV and the lowest optimal operating temperature (below 650 K), and $\text{Mo}_3\text{Sb}_5\text{Te}_2$ (gap of 0.6 eV) and $\text{Yb}_{14}\text{MnSb}_{11}$ (gap of $\text{Ca}_{14}\text{AlSb}_{11}$: 0.7 eV) having the highest optimal operating temperatures (above 1000 K). Moreover, the steep peaks around the gap arising from the Sb–Sb interactions, contribute to a large Seebeck coefficient, advantageous for high figure of merits, ZT.

References

- [1] Rowe, D. M. *CRC Handbook of Thermoelectrics*; CRC Press: Boca Raton, FL, 1995.
- [2] Sales, B. C.; Mandrus, D.; Williams, R. K. *Science* **1996**, *272*, 1325-1328.
- [3] Lamberton, G. A.; Bhattacharya, S.; Littleton, R. T. I.; Kaeser, M. A.; Tedstrom, R. H.; Tritt, T. M.; Yang, J.; Nolas, G. S. *Appl. Phys. Lett.* **2002**, *80*, 598-600.
- [4] Dyck, J. S.; Chen, W.; Uher, C.; Chen, L.; Tang, X.; Hirai, T. *J. Appl. Phys.* **2002**, *91*, 3698-3705.
- [5] Nolas, G. S.; Morelli, D. T.; Tritt, T. M. *Annu. Rev. Mater. Sci.* **1999**, *29*, 89-116.
- [6] Caillat, T.; Fleurial, J. P.; Borshchevsky, A. *J. Phys. Chem. Solids* **1997**, *58*, 1119-1125.
- [7] Brown, S. R.; Kauzlarich, S. M.; Gascoin, F.; Snyder, G. J. *Chem. Mater.* **2006**, *18*, 1973-1877.
- [8] Dashjav, E.; Szczepienowska, A.; Kleinke, H. *J. Mater. Chem.* **2002**, *12*, 345-349.
- [9] Soheilnia, N.; Dashjav, E.; Kleinke, H. *Can. J. Chem.* **2003**, *91*, 1157-1163.
- [10] Gascoin, F.; Rasmussen, J.; Snyder, G. J. *J. Alloys Compd.* **2007**, *427*, 324-329.
- [11] Chung, D. Y.; Hogan, T. P.; Brazis, P.; Rocci-Lane, M.; Kannewurf, C. R.; Bastea, M.; Uher, C.; Kanatzidis, M. G. *Science* **2000**, *287*, 1024-1027.
- [12] Venkatasubramanian, R.; Slivola, E.; Colpitts, T.; O'Quinn, B. *Nature* **2001**, *413*, 597-602.
- [13] Hsu, K. F.; Loo, S.; Guo, F.; Chen, W.; Dyck, J. S.; Uher, C.; Hogan, T.; Polychroniadis, E. K.; Kanatzidis, M. G. *Science* **2004**, *303*, 818-821.
- [14] Xu, J.; Kleinke, K. M.; Kleinke, H. *Z. Anorg. Allg. Chem.*, submitted.
- [15] Skriver, H. L. *The LMTO Method*; Springer: Berlin, Germany, 1984.
- [16] Dronskowski, R.; Blöchl, P. E. *J. Phys. Chem.* **1993**, *97*, 8617-8624.
- [17] Bradley, C. J.; Cracknell, A. P. *The Mathematical Theory of Symmetry in Solids*; Clarendon Press: Oxford, 1972.
- [18] Snyder, G. J.; Christensen, M.; Nishibori, E.; Caillat, T.; Iversen, B. B. *Nat. Mater.* **2004**, *3*, 458-463.
- [19] Cordier, G.; Schäfer, H. *Z. Anorg. Allg. Chem.* **1984**, *519*, 183-188.
- [20] Braun, D. J.; Jeitschko, W. *J. Less-Common Met.* **1980**, *72*, 147-156.
- [21] Jensen, P.; Kjekshus, A.; Skansen, T. *Acta. Chem. Scand.* **1966**, *20*, 417-422.
- [22] Assoud, A.; Kleinke, K. M.; Soheilnia, N.; Kleinke, H. *Angew. Chem. Int. Ed.* **2004**, *43*, 5260-5262.
- [23] Frisch, M. J.; Trucks, G. W.; Schlegel, H. B.; Scuseria, G. E.; Robb, M. A.; Cheeseman, J. R.; Montgomery, J. A.; Vreven, T.; Kudin, K. N.; Burant, J. C.; Millam, J. M.; Iyenga, S. S.; Tomasi, J.; Barone, V.; Mennucci, B.; Cossi, M.; Scalmani, G.; Rega, N.; Petersson, G. A.; Nakatsuji, H.; Hada, M.; Ehara, M.; Toyota, K.; Fukuda, R.; Hasegawa, J.; Ishida, M.; Nakajima, T.; Honda, Y.; Kitao, O.; Nakai, H.; Klene, M.; Li, X.; Knox, J. E.; Hratchian, H. P.; Cross, J. B.; Adamo, C.; Jaramillo, J.; Gomperts, R.; Stratmann, R. E.; Yazyev, O.; Austin, A. J.; Cammi, R.; Pomelli, C.; Ochterski, J. W.; Ayala, P. Y.; Morokuma, K.; Voth, G. A.; Salvador, P.; Dannenberg, J. J.; Zakrzewski, V. G.; Dapprich, S.; Daniels, A. D.; Strain, M. C.; Farkas, O.; Malick, D. K.; Rabuck, A. D.; Raghavachari, K.; Foresman, J. B.; Ortiz, J. V.; Cui, Q.; Baboul, A. G.; Clifford, S.; Cioslowski, J.; Stefanov, B. B.; Liu, G.; Liashenko, A.; Piskorz, P.; Komaromi, I.; Martin, R. L.; Fox, D. J.; Keith, T.; Al-

- Laham, M. A.; Peng, C. Y.; Nanayakkara, A.; Challacombe, M.; Gill, P. M. W.; Johnson, B.; Chen, W.; Wong, M. W.; Gonzalez, C.; Pople, J. A. *Gaussian 03*; Revision C.02 ed.; Gaussian, Inc.: Wallingford, CT, USA, 2004.
- [24] Lee, C.; Yang, W.; Parr, R. G. *Phys. Rev.* **1988**, *37*, 785-789.
- [25] Miehlich, B.; Savin, A.; Stoll, H.; Preuss, H. *Chem. Phys. Lett.* **1989**, *157*, 200-206.
- [26] Pietro, W. J.; Francl, M. M.; Hehre, W. J.; DeFrees, D. J.; Pople, J. A.; Binkley, J. S. *J. Am. Chem. Soc.* **1982**, *104*, 5039-5048.
- [27] Hönle, W.; von Schnering, H.-G. *Z. Kristallogr.* **1981**, *155*, 307-314.
- [28] Miessler, G. L. *Inorganic Chemistry*; Pearson: Upper Saddle River, N. J., 2004.
- [29] Mozharivskyj, Y.; Janssen, Y.; Harringa, J. L.; Kracher, A.; Tsokol, A. O.; Miller, G. J., 18, 822-831. *Chem. Mater.* **2006**, *18*, 822-831.
- [30] Kleinke, H. *Chem. Commun.* **1998**, 2219-2220.
- [31] Müller, W. *Z. Naturforsch. B.* **1977**, *32*, 357-359.
- [32] Kleinke, H. *J. Mater. Chem.* **1999**, *9*, 2703-2708.
- [33] Papoian, G. A.; Hoffmann, R. *Angew. Chem. Int. Ed.* **2000**, *39*, 2408-2448.
- [34] Sharp, J. W.; Jones, E. C.; Williams, R. K.; Martin, P. M.; Sales, B. C. *J. Appl. Phys.* **1995**, *78*, 1013-1018.
- [35] Chakoumakos, B. C.; Sales, B. C.; Mandrus, D.; Keppens, V. *Acta Crystallogr. B* **1999**, *55*, 341-347.
- [36] Kjekshus, A.; Rakke, T. *Acta Chem. Scand.* **1974**, *28*, 99-103.
- [37] Koga, K.; Akai, K.; Oshiro, K.; Matsuura, M. *Mat. Res. Soc. Symp. Proc.* **2002**, *691*, 339-344.
- [38] Fornari, M.; Singh, D. *J. Appl. Phys. Lett.* **1999**, *74*, 3666-3668.
- [39] Fornari, M.; Singh, D. *J. Phys. Rev. B* **1999**, *59*, 9722-9724.
- [40] Anno, H.; Ashida, K.; Matsubara, K.; Nolas, G. S.; Akai, K.; Matsuura, M.; Nagao, J. *Mat. Res. Soc. Symp. Proc.* **2002**, *691*, 49-54.
- [41] Tasman, H. A.; Boswijk, K. H. *Acta Crystallogr.* **1955**, *8*, 59-60.
- [42] Mooney Slater, R. C. L. *Acta Crystallogr.* **1959**, *12*, 187-196.
- [43] Rundle, R. E. *J. Am. Chem. Soc.* **1963**, *85*, 112-113.
- [44] Assoud, A.; Xu, J.; Kleinke, H. *Inorg. Chem.* **2007**, *46*, 9906-9911.
- [45] Böttcher, P. Z. *Z. Anorg. Allg. Chem.* **1977**, *32*, 167-172.
- [46] Böttcher, P. Z. *Z. Anorg. Allg. Chem.* **1980**, *61*, 13-21.
- [47] Kauzlarich, S. M.; Thomas, M. M.; Odink, D. A.; Olmstead, M. M. *J. Am. Chem. Soc.* **1991**, *113*, 7205-7208.
- [48] Carrillo-Cabrera, W.; Somer, M.; Peters, K.; von Schnering, H. G. *Chem. Ber.* **1996**, *129*, 1015-1023.
- [49] Young, D. M.; Torardi, C. C.; Olmstead, M. M.; Kauzlarich, S. M. *Chem. Mater.* **1995**, *7*, 93-101.
- [50] Rehr, A.; Kuromoto, T. Y.; Kauzlarich, S. M.; Del Castillo, J.; Webb, D. J. *Chem. Mater.* **1994**, *6*, 93-99.
- [51] Chan, J. Y.; Olmstead, M. M.; Kauzlarich, S. M.; Webb, D. J. *Chem. Mater.* **1998**, *10*, 3583-3588.
- [52] Brown, A. *Nature* **1965**, *206*, 502-503.
- [53] Häussermann, U.; Elding-Pontén, M.; Svensson, C.; Lidin, S. *Chem. Eur. J.* **1998**, *4*, 1007-1015.

- [54] Zhang, H.; He, J.; Zhang, B.; Su, Z.; Tritt, T. M.; Soheilnia, N.; Kleinke, H. *J. Electron Mater.* **2007**, *36*, 727-731.
- [55] Xu, H.; Soheilnia, N.; Tritt, T. M.; Kleinke, H. *Mat. Res. Soc. Proc.* **2008**, in press.
- [56] Soheilnia, N.; Xu, H.; Zhang, H.; Tritt, T. M.; Swainson, I.; Kleinke, H. *Chem. Mater.* **2007**, *19*, 4063-4068.
- [57] Onken, H.; Vierheilig, K.; Hahn, H. *Z. Anorg. Allg. Chem.* **1964**, *333*, 267-279.
- [58] Norling, B. K.; Steinfink, H. *Inorg. Chem.* **1966**, *5*, 1488-1491.
- [59] Andrukhiv, L. S.; Lysenko, L. A.; Yarmolyuk, Y. P.; Gladyshevskii, E. I. *Dopov. Akad. Nauk Ukr. RSR A* **1975**, 645-648.
- [60] Tremel, W.; Hoffman, R. *J. Am. Chem. Soc.* **1987**, *109*, 124-140.
- [61] Böttcher, P.; Doert, T.; Arnold, H.; Tamazyan, R. *Z. Kristallogr.* **2000**, *215*, 246-253.
- [62] Patschke, R.; Kanatzidis, M. G. *Phys. Chem. Chem. Phys.* **2002**, *4*, 3266-3281.
- [63] Jepsen, O.; Andersen, O. K. *Z. Phys.* **1995**, *97*, 35-47.

Appendix

Table A. 1 Details about starting materials for the synthesis.

| Name | Company | Form | Purity |
|---------------------------------|-------------------|-------------------|----------|
| Na ₂ CO ₃ | Merck | powder | 99.5% |
| CuO | BDH chemicals | powder | 99.0% |
| TeO ₂ | Fisher scientific | powder | 99.0% |
| La ₂ O ₃ | Alfa aesar | powder | 99.9% |
| Mo | Alfa aesar | powder | 99.95% |
| MoO ₂ | Alfa aesar | powder | 99% |
| PbO | Alfa aesar | powder | 99.999% |
| MoO ₃ | Alfa aesar | powder | 99.9995% |
| Tl | Alfa aesar | granules, 1-5 mm | 99.9% |
| Sb | Aldrich | powder, -100 mesh | 99.95% |
| Bi | Aldrich | powder | 99.5% |
| Se | Alfa aesar | powder, -200 mesh | 99.999% |
| Te | Alfa aesar | powder, -325 mesh | 99.99% |

Table A. 2 Crystallographic data of Na₂Cu₂TeO₆.

| | |
|-----------------------------------|--|
| Empirical formula | Na ₂ Cu ₂ TeO ₆ |
| Formula weight | 396.66 g/mol |
| Temperature | 200(2) K |
| Wavelength | 0.71073 Å |
| Crystal system | Monoclinic |
| Space group | <i>C2/m</i> (no. 12) |
| <i>a</i> | 5.7059(6) Å |
| <i>b</i> | 8.6751(9) Å |
| <i>c</i> | 5.9380(6) Å |
| β | 113.740(2)° |
| Volume | 269.02(5) Å ³ |
| <i>Z</i> | 2 |
| Crystal size | 0.04 × 0.04 × 0.02 mm ³ |
| Theta range for data collection | 3.75 to 35° |
| R indices, I > 2σ(I) | R1 = 0.0313, wR2 = 0.0823 |
| R indices, all data | R1 = 0.0314, wR2 = 0.0823 |
| Goodness-of-fit on F ² | 1.068 |

Table A. 3 Atomic coordinates and equivalent displacement parameters.

| Atom | <i>x</i> | <i>y</i> | <i>z</i> | $U_{\text{eq}}/\text{\AA}^2$ |
|------|-----------|------------|-----------|------------------------------|
| Te | 0 | 0 | 0 | 0.0490(1) |
| Cu | 0 | 0.66475(4) | 0 | 0.0069(2) |
| Na | 0 | 0.1839(2) | 0.5 | 0.0111(3) |
| O1 | 0.1936(5) | 0.1632(2) | 0.2121(5) | 0.0076(4) |
| O2 | 0.7574(5) | 0 | 0.1640(5) | 0.0078(4) |

* U_{eq} is defined as one third of the trace of the orthogonalized U_{ij} tensor.

Table A. 4 Selected bond distances [\AA] for $\text{Na}_2\text{Cu}_2\text{TeO}_6$.

| | |
|------------------|----------|
| Te-O1 \times 4 | 1.921(2) |
| Te-O2 \times 2 | 1.988(3) |
| Cu-O1 \times 2 | 1.978(2) |
| Cu-O1 \times 2 | 1.999(2) |
| Cu-O1 \times 2 | 2.533(4) |
| Cu-O1 \times 1 | 2.858(1) |
| Cu-O1 \times 2 | 3.214(1) |
| Na-O1 \times 2 | 2.309(2) |
| Na-O1 \times 2 | 2.386(3) |
| Na-O1 \times 2 | 2.494(2) |

Table A. 5 Data summary of structure determination for $\text{Pb}_{0.69}\text{Mo}_4\text{O}_6$.

| | |
|---------------------------|------------------------|
| <i>a</i> | 9.6112(3) Å |
| <i>c</i> | 2.8411(1) Å |
| <i>q</i> | (0, 0, 0.25) |
| Space group | <i>P4/mbm(00g)00ss</i> |
| # reflections total | 21832 |
| # reflections independent | 1418 |

Table A. 6 Atomic parameters of $\text{Pb}_{0.69}\text{Mo}_4\text{O}_6$ and uncertainties after final refinement.

| Atom | <i>x</i> | <i>y</i> | <i>z</i> | $U_{\text{eq}}/\text{\AA}^2$ |
|-----------------|-------------|-------------|-------------|------------------------------|
| O1 | 0.4589(12) | 0.2627(13) | 0 | 0.006(2) |
| O2 | 0.2099(15) | 0.2902(15) | 0 | 0.014(4) |
| Mo1 | 0.60193(17) | 0.10193(17) | 0.5 | 0.0041(4) |
| Mo2 | 0.3564(2) | 0.1436(2) | 0 | 0.0099(5) |
| ^a Pb | 0 | 0 | 0 | 0.0390(17) |
| ^b Pb | 0 | 0 | -0.2042(10) | 0.0132(7) |

* U_{eq} is defined as one third of the trace of the orthogonalized U_{ij} tensor.

^aPb/^bPb = 30.9(1)/19.1%.

Table A. 7 Final refinement R-values for the incommensurately modulated model for



| | # Observed | R _{obs} | # All | R _{all} |
|-----------------------|------------|------------------|-------|------------------|
| Main reflections | 143 | 7.75 | 189 | 8.59 |
| 1 st order | 99 | 6.99 | 296 | 17.07 |
| 2 nd order | 59 | 13.90 | 169 | 20.08 |

Table A. 8 Crystallographic data of $\text{Tl}_{2.35}\text{Sb}_{8.65}\text{Se}_{14}$.

| | |
|---------------------------------|---|
| Empirical formula | $\text{Tl}_{2.35(1)}\text{Sb}_{8.65}\text{Se}_{14}$ |
| Formula weight | 2651.36 g/mol |
| Temperature | 298(2) K |
| Wavelength | 0.71073 Å |
| Crystal system | Monoclinic |
| Space group | $P2_1/m$ (no. 11) |
| <i>a</i> | 17.201(2) Å |
| <i>b</i> | 4.0792(5) Å |
| <i>c</i> | 21.196(3) Å |
| β | 109.303(3)° |
| Volume | 1403.6(3) Å ³ |
| <i>Z</i> | 2 |
| Crystal size | 0.20 × 0.02 × 0.02 mm ³ |
| Theta range for data collection | 3.72 to 30° |
| R indices, $I > 2\sigma(I)$ | R1 = 0.0442, wR2 = 0.1080 |
| R indices, all data | R1 = 0.0525, wR2 = 0.1130 |
| Goodness-of-fit on F^2 | 1.068 |

Table A. 9 Atomic coordinates and equivalent displacement parameters of $\text{Tl}_{2.35}\text{Sb}_{8.65}\text{Se}_{14}$.

| Atom | <i>x</i> | <i>y</i> | <i>z</i> | $U_{\text{eq}}/\text{\AA}^2$ |
|------------------|-------------|----------|------------|------------------------------|
| ^a Tl1 | 0.85457(12) | 0.2500 | 0.30507(5) | 0.0298(4) |
| Tl2 | 0.57524(4) | 0.2500 | 0.14219(3) | 0.03807(15) |
| ^b Tl3 | 0.66107(6) | 0.7500 | 0.78910(8) | 0.0287(4) |
| Sb1 | 0.09377(5) | 0.2500 | 0.49109(5) | 0.02901(19) |
| Sb2 | 0.27513(6) | 0.7500 | 0.43507(5) | 0.0310(2) |
| Sb3 | 0.47305(5) | 0.2500 | 0.41050(4) | 0.02539(18) |
| Sb4 | 0.65757(6) | 0.7500 | 0.35678(5) | 0.0299(2) |
| ^a Sb5 | 0.8132(4) | 0.2500 | 0.2876(3) | 0.0385(8) |
| Sb6 | 0.07675(5) | 0.2500 | 0.22453(4) | 0.02275(17) |
| ^b Sb7 | 0.6540(3) | 0.7500 | 0.8189(4) | 0.0371(9) |
| Sb8 | 0.87115(5) | 0.7500 | 0.11768(4) | 0.02112(16) |
| Sb9 | 0.88845(5) | 0.2500 | 0.92765(4) | 0.02262(17) |
| Sb10 | 0.66421(5) | 0.2500 | 0.98068(5) | 0.02336(17) |
| Se1 | 0.40578(7) | 0.2500 | 0.51636(6) | 0.0218(2) |
| Se2 | 0.21121(9) | 0.7500 | 0.56691(9) | 0.0397(4) |
| S3 | 0.01587(7) | 0.2500 | 0.58200(6) | 0.0230(2) |
| Se4 | 0.82971(10) | 0.7500 | 0.62816(8) | 0.0398(3) |
| Se5 | 0.36111(8) | 0.7500 | 0.34523(6) | 0.0262(3) |
| Se6 | 0.45533(9) | 0.7500 | 0.69834(7) | 0.0291(3) |
| Se7 | 0.70746(8) | 0.7500 | 0.25314(6) | 0.0239(2) |
| Se8 | 0.96746(7) | 0.7500 | 0.24279(6) | 0.0193(2) |
| Se9 | 0.81616(7) | 0.2500 | 0.79786(6) | 0.0187(2) |
| Se10 | 0.57212(8) | 0.2500 | 0.85301(6) | 0.0253(3) |
| Se11 | 0.77708(7) | 0.2500 | 0.13892(6) | 0.0216(2) |
| Se12 | 0.99176(7) | 0.2500 | 0.08895(6) | 0.0192(2) |
| Se13 | 0.78626(7) | 0.7500 | 0.94546(6) | 0.0226(2) |
| Se14 | 0.41808(7) | 0.2500 | 0.98892(6) | 0.0211(2) |

Table A. 10 Selected interatomic distances [Å] for $\text{Tl}_{2.35}\text{Sb}_{8.65}\text{Se}_{14}$.

| | | | |
|--------------|----------|---------------|----------|
| Tl1–Sb5 | 0.685(6) | Sb4–Se7 | 2.609(3) |
| Tl1–Se7 × 2 | 3.152(2) | Sb4–Se6 × 2 | 2.792(3) |
| Tl1–Se8 × 2 | 3.372(3) | Sb4–Se2 × 2 | 3.075(4) |
| Tl1–Se3 × 2 | 3.366(5) | Sb4–Se1 | 3.218(3) |
| Tl1–Se2 | 3.267(2) | Sb5–Se7 × 2 | 2.669(4) |
| Tl1–Se11 | 3.328(4) | Sb5–Se11 | 3.004(5) |
| Tl2–Se10 × 2 | 3.281(1) | Sb5–Se2 | 3.247(7) |
| Tl2–Se7 × 2 | 3.366(5) | Sb5–Se8 × 2 | 3.711(7) |
| Tl2–Se14 | 3.472(7) | Sb6–Se12 | 2.760(1) |
| Tl2–Se14 × 2 | 3.480(1) | Sb6–Se8 × 2 | 2.885(1) |
| Tl2–Se11 | 3.495(2) | Sb6–Se9 × 2 | 2.891(1) |
| Tl2–Se6 | 3.588(2) | Sb6–Se4 | 3.003(2) |
| Tl3–Sb7 | 0.681(6) | Sb7–Se10 × 2 | 2.710(4) |
| Tl3–Se10 × 2 | 3.115(2) | Sb7–Se13 | 2.887(6) |
| Tl3–Se13 | 3.302(6) | Sb7–Se6 | 3.526(9) |
| Tl3–Se9 | 3.314(1) | Sb7–Se9 × 2 | 3.600(6) |
| Tl3–Se5 | 3.420(2) | Sb8–Se8 | 2.621(1) |
| Tl3–Se6 | 3.424(6) | Sb8–Se11 × 2 | 2.732(1) |
| Sb1–Se3 × 2 | 2.686(2) | Sb8–Se12 × 2 | 3.110(2) |
| Sb1–Se3 | 2.861(1) | Sb8–Se13 | 3.454(5) |
| Sb1–Se2 × 2 | 2.946(1) | Sb9–Se9 | 2.618(1) |
| Sb1–Se4 | 3.213(4) | Sb9–Se13 × 2 | 2.798(1) |
| Sb2–Se4 × 2 | 2.759(3) | Sb9–Se12 × 2 | 3.001(1) |
| Sb2–Se5 | 2.770(3) | Sb9–Se9 | 3.291(5) |
| Sb2–Se1 × 2 | 3.101(4) | Sb10–Se10 | 2.645(5) |
| Sb2–Se2 | 3.324(4) | Sb10–Se14 × 2 | 2.680(2) |
| Sb3–Se5 × 2 | 2.832(1) | Sb10–Se13 × 2 | 3.188(2) |
| Sb3–Se1 | 2.844(1) | Sb10–Se11 | 3.273(6) |
| Sb3–Se6 | 2.953(2) | | |
| Sb3–Se1 × 2 | 2.962(2) | | |

Table A. 11 Crystallographic data of $\text{Tl}_{1.97}\text{Sb}_{8.03}\text{Se}_{13}$.

| | |
|---------------------------------|---|
| Empirical formula | $\text{Tl}_{1.97(1)}\text{Sb}_{8.03}\text{Se}_{13}$ |
| Formula weight | 2403.44 g/mol |
| Temperature | 298(2) K |
| Wavelength | 0.71073 Å |
| Crystal system | Monoclinic |
| Space group | $P2_1/m$ (no. 11) |
| <i>a</i> | 17.222(3) Å |
| <i>b</i> | 4.0682(6) Å |
| <i>c</i> | 18.318(3) Å |
| β | 90.320(3)° |
| Volume | 1283.4(3) Å ³ |
| <i>Z</i> | 2 |
| Crystal size | 0.35 × 0.02 × 0.02 mm ³ |
| Theta range for data collection | 3.26 to 30° |
| R indices, $I > 2\sigma(I)$ | R1 = 0.0649, wR2 = 0.1068 |
| R indices, all data | R1 = 0.0865, wR2 = 0.1159 |
| Goodness-of-fit on F^2 | 1.188 |

Table A. 12 Atomic coordinates and equivalent displacement parameters of $\text{Tl}_{1.97}\text{Sb}_{8.03}\text{Se}_{13}$.

| Atom | <i>x</i> | <i>y</i> | <i>z</i> | $U_{\text{eq}}/\text{\AA}^2$ |
|-------------------|------------|----------|------------|------------------------------|
| ^a Tl1 | 0.3062(3) | 0.7500 | 0.3256(3) | 0.0171(4) |
| ^b Tl2 | 0.2488(1) | 0.2500 | 0.7663(1) | 0.0285(4) |
| ^c Tl3A | 0.5179(1) | 0.2500 | 0.8451(1) | 0.0376(3) |
| ^c Tl3B | 0.4663(6) | 0.2500 | 0.8217(5) | 0.0376(3) |
| Sb1 | 0.9169(1) | 0.2500 | 0.793(1) | 0.0220(3) |
| Sb2 | 0.1768(1) | 0.2500 | 0.1261(1) | 0.0201(3) |
| Sb3 | 0.3277(1) | 0.7500 | -0.182(1) | 0.0207(3) |
| Sb4 | 0.8985(1) | 0.2500 | 0.4772(1) | 0.0263(3) |
| Sb5 | 0.7010(1) | 0.7500 | 0.4554(1) | 0.0253(3) |
| Sb6 | 0.164(1) | 0.7500 | 0.2447(1) | 0.0220(3) |
| Sb7 | 0.4945(1) | 0.2500 | 0.3859(1) | 0.0286(4) |
| ^a Sb8A | 0.2672(2) | 0.7500 | 0.3293(2) | 0.0171(4) |
| ^a Sb8B | 0.2911(11) | 0.7500 | 0.3485(8) | 0.0171(4) |
| ^b Sb9A | 0.2828(6) | 0.2500 | 0.7941(6) | 0.0285(4) |
| ^b Sb9B | 0.2642(13) | 0.2500 | 0.8106(12) | 0.0285(4) |
| Se1 | 0.9797(2) | 0.7500 | 0.4027(1) | 0.0299(5) |
| Se2 | 0.8997(1) | 0.2500 | 0.2210(1) | 0.0185(4) |
| Se3 | 0.8072(1) | 0.7500 | 0.599(1) | 0.0218(4) |
| Se4 | 0.3950(1) | 0.2500 | 0.2774(1) | 0.0243(5) |
| Se5 | 0.8101(1) | 0.7500 | 0.5575(1) | 0.0268(5) |
| Se6 | 0.7761(1) | 0.2500 | 0.3779(1) | 0.0241(5) |
| Se7 | 0.9572(1) | 0.2500 | -0.959(1) | 0.0195(4) |
| Se8 | 0.1328(1) | 0.2500 | 0.2626(1) | 0.0195(4) |
| Se9 | 0.3682(1) | 0.7500 | 0.8410(1) | 0.0249(5) |
| Se10 | 0.4234(1) | 0.2500 | 0.127(1) | 0.0212(4) |
| Se11 | 0.5776(2) | 0.7500 | 0.3197(1) | 0.0299(5) |
| Se12 | 0.2791(1) | 0.7500 | 0.1494(1) | 0.0218(4) |
| Se13 | 0.6095(2) | 0.2500 | 0.5393(1) | 0.0304(5) |

* U_{eq} is defined as one third of the trace of the orthogonalized U_{ij} tensor.

^aTl1/Sb8A/8B = 21.6(3)/66.1(4)/12.2%; ^bTl2/Sb9A/Sb9B = 71.2(4)/19.9(3)/8.9%;

^cTl3A/Tl3B = 88.4(2)/11.6%.

Table A. 13 Selected interatomic distances [Å] for $\text{Tl}_{1.97}\text{Sb}_{8.03}\text{Se}_{13}$

| | | | |
|---------------|-----------|--------------|-----------|
| Tl1–Sb8A | 0.675(4) | Sb4–Se1 | 3.030(5) |
| Tl1–Sb8B | 0.495(2) | Sb4–Se1 × 2 | 2.824(3) |
| Tl1–Se4 × 2 | 2.696(4) | Sb4–Se5 × 2 | 2.940(3) |
| Tl1–Se5 × 2 | 3.575(6) | Sb4–Se6 | 2.778(5) |
| Tl1–Se8 × 2 | 3.788(5) | Sb5–Se5 | 2.645(5) |
| Tl1–Se12 | 3.259(6) | Sb5–Se6 × 2 | 2.802(3) |
| Tl1–Se13 | 2.862(7) | Sb5–Se11 | 3.260(6) |
| Tl2–Se2 × 2 | 3.276(2) | Sb5–Se13 × 2 | 3.001(3) |
| Tl2–Se3 | 3.331(4) | Sb6–Se1 | 2.967(3) |
| Tl2–Se6 × 2 | 3.359(2) | Sb6–Se2 × 2 | 2.890(2) |
| Tl2–Se9 × 2 | 3.195(3) | Sb6–Se7 | 2.764(3) |
| Tl2–Se11 | 3.389(5) | Sb6–Se8 × 2 | 2.8739(2) |
| Tl3A–Tl3B | 0.984(10) | Sb7–Se4 | 2.618(5) |
| Tl3A–Se4 × 2 | 3.386(4) | Sb7–Se11 × 2 | 2.770(3) |
| Tl3A–Se9 | 3.285(5) | Sb7–Se13 | 3.492(3) |
| Tl3A–Se10 | 3.481(5) | Sb7–Se13 × 2 | 3.042(7) |
| Tl3A–Se10 × 2 | 3.452(3) | Sb8A–Se4 × 2 | 3.148(3) |
| Tl3A–Se11 | 3.430(5) | Sb8A–Se5 × 2 | 3.200(4) |
| Tl3A–Se12 | 3.498(2) | Sb8A–Se8 × 2 | 3.310(4) |
| Tl3B–Se4 × 2 | 3.632(9) | Sb8A–Se12 | 3.303(4) |
| Tl3B–Se9 × 2 | 2.669(7) | Sb8A–Se13 | 3.201(6) |
| Tl3B–Se10 | 3.579(10) | Sb8B–Se4 × 2 | 3.010(13) |
| Tl3B–Se11 | 2.694(10) | Sb8B–Se5 × 2 | 3.190(14) |
| Sb1–Se2 | 2.615(3) | Sb8B–Se8 × 2 | 3.741(16) |
| Sb1–Se3 × 2 | 2.797(2) | Sb8B–Se12 | 3.652(15) |
| Sb1–Se7 | 3.287(3) | Sb8B–Se13 | 2.668(17) |
| Sb1–Se7 × 2 | 2.988(2) | Sb9A–Se2 × 2 | 3.753(9) |
| Sb2–Se3 | 3.419(3) | Sb9A–Se3 | 3.099(12) |
| Sb2–Se7 × 2 | 3.123(2) | Sb9A–Se9 × 2 | 2.650(7) |
| Sb2–Se8 | 2.618(3) | Sb9A–Se11 | 3.191(12) |
| Sb2–Se12 × 2 | 2.723(2) | Sb9B–Se2 | 3.525(18) |
| Sb3–Se3 × 2 | 3.177(3) | Sb9B–Se3 | 2.678(22) |
| Sb3–Se9 | 2.676(3) | Sb9B–Se9 × 2 | 2.764(15) |
| Sb3–Se10 × 2 | 2.677(2) | Sb9B–Se11 | 3.633(23) |
| Sb3–Se12 | 3.187(4) | | |

Table A. 14 Crystallographic data of $\text{Tl}_{2.04}\text{Bi}_{7.96}\text{Se}_{13}$.

| | |
|---------------------------------|---|
| Empirical formula | $\text{Tl}_{2.04(1)}\text{Bi}_{7.96}\text{Se}_{13}$ |
| Formula weight | 3106.88 g/mol |
| Temperature | 298(2) K |
| Wavelength | 0.71073 Å |
| Crystal system | Monoclinic |
| Space group | $P2_1/m$ (no. 11) |
| <i>a</i> | 17.397(3) Å |
| <i>b</i> | 4.1760(8) Å |
| <i>c</i> | 18.336(4) Å |
| β | 90.748(4)° |
| Volume | 1332.0(5) Å ³ |
| <i>Z</i> | 2 |
| Crystal size | 0.40 × 0.02 × 0.02 mm ³ |
| Theta range for data collection | 3.21 to 30° |
| R indices, $I > 2\sigma(I)$ | R1 = 0.0789, wR2 = 0.1212 |
| R indices, all data | R1 = 0.1213, wR2 = 0.1333 |
| Goodness-of-fit on F^2 | 1.160 |

Table A. 15 Atomic coordinates and equivalent displacement parameters of $\text{Tl}_{2.04}\text{Bi}_{7.96}\text{Se}_{13}$.

| Atom | x | y | z | $U_{\text{eq}}/\text{\AA}^2$ |
|-------------------|-------------|--------|-------------|------------------------------|
| ^a Tl1 | 0.27172(6) | 0.7500 | 0.32738(6) | 0.0354(2) |
| ^b Tl2 | 0.25026(4) | 0.2500 | 0.77052(4) | 0.0354(2) |
| ^c Tl3 | 0.51480(5) | 0.2500 | 0.84425(5) | 0.0473(2) |
| Bi1 | 0.91719(3) | 0.2500 | 0.07828(2) | 0.0218(1) |
| Bi2 | 0.17363(3) | 0.2500 | 0.12253(2) | 0.0219(1) |
| Bi3 | 0.33074(2) | 0.7500 | -0.01683(3) | 0.0237(1) |
| Bi4 | 0.89291(3) | 0.2500 | 0.47672(3) | 0.0270(1) |
| Bi5 | 0.69460(2) | 0.7500 | 0.45207(2) | 0.0230(1) |
| Bi6 | 0.91719(3) | 0.2500 | 0.07828(2) | 0.0218(1) |
| Bi7 | 0.17363(3) | 0.2500 | 0.12253(2) | 0.0219(1) |
| ^a Bi8 | 0.29483(6) | 0.7500 | 0.32378(6) | 0.0354(2) |
| ^b Bi9 | 0.27186(16) | 0.2500 | 0.79178(15) | 0.0354(2) |
| ^c Bi10 | 0.48443(13) | 0.2500 | 0.82777(13) | 0.0473(2) |
| Se1 | 0.98322(7) | 0.7500 | 0.40563(6) | 0.0259(3) |
| Se2 | 0.89771(6) | 0.2500 | 0.22653(6) | 0.0211(3) |
| Se3 | 0.80389(6) | 0.7500 | 0.05559(6) | 0.0236(3) |
| Se4 | 0.39104(7) | 0.2500 | 0.26982(7) | 0.0329(4) |
| Se5 | 0.81040(7) | 0.7500 | 0.55850(6) | 0.0244(3) |
| Se6 | 0.76925(6) | 0.2500 | 0.37142(6) | 0.0218(3) |
| Se7 | 0.95885(6) | 0.2500 | -0.09159(6) | 0.0190(3) |
| Se8 | 0.13425(6) | 0.2500 | 0.26696(6) | 0.0218(3) |
| Se9 | 0.37192(7) | 0.7500 | 0.83610(7) | 0.0283(3) |
| Se10 | 0.42904(7) | 0.2500 | 0.01599(7) | 0.0262(3) |
| Se11 | 0.57703(7) | 0.7500 | 0.31974(6) | 0.0232(3) |
| Se12 | 0.27868(6) | 0.7500 | 0.14677(6) | 0.0204(3) |
| Se13 | 0.60748(7) | 0.2500 | 0.53578(7) | 0.0271(3) |

* U_{eq} is defined as one third of the trace of the orthogonalized U_{ij} tensor.

^aTl1/Bi8 = 51.1(1)/48.9%; ^bTl2/Bi9 = 80.5(1)/19.5%; ^cTl3/Bi10 = 72.4(1)/27.6%.

Table A. 16 Selected interatomic distances [Å] for $Tl_{2.04}Bi_{7.96}Se_{13}$.

| | | | |
|--------------|----------|--------------|----------|
| Tl1–Bi8 | 0.408(2) | Bi3–Se12 | 3.145(4) |
| Tl1–Se4 × 2 | 3.315(2) | Bi4–Se1 | 3.029(6) |
| Tl1–Se5 × 2 | 3.295(4) | Bi4–Se1 × 2 | 2.929(3) |
| Tl1–Se8 × 2 | 3.352(3) | Bi4–Se5 × 2 | 2.954(3) |
| Tl1–Se12 | 3.315(2) | Bi4–Se6 | 2.872(6) |
| Tl1–Se13 | 3.252(7) | Bi5–Se5 | 2.786(6) |
| Tl2–Bi9 | 0.538(3) | Bi5–Se6 × 2 | 2.878(3) |
| Tl2–Se2 × 2 | 3.316(1) | Bi5–Se11 | 3.153(6) |
| Tl2–Se3 | 3.336(4) | Bi5–Se13 × 2 | 3.012(3) |
| Tl2–Se6 × 2 | 3.350(2) | Bi6–Se2 × 2 | 2.956(2) |
| Tl2–Se9 × 2 | 3.197(3) | Bi6–Se2 | 2.881(3) |
| Tl2–Se11 | 3.449(6) | Bi6–Se7 | 2.979(2) |
| Tl3–Bi10 | 0.605(3) | Bi6–Se8 × 2 | 2.950(1) |
| Tl3–Se4 × 2 | 3.392(4) | Bi7–Se4 | 2.743(6) |
| Tl3–Se9 | 3.248(1) | Bi7–Se11 × 2 | 2.837(3) |
| Tl3–Se10 | 3.502(6) | Bi7–Se13 | 3.382(7) |
| Tl3–Se10 × 2 | 3.437(3) | Bi7–Se13 × 2 | 3.082(3) |
| Tl3–Se11 | 3.386(6) | Bi8–Se4 × 2 | 2.861(3) |
| Tl3–Se12 | 3.594(2) | Bi8–Se5 × 2 | 3.532(5) |
| Bi1–Se2 | 2.744(2) | Bi8–Se12 | 3.254(2) |
| Bi1–Se3 × 2 | 2.898(1) | Bi8–Se13 | 3.067(6) |
| Bi1–Se7 | 3.207(3) | Bi9–Se2 × 2 | 3.626(3) |
| Bi1–Se7 × 2 | 3.009(1) | Bi9–Se3 | 3.109(6) |
| Bi2–Se3 | 3.294(2) | Bi9–Se9 | 2.831(3) |
| Bi2–Se7 × 2 | 3.156(2) | Bi9–Se11 | 3.352(7) |
| Bi2–Se8 | 2.744(3) | Bi10–Se4 × 2 | 3.515(5) |
| Bi2–Se12 × 2 | 2.806(1) | Bi10–Se9 × 2 | 2.867(2) |
| Bi3–Se3 × 2 | 3.210(2) | Bi10–Se10 | 3.595(5) |
| Bi3–Se9 | 2.799(3) | Bi10–Se11 | 2.895(5) |
| Bi3–Se10 × 2 | 2.760(2) | | |